THE GIANT DIPOLE RESONANCE REGION OF ^{14}N POLARIZED AND UNPOLARIZED PHOTON CAPTURE MEASUREMENTS

by

James David Turner

Department of Physics
Duke University

Date: September 5, 1978

Approved:

N. Russell Roberson, Supervisor

Robert L Walter

Hugh Robinson

E. L. Belpuch

A dissertation submitted in partial fulfillment of the requirements for the degree of Doctor of Philosophy in the Department of Physics in the Graduate School of Arts and Sciences of Duke University

1978

THE GIANT DIPOLE RESONANCE REGION OF ^{14}N POLARIZED AND UNPOLARIZED PROTON CAPTURE MEASUREMENTS

by

James David Turner

Department of Physics
Duke University

Date: September 5, 1978

Approved:

N. Russell Roberson, Supervisor

Robert L Walter

Hugh Robinson

E. G. Bilpuch

An abstract of a dissertation submitted in partial fulfillment of the requirements for the degree of Doctor of Philosophy in the Department of Physics in the Graduate School of Arts and Sciences of Duke University

1978

THE GIANT DIPOLE RESONANCE REGION

OF ^{14}N

POLARIZED AND UNPOLARIZED PROTON CAPTURE MEASUREMENTS

by

JAMES DAVID TURNER

The 90 degree yield curves for the $^{13}C(p,\gamma_0)^{14}N$ and $^{13}C(p,\gamma_1)^{14}N$ reactions have been measured for incident proton energies ranging from 6.25 to 17.0 MeV. The integrated yield for the ground state transition exhausts approximately 6 percent of the classical dipole sum rule in the region of 13.3 to 23.3 MeV excitation. The transition to the first excited state exhausts approximately 9 percent of the classical dipole sum rule between 11.0 and 21.0 MeV excitation. The yield curves are compared to earlier measurements of these reactions.

Angular distributions of cross section and analyzing power of the $^{13}C(p,\gamma_0)^{14}N$ and $^{13}C(p,\gamma_1)^{14}N$ reactions were measured at twelve energies spanning the GDR region. The cross section was measured at 9 angles ranging from 30 to 154 degrees and the analyzing power was measured at seven

angles from 42 to 142 degrees. An analysis which assumed pure E1 radiation was used to determine the transition matrix elements for the $^{13}C(p,\gamma_0)^{14}N$ reaction. These results are compared to a simple direct-semidirect model calculation.

The data from the $^{13}C(p,\gamma_1)^{14}N$ reaction were analyzed in a similar manner, but for this case it was possible to determine the E2 as well as the E1 transition matrix elements. At most energies studied in the present work, two E2 solutions were found. Arguments are presented to suggest that of the two E2 solutions, the ones with the smaller cross section are the physical solutions. With this assumption, this channel exhausts approximately 20 percent of the E2 energy weighted isoscalar sum rule for self-conjugate nuclei. The magnitude and energy dependence of this E2 cross section are in reasonable agreement with a pure direct model calculation and show no evidence for a giant quadrupole resonance.

ACKNOWLEDGEMENTS

I wish to express my appreciation to my advisor, Dr. N. R. Roberson for his interest, help, advice, and support during my graduate career. I would also like to extend my personal thanks to Dr. Henry Weller for his advice, interest and support of this research. I also wish to thank Dr. D. R. Tilley, Mr. Mark Jensen, Mr. Steve Manglos, and Dr. R. A. Blue for their assistance in data collection. I would also like to thank Dr. Thomas Clegg and all others who spent many hours in developing and maintaining the polarized ion source.

I also extend my gratitude to Dr. Chris Cameron for the various computer codes used in the analysis of the data involved in this study. I would also like to thank Dr. R. C. McBroom for his spectrum analysis code.

I extend my gratitude to the technical staff for valuable assistance with the accelerator and associated equipment. I especially wish to thank Mr. Sidney Edwards for his help with the computers and various electronic devices.

I wish to thank Mrs. Mike Bailey for her skillful assistance and patience in the preparation of the figures.

I extend a special thanks to Ms. Gail Glendinning for her assistance in the preparation and proof reading of this manuscript.

I am grateful to the late Dr. Henry Newson and to Dr. E. G. Bilpuch for providing me with a research assistantship.

I extend my deepest gratitude to my parents for their continuing support and encouragement.

This study was supported in part by the United States Department of Energy.

J. D. T.

CONTENTS

LIST OF FIGURES

LIST OF TABLES

THE GIANT DIPOLE RESONANCE REGION

of ^{14}N

POLARIZED AND UNPOLARIZED CAPTURE MEASUREMENTS

Chapter I

INTRODUCTION

The giant dipole resonance (GDR) is the dominant feature of the photon absorption cross section for nuclei. The GDR is located at an excitation energy of approximately $80/A^{1/3}$ MeV for medium and heavy nuclei and has widths ranging from 3 to 10 MeV; for the light nuclei the centroid is located near 20 MeV (Hayward, 1970). Contributions to the photonuclear cross section from M1 and E2 radiation have been investigated in recent years and some of the properties of these types of transitions have been established (Hanna, 1977 and references therein).

Investigations of the photonuclear cross section have been carried out using various techniques. Included among these are electron scattering, photon scattering and absorption, and radiative nucleon capture. Polarized proton capture has been shown to be a valuable tool in the analysis of the photonuclear cross section (Hanna et al., 1972, Glavish et al., 1972, and Weller et al., 1974). The range of available proton energies and present polarized beam intensities coupled with the high resolution and large solid angle offered by NaI detectors are sufficient to allow a detailed study of the GDR region of most nuclei. For cases

where the target and residual spins are 1/2 and 0, respectively, (or vice versa) it is possible to obtain both E1 and E2 amplitudes and phases from a transition matrix element analysis (see for example, Hanna et al., 1974 and Weller et al., 1976).

The present work is an investigation of the GDR region of ^{14}N via the $^{13}C(p,\gamma)^{14}N$ reaction. The capture gamma rays were detected by a large NaI detector system with an anti-coincidence shield and pile-up suppression. The resolution of the gamma ray detection system allowed the study of transitions to the ground state ($J^{\pi}=1^{+}$,T=0) and to the first excited state ($J^{\pi}=0^{+}$,T=1, 2.313 MeV) in ^{14}N. Yield curves have been measured for the $^{13}C(p,\gamma_0)^{14}N$ (Q=7.55 MeV) and $^{13}C(p,\gamma_1)^{14}N$ reactions for proton energies ranging from 6.25 to 17.0 MeV. Twelve angular distributions of cross section and analyzing power were measured at proton energies ranging from 8.0 to 15.5 MeV.

An analysis of the GDR built on the ground state of ^{14}N is limited by the fact that the target spin (the ground state of ^{13}C) is 1/2 and the final spin (the ground state of ^{14}N) is 1. This combination of spins allows too many transition matrix elements for a combined E1 and E2 analysis. For this reason, only an E1 analysis of this reaction is included in this study.

However, the GDR built on the first excited state of ^{14}N is particularly well suited for investigation via

polarized proton capture. The combination of target spin of 1/2 (the ground state spin of ^{13}C) and final spin of 0 (the first excited state of ^{14}N) allows extraction of both E1 and E2 T-matrix amplitudes and phases directly from the data. This study includes such an analysis.

A theoretical model that has been particularly successful in describing the radiative capture process is the direct-semidirect model (DSD) (Brown, 1964 and Weller, Roberson, and Cotanch, 1978). Model calculations are compared to E1 amplitudes extracted from both the ground state and first excited state transitions and to the E2 amplitudes extracted from the first excited state transition.

Chapter II

EXPERIMENTAL APPARATUS AND TECHNIQUES

2.1 BEAM PARAMETERS AND TRANSPORT SYSTEM

This study involves the use of both polarized and unpolarized beams accelerated by the Triangle University Nuclear Laboratory (TUNL) model FN Van de Graaff accelerator. Unpolarized beams were accelerated to energies ranging from 6.25 to 17.0 MeV with beam currents ranging from 50 to 400 nanoamperes on target.

The polarized beam was provided by the TUNL polarized ion source (Clegg et al., 1970). The beam current obtained on target ranged from 25 to 110 nA and averaged about 70 na with an average polarization of 0.80±0.02. The polarization was measured after each data point (one spin state taken at one detector angle) with the quench-ratio technique (Trainor et al., 1974). This technique involves the quenching of the polarized fraction of the beam with a strong d.c. electric field and is accurate if the beam does not contain charged unpolarized background beam. Source operation was monitored on a regular basis and small corrections were made for charged background when needed.

The high energy beam transport system employed two 90 degree analyzing magnets and a 30 degree switching magnet.

A series of adjustable horizontal and vertical slits was used to define and limit the beam throughout the transport system. A diagram of the experimental area is shown in figure 1. A final set of horizontal and vertical slits could be used to define the beam image. These slits were shielded from the gamma ray detector by approximately 20 cm of lead, 20 cm of concrete, and 30 cm of paraffin. In practice the beam was well focussed at the exit of the switching magnet and further definition with these slits was not required. The beam was transported from the slits to the target by two magnetic steerers and a magnetic quadrupole lens. The target was mounted in a brass scattering chamber 15.5 cm in diameter and 8 cm in height. The beam was collimated to 4 mm in this chamber with a tantalum collimator assembly which was electrically insulated from the chamber. Beam current on the collimator was constantly monitored and consistently maintained below one nanoampere to reduce slit scattering and background radiation. Total beam current was integrated with a tantalum-lined Faraday cup located 3 meters downstream from the target chamber. The uncertainty in the charge integration was less than 2 percent. The Faraday cup was shielded from the gamma ray detector with approximately 10 cm of copper, 10 cm of lead, and 25 cm of high density paraffin doped with lithium carbonate.

Figure 1. Schematic diagram of the target area. The final set of collimating slits is indicated by arrows on either side of the beamline.

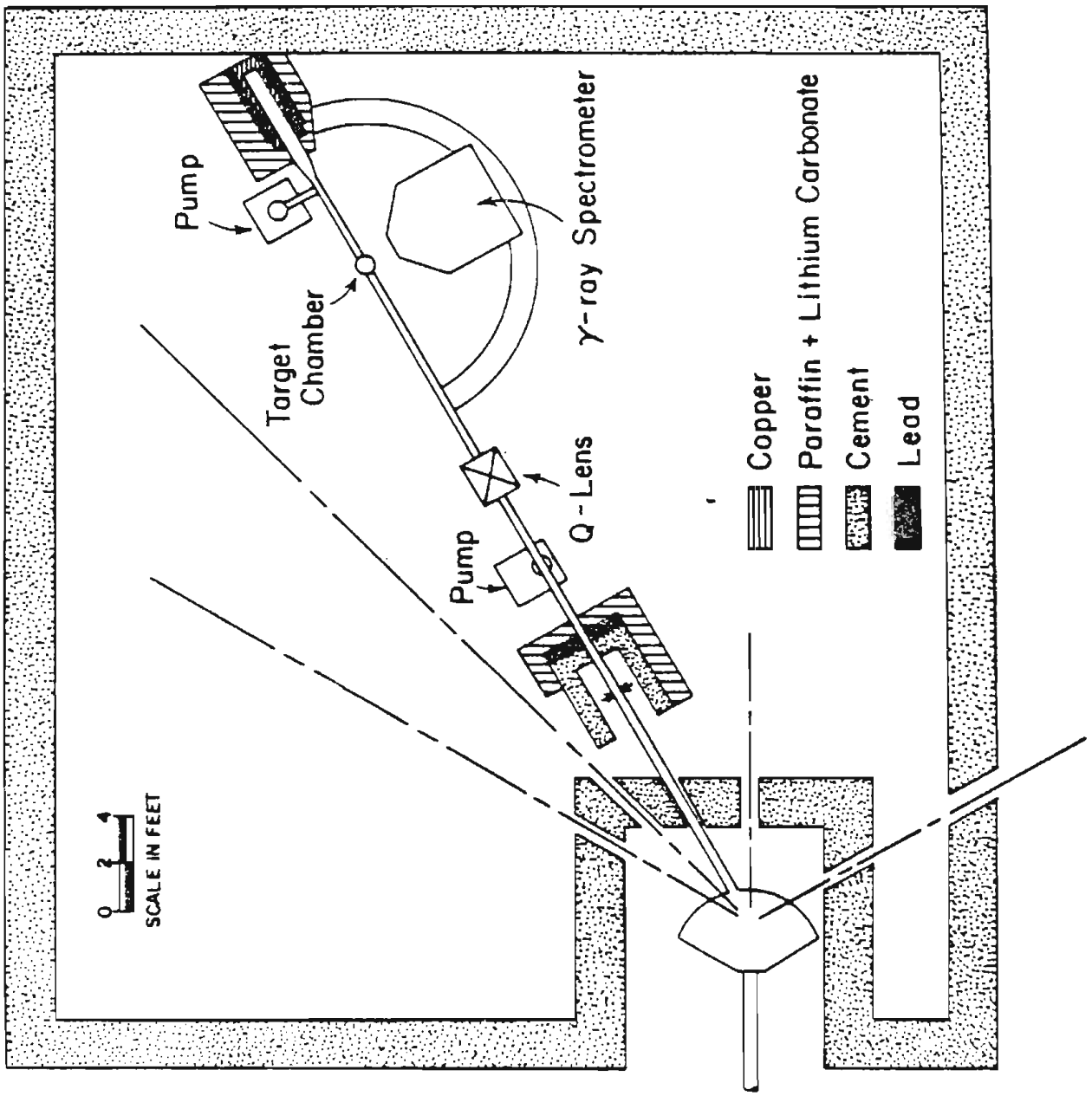
Pump
Target Chamber
γ-ray Spectrometer
Pump
Q-Lens
Copper
Paraffin + Lithium Carbonate
Cement
Lead
0 2 4
SCALE IN FEET

2.2 TARGETS

The carbon-13 targets used in this study were purchased from Penn Spectra Tech, Inc. of Wallingford, Pennsylvania. Data were taken with two sets of targets, each set consisting of two targets. One set, mounted on target rings with an aperture of three-eighths of an inch, was used to measure the excitation curve. The thickness of each of these targets was determined to be 270 ± 27 $\mu g/cm^2$ by measuring the energy loss of alpha particles emitted by an americium-241 source. A second set of two targets, mounted on frames with an aperture one half inch in diameter, was used to measure the angular distributions. The thickness of these targets was estimated to be approximately 255 ± 26 $\mu g/cm^2$ and 325 ± 33 $\mu g/cm^2$, respectively.

2.3 DETECTORS

The capture gamma rays observed in this study were detected with the NaI crystal and plastic shield assembly shown in figure 2. The 25.4 by 25.4 cm NaI crystal is enclosed in a stainless steel housing and is viewed by six RCA 8575 photomultiplier tubes. The crystal is surrounded on the front and sides by an anticoincidence shield (Suffert et al., 1968) of NE110 plastic. The shield is 7.6 cm thick in the front and 12.7 cm thick on the sides and is viewed by eight XP1031 photomultiplier tubes. Two of these tubes

Figure 2. Schematic diagram of the NaI crystal and shield assembly.

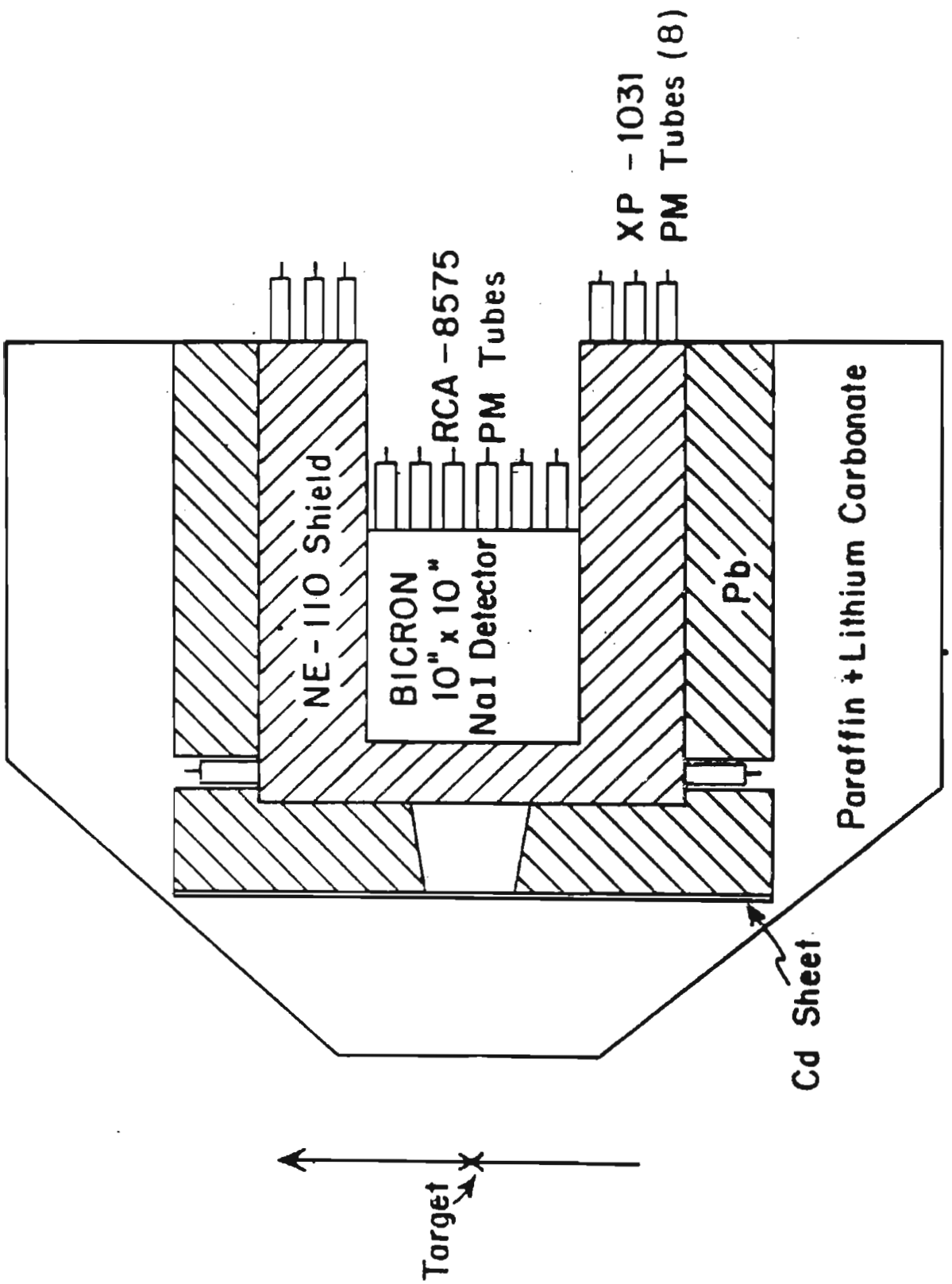
XP -1031
PM Tubes (8)
RCA-8575
PM Tubes
NE-110 Shield
BICRON
10" x 10"
NaI Detector
Pb
Paraffin + Lithium Carbonate
Cd Sheet
Target

are mounted on opposite sides of the front with the other six tubes being mounted on the back. In an effort to reduce the background counting rate, the entire assembly was shielded with 10 cm of lead and up to 20 cm of paraffin doped with lithium carbonate (50 % by weight). The front of the detector was also shielded with a sheet of cadmium one eighth of an inch in thickness. The back of the assembly was shielded by 20 cm of doped paraffin (not shown in the figure).

The capture gamma rays were collimated with either of two tapering lead collimators designed to fully illuminate the back face of the crystal at distances of 82 and 102 cm. The collimators were 20 cm thick and were fitted with a doped paraffin plug to reduce the neutron flux in the detector. The data for the excitation function were taken with the back face of the crystal 82 cm from the target, corresponding to a total angular acceptance of 17.6 degrees. The angular distributions of analyzing power and cross section were made with the back face of the crystal 102 cm from the target. This position allowed an angular range of 42 to 142 degrees and corresponds to a total angular acceptance of 14.2 degrees. Additional angular distribution measurements were made at angles ranging from 30 to 154 degrees with the back face of the crystal 145 cm from the target. These data were taken with the collimator designed for the 102 cm position.

Beam polarization and integrated charge were monitored throughout this study with two 2000 micron silicon surface barrier detectors mounted in the 15.5 cm scattering chamber. These detectors were mounted at fixed angles of plus and minus 160 degrees relative to the beam direction. The collimating system for these detectors consisted of a tantalum anti-scattering aperture 3.2 mm in diameter 4.3 cm from the target and a tantalum collimator with a 1.6 mm aperture 6.8 cm from the target, resulting in a solid angle of 0.43 msr for each detector.

2.4 ELECTRONICS AND DATA COLLECTION

The data-taking electronics system had two major functions: the processing of the linear energy signal from the crystal and the rejection of coincidence events in the crystal and shield. These latter events result from escape gamma rays from the crystal and cosmic radiation. The electronics system is outlined in the block diagram shown in figure 3. Special high-current transistorized tube bases were developed for use with the RCA 8575 photomultiplier tubes on the crystal. These bases were designed to improve gain stability under high count rate and variable count rate conditions. A schematic diagram of these tube bases is shown in figure 4. The gains of each of the tube and base systems were carefully matched by making fine adjustments to the high voltage applied to the individual tubes. The anode

Figure 3. Simplified block diagram of electronics used to process gamma ray events. Additional circuits used to measure dead time and accidental rates are not shown.

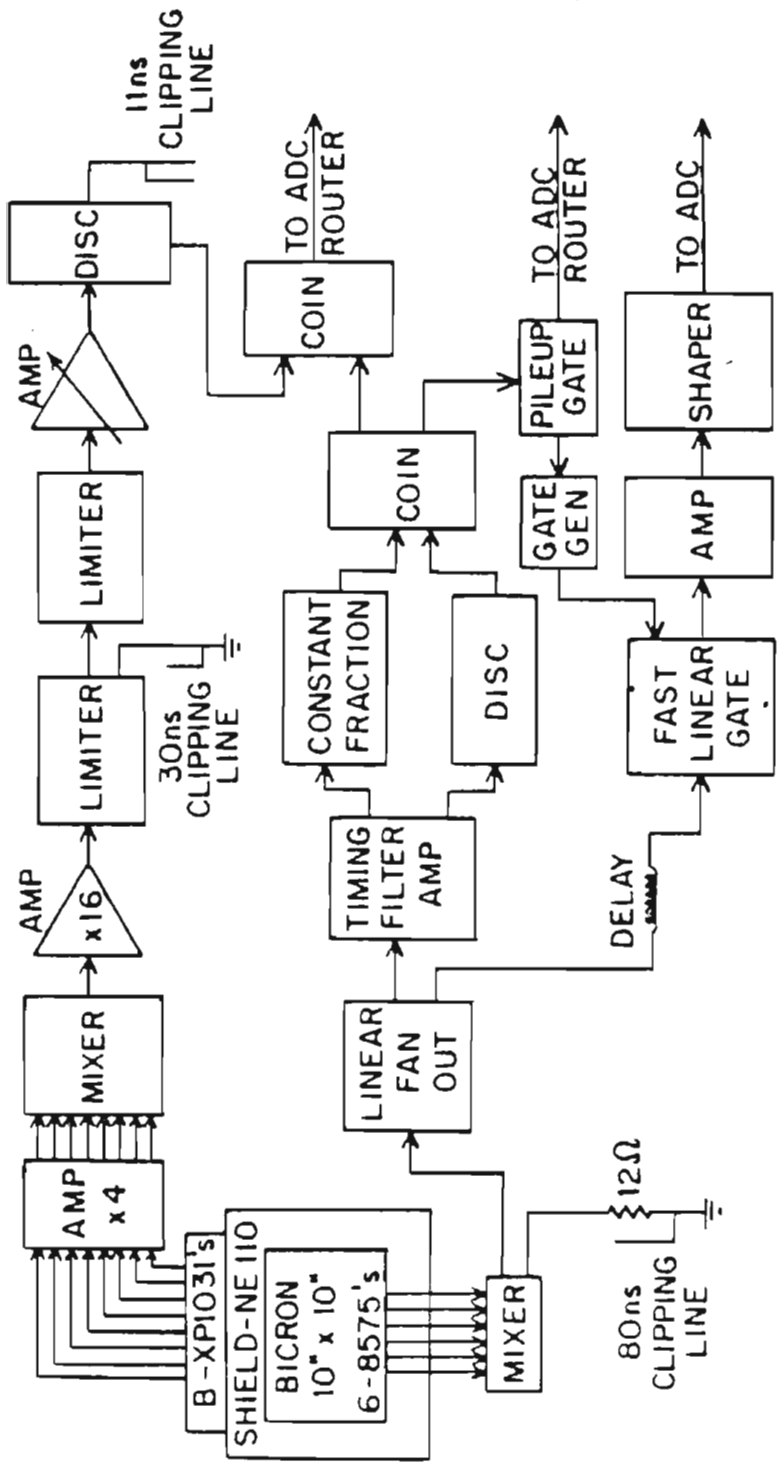
SHIELD-NE 110
B-XP1031's
BICRON
10" x 10"
6-8575's
AMP
x4
MIXER
AMP
x16
LIMITER
30ns
CLIPPING
LINE
LIMITER
AMP
DISC
11ns
CLIPPING
LINE
MIXER
12Ω
80ns
CLIPPING
LINE
LINEAR
FAN
OUT
TIMING
FILTER
AMP
CONSTANT
FRACTION
COIN
TO ADC
ROUTER
DISC
COIN
TO ADC
ROUTER
DELAY
GATE
GEN
PILEUP
GATE
FAST
LINEAR
GATE
AMP
SHAPER
TO ADC

Figure 4. Schematic diagram of the high-current transistorized photomultiplier tube bases.

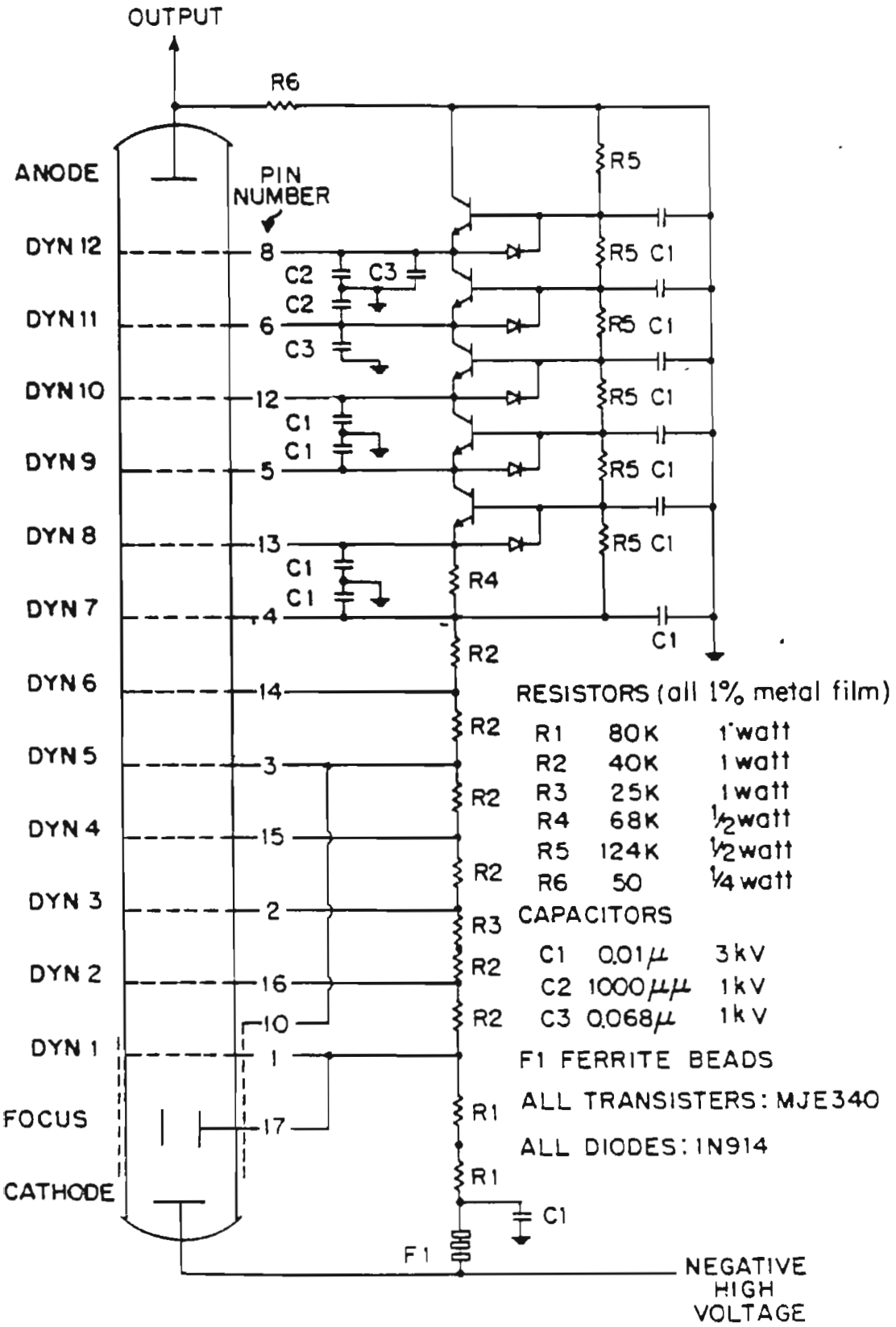

RESISTORS (all 1% metal film)

R1	80K	1 watt
R2	40K	1 watt
R3	25K	1 watt
R4	68K	½ watt
R5	124K	½ watt
R6	50	¼ watt

CAPACITORS

C1	0.01μ	3kV
C2	1000μμ	1kV
C3	0.068μ	1kV

F1 FERRITE BEADS

ALL TRANSISTERS: MJE340

ALL DIODES: 1N914

signals from the six tubes were summed with a mixer located in the target room. An 80 nanosecond long clipping line, terminated with a 12 ohm resistor, was used at the output of the mixer to produce a linear signal approximately 350 nanoseconds wide. This signal was transmitted to a linear fan-out located in the control room by RG-8 cable. A linear signal from this fan-out was sent to the analogue-to-digital-converter (ADC) after being passed through a delay, a fast linear gate, an amplifier, and a shaper. The fast linear gate was held open for only 400 ns to reduce the possibility of pileup. The delay allowed time for a trigger signal for the gate to be processed. A second linear signal from the fan-out was used to derive a timing signal for the linear gate and rejection circuits and to provide routing information to the ADC. This linear signal was amplified by a fast amplifier for parallel use by a fast leading edge discriminator (FLED) and a constant fraction discriminator (CFD). The output of these discriminators was then tested for an overlap coincidence. This circuit produces a pulse with good timing based on the CFD and with energy discrimination determined by the FLED. The output of the coincidence circuit was used in two ways. First, a pileup gate was used to generate the trigger for the linear gate and a routing pulse for the ADC. This pileup gate was held closed for 10 microseconds after each pulse to allow processing of the linear signal without pileup. The second

output of this coincidence circuit was used in the rejection circuit as discussed below.

The signals from the shield photomultiplier tubes were amplified before mixing. After mixing, the signal was amplified by a factor of sixteen and sent to a series of two limiters with the signal being clipped at the output of the first limiter with a 30 ns shorted cable. The output of this limiter circuit was connected to a variable amplifier in the control room by RG-8 cable. After amplification, the shield signal was directed to a fast discriminator. An 11 ns unterminated clipping line was used to increase the width of the discriminator output. The shield discriminator output was used in two ways. First, the output was tested with the output of the NaI coincidence circuit for an overlap coincidence. Such a coincidence indicated escape peak or cosmic radiation and routing information indicating the coincidence was directed to the ADC. The variable amplifier and fast discriminator levels could be adjusted to provide various rejection percentages of the first and second escape peaks. In general the discriminator level was set low enough to provide clear resolution of the peaks corresponding to the ground state and first excited state transitions from each other and from the low energy background. The second output of the shield discriminator was used to measure the rate of random rejection of good data events. Such accidental rejection lowers the apparent

cross section if appropriate corrections are not made. This accidental rate was measured by substantially delaying the NaI coincidence pulse and again testing it with the shield discriminator output for an overlap coincidence.

All data were collected and processed with an on-line DDP=224 computer. All events processed without a rejection pulse were stored in a true event spectrum and all events processed with a rejection pulse were stored in a separate rejected spectrum. When polarized beam was used, a separate set of true and rejected spectra was stored for each spin state.

The resolution of the system was a function of the counting rate and discriminator setting. Under ideal conditions , the system has achieved 2.4% resolution (Weller et al., 1976). Under typical conditions for this experiment, the resolution was 3-4%. A sample gamma ray spectrum is shown in figure 5 and has a resolution of 3.5%.

The beam current from the Faraday cup was integrated with an electronic current meter and three scalers. One scaler was ungated and measured the total charge accumulated during the run. The other two scalers were used to measure the live charge for the gamma ray and charged particle detector systems, respectively. Each of these scalers was gated off during the processing of an appropriate event. Additional scalers were used to monitor the operation of the system by measuring the true and accidental coincidence

Figure 5. A typical gamma ray spectrum obtained with the $^{13}C(p,\gamma)^{14}N$ reaction at E =12.0 MeV and a detector angle of 42.5 degrees. The solid curves represent fits to the spectrum described in chapter 3.

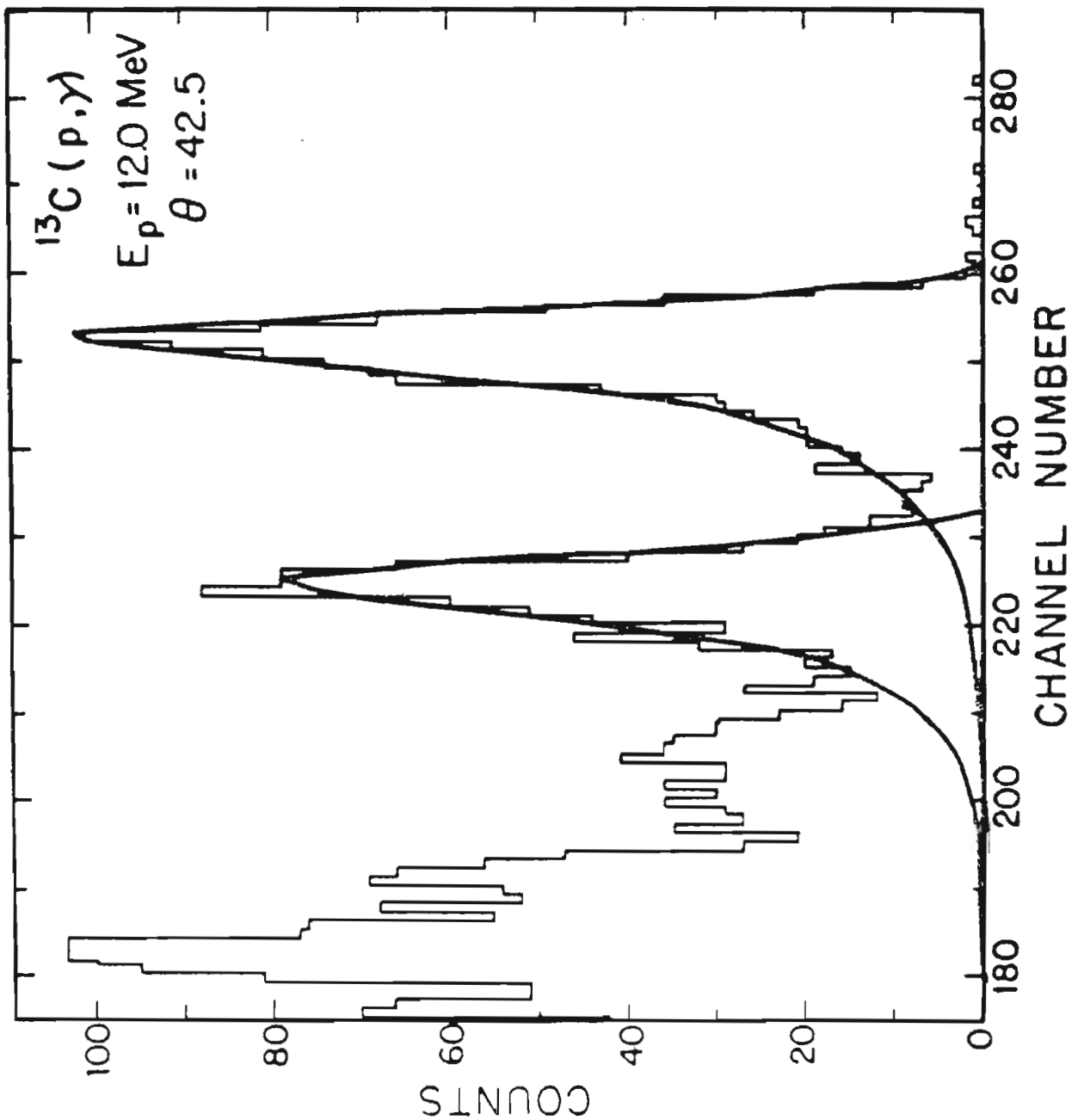
$^{13}C(p,\gamma)$
$E_p = 12.0$ MeV
$\theta = 42.5$
COUNTS
CHANNEL NUMBER
0
20
40
60
80
100
180
200
220
240
260
280

rates, as well as the individual NaI and shield counting rates. At the end of each run, the scaler readings were read into the computer and written onto magnetic tape along with the spectra.

Chapter III

DATA REDUCTION

3.1 FITTING, STRIPPING, AND SUMMING PROCEDURES

The off-line analysis of that data recorded on magnetic tape included fitting the various peaks to a standard lineshape. The lineshape used by the fitting routine was originally determined from the $T(p,\gamma)^4He$ reaction (McBroom, 1977) and was modified for use with $^{13}C(p,\gamma)$ spectra. The details of the fitting routine and procedure for modifing the lineshape are described in appendix 1. The tail of the peak corresponding to the ground state (γ_0) transitions and the tail of the peak of the first excited state (γ_1) transitions were incompletely resolved and unfolding was required. Figure 5 in chapter 2 shows a typical fit to γ_0 and γ_1. The average width of the peaks increased slowly with energy throughout the region studied; the widths of γ_0 and γ_1 were approximately the same.

The efficiency of the NaI crystal system depends upon the rejection threshold as well as the width of the region of the spectrum summed or fitted. The efficiency (probability that a photon will be recorded if it reaches the crystal) was determined by measuring the $^{12}C(p,\gamma)$ thick target (50 keV for 14.2 MeV protons) yield over the 15.07

MeV resonance in ^{13}N. This yield, along with the recent measurement (Mans et al., 1975) of the number of gamma rays per proton $(6.83\pm0.22)\times10^{-9}$, was used to determine the efficiency. The value obtained was $\varepsilon=0.168\pm0.011$, when the peak was summed in the full-energy region. It is assumed that the efficiency remains constant for all gamma ray energies involved in the present study. The γ_0 90 degree yield curve was obtained by summing the data in a window of fixed width in a manner consistent with the efficiency measurement. The γ_0 peak was fitted and stripped to allow a similar sum of the γ_1 peak.

The angular distribution measurements involved the analysis of several spectra with essentially the same gamma ray energies. These peaks were all fitted with a fixed width obtained from an average of the individual widths. The γ_0 peak was fitted with the appropriate width and stripped from the data spectrum. The γ_1 peak could then be fitted in the residual spectrum. After both peaks were fitted, the sum of the fits was compared to the original data spectrum to determine the accuracy of the fitting procedure.

3.2 NORMALIZATION TO MONITOR DETECTORS

The elastically scattered protons were observed by charged particle detectors located at plus and minus 160 degrees relative to the beam direction. The yield measured

in these fixed detectors was used to verify the uniformity of charge integration and target thickness. In general, the elastic proton yield was consistent to better than 1 percent and no corrections to the integrated charge were required. The asymmetry measured with the two detectors was used to monitor the beam polarization. The analyzing power, which is the asymmetry divided by the beam polarization, was calculated for the elastically scattered protons for each spin state to verify the polarization as obtained from the quench ratio measurement. In general, the deviations were smaller than the error in the quench ratio measurement. For this reason, it was unnecessary to make corrections to the data.

3.3 CORRECTIONS FOR ACCIDENTAL COINCIDENCES AND BACKGROUND

The rate of accidental coincidences between the NaI crystal and the shield was measured for each data point as described in chapter 2. In general, the rate was 3 to 8 percent of the true coincidences with the high values occurring at forward angles (<50 degrees). The yields were corrected for this effect. The count rate in the NaI detector was consistently maintained below 80,000 counts per second.

The off-line analysis included the calculation of a background contribution obtained by averaging a portion of the spectrum above the γ_0 peak. In general, this

contribution was very small and could be neglected. However, at extreme angles or poor beam conditions (for example, excessive collimator current) this contribution was finite and appropriate corrections were made.

Chapter IV

EXCITATION FUNCTIONS

4.1 YIELD CURVE FOR THE $^{13}C(p,\gamma_0)^{14}N$ REACTION

The yield at 90 degrees was measured for the $^{13}C(p,\gamma_0)^{14}N$ reaction at proton energies ranging from 6.25 to 17.0 MeV. Data were taken in 200 keV steps for proton energies ranging from 6.25 to 13.6 MeV and in 100 Kev steps from 13.6 to 17.0 MeV. Additional data were taken in 50 Kev steps at proton energies ranging from 12.6 to 14.55 MeV to investigate structure reported in this energy region. The results of these measurements are shown in figure 6 with error bars representing the statistical errors. The cross section was obtained from measurements of the target thickness, integrated yield, and detector efficiency and has an overall uncertainty of 12 percent. The cross section extracted from the present data is approximately 40 percent smaller than the results reported by Reiss, O'Connell, and Paul (1971). However, comparison of our results to the $^{14}N(\gamma,p_0)^{13}C$ measurements made by Baglin, Bentz, and Carr (1974) through the process of detailed balance shows the present cross section larger by approximately 15 percent. The data of Reiss, Paul, and O'Connell were reported in this latter reference to be in agreement with the (γ,p_0) measurement.

Figure 6. The 90 degree yield curve obtained with the $^{13}C(p,\gamma_0)^{14}N$ reaction. The incident proton energy is given on the lower scale and the gamma ray energy is given on the scale at the top of the figure.

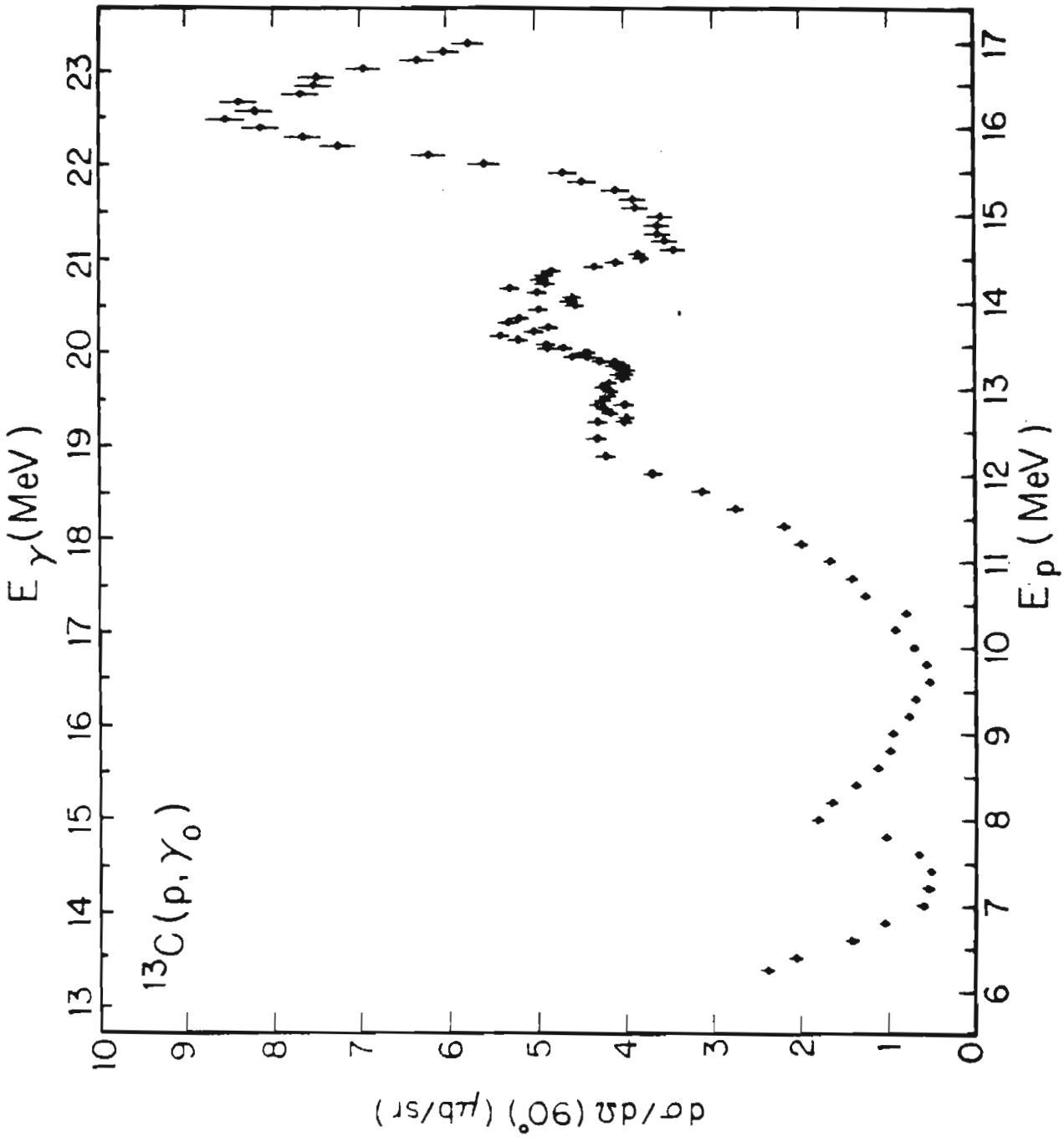
$^{13}C(p,\gamma_0)$
E_γ(MeV)
E_p (MeV)
$d\sigma/d\Omega$ (90°) (μb/sr)

This now appears to be in error. To further check this point, measurements of the $^{13}C(d,\gamma_0)^{15}N$ cross section were made using the same targets and detector system and are in excellent agreement with the measurements of this cross section reported by Del Bianco, Kundu, and Kim (1976). These $^{13}C(d,\gamma_0)^{15}N$ cross section measurements are also in good agreement with measurements of the $^{15}N(\gamma,d_0)^{13}C$ reaction made by Skopik et al. (1978). The agreement of the measured (d,γ) cross section with two independent measurements adds confidence to the cross section extracted from the present data.

All measurements of the $^{14}N(\gamma,p_0)$ cross section reveal basically similar shapes. Figure 7 shows a plot of data from the present experiment, the data of Reiss, O'Connell, and Paul (1971) and the data of Paul, Kuan, and Warburton (1975). These data were converted from the (p,γ_0) to the (γ,p_0) cross sections through detailed balance (Hayward, 1970). The $^{14}N(\gamma,p_0)^{13}C$ data of Baglin, Bentz and Carr (1974) and the $^{14}N(\gamma,n_0)^{13}N$ data of Gellie et al. (1972) are also presented in figure 7. The two distinct peaks observed by Reiss and coworkers between 22.0 and 23.5 MeV excitation are not reproduced in the other data. Although the resolution reported for the data of Baglin, Bentz and Carr and of the present data (the combined effects of target thickness and beam energy fluctuations are less than 50 Kev over the region studied) is more than sufficient to observe

Figure 7. Comparison of various measurements of the 90 degree cross section for the $^{14}N(\gamma,p_o)$ reaction. The $^{14}N(\gamma,n_o)^{13}N$ 90 degree yield curve obtained by Gellie et al. is also shown. These data are discussed in the text.

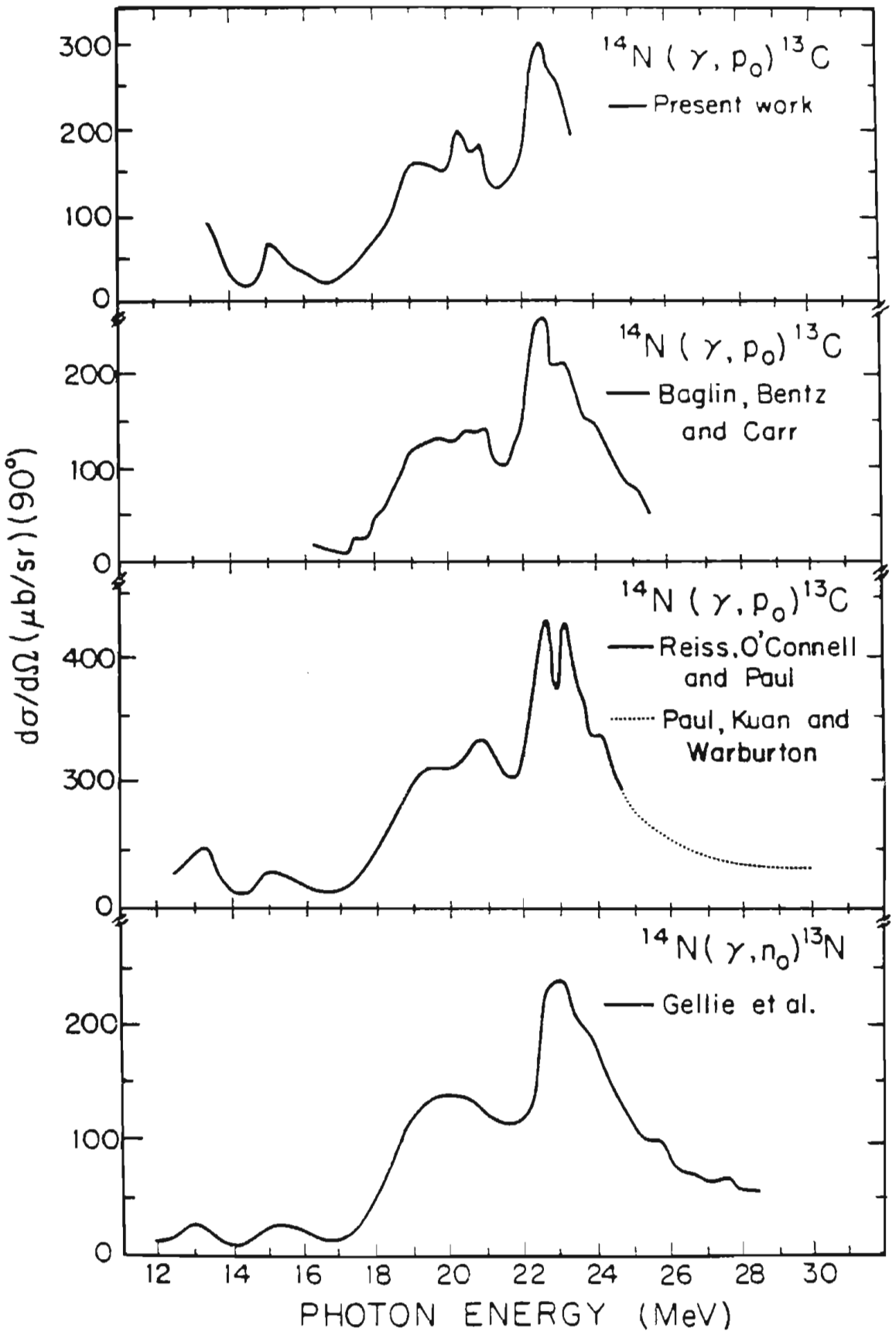
$^{14}N(\gamma, p_0)^{13}C$
— Present work
$^{14}N(\gamma, p_0)^{13}C$
— Baglin, Bentz and Carr
$^{14}N(\gamma, p_0)^{13}C$
— Reiss, O'Connell and Paul
····· Paul, Kuan and Warburton
$^{14}N(\gamma, n_0)^{13}N$
— Gellie et al.
$d\sigma/d\Omega$ (μb/sr) (90°)
PHOTON ENERGY (MeV)

such detailed structure, only a single peak with a somewhat broadened shoulder is seen.

The dip in the cross section near a proton energy of 14.0 MeV (an excitation energy of 20.6 MeV) is an interesting feature. Weller et al. (1978) report a peak at this energy in the $^{13}C(p,p)^{13}C$ cross section observed at a center of mass angle of 89.4 degrees. Similar correlated features were observed in the $^{12}C(p,\gamma_0)^{13}N$ reaction by Hasinoff, Johnson, and Measday (1972). In this case two such minima were related to levels in ^{13}N. Destructive interference of this kind could account for the minimum in the $^{13}C(p,\gamma_0)^{14}N$ reaction at 20.6 MeV excitation.

4.2 YIELD CURVE FOR THE $^{13}C(P,\gamma_1)^{14}N$ REACTION

The yield at 90 degrees for the (p,γ_1) reaction was measured at the same proton energies as the (p,γ_0) reaction described above. The first excited state is located at 2.313 MeV excitation in ^{14}N. The peak corresponding to the ground state transition was fitted and stripped from the spectrum as described in chapter 3. In principle, the amount of tail from the γ_0 peak subtracted from the region of the γ_1 peak should be related to the size of the γ_0 peak. Figure 8 shows a plot of the tail subtracted by the fitting routine from the region of the γ_1 peak as a function of energy. The solid line is a scaled drawing of the (p,γ_0) yield curve shown in figure 6. The agreement is excellent

Figure 8. Plot of the amount of tail from the γ_0 peak in the gamma ray spectrum removed from the region of the γ_1 peak as a function of energy. The solid line is a scaled drawing of the $^{13}C(p,\gamma_0)^{14}N$ yield curve shown in figure 6.

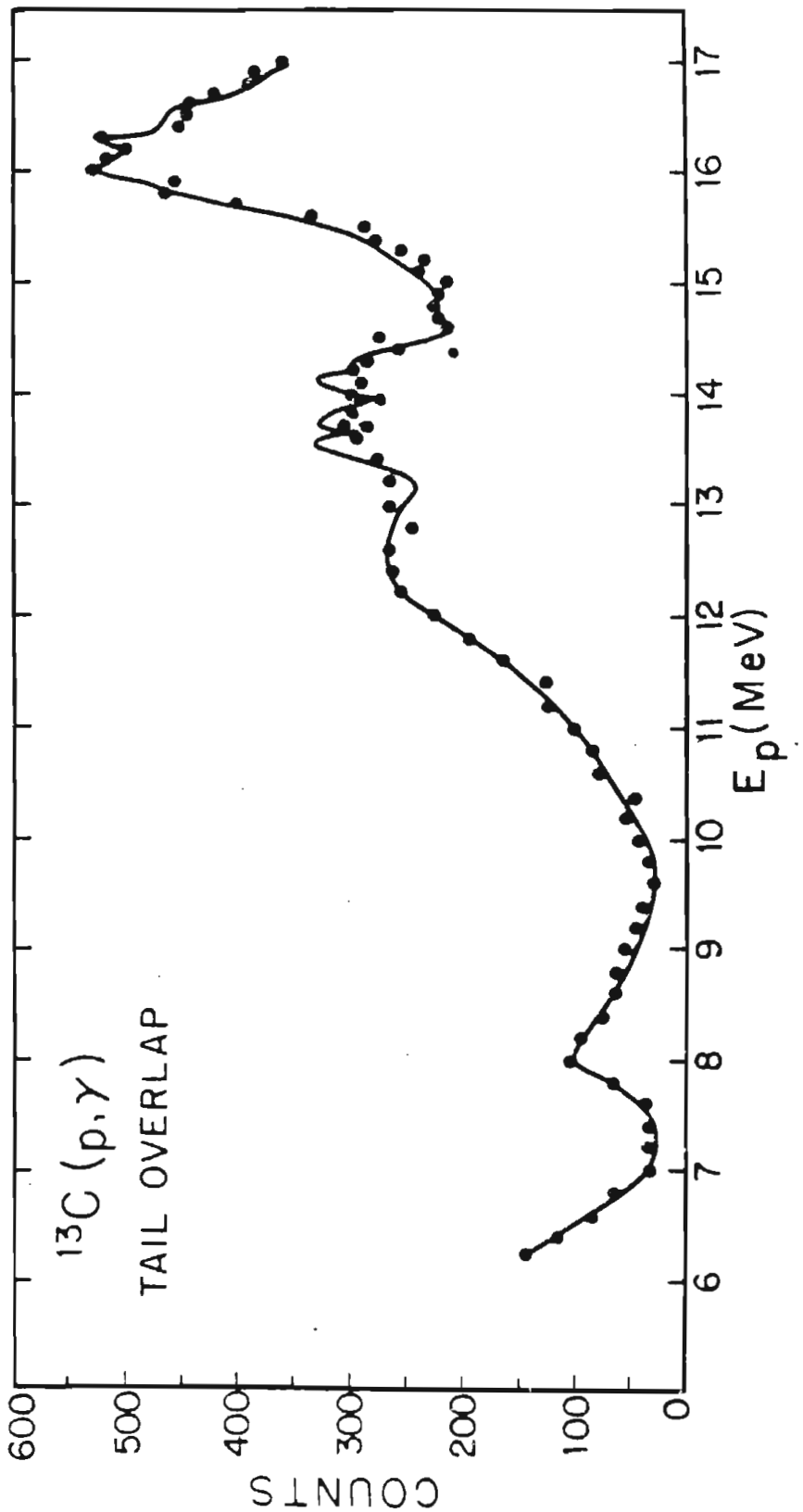
$^{13}C(p,\gamma)$
TAIL OVERLAP
COUNTS
E_p(MeV)
0
100
200
300
400
500
600
6
7
8
9
10
11
12
13
14
15
16
17

and indicates that the peak fitting routine unfolds the spectra in a consistent fashion. The γ_0 tail subtracted from the full energy region of the γ_1 peak represents approximately 15 percent of the (p,γ_0) yield obtained with a sum of the full energy region of the γ_0 peak. The spectrum shown in figure 5 has a tail overlap of approximately 6 percent. Spectra taken for the yield curve show slightly broader peaks and more counts in the valley between the peaks. The differences in the tail overlap reflect these differences in the spectra. An overall uncertainty of 20 percent is assigned to the (p,γ_1) cross section and includes an estimate of the uncertainty in the tail overlap.

The $^{13}C(p,\gamma_1)^{14}N$ yield curve is presented in figure 9. The curve is relatively smooth and exhibits a shape characteristic of the giant dipole resonance (built on the first excited state). The present results are compared to the combined results obtained by Reiss, O'Connell, and Paul (1971) and by Paul, Kuan, and Warburton (1975) in figure 10. The shapes of the two yield curves disagree rather substantially. These differences could arise from the background and pile-up problems present in the data of Reiss, O'Connell, and Paul. Thus the present data indicate that the dipole strength observed through the (p,γ_1) channel is centered at a slightly lower energy than suggested by the earlier data.

Figure 9. The 90 degree yield curve obtained with the $^{13}C(p,\gamma_1)^{14}N$ reaction. The incident proton energy is given on the lower scale and the gamma ray energy is given on the scale at the top of the figure.

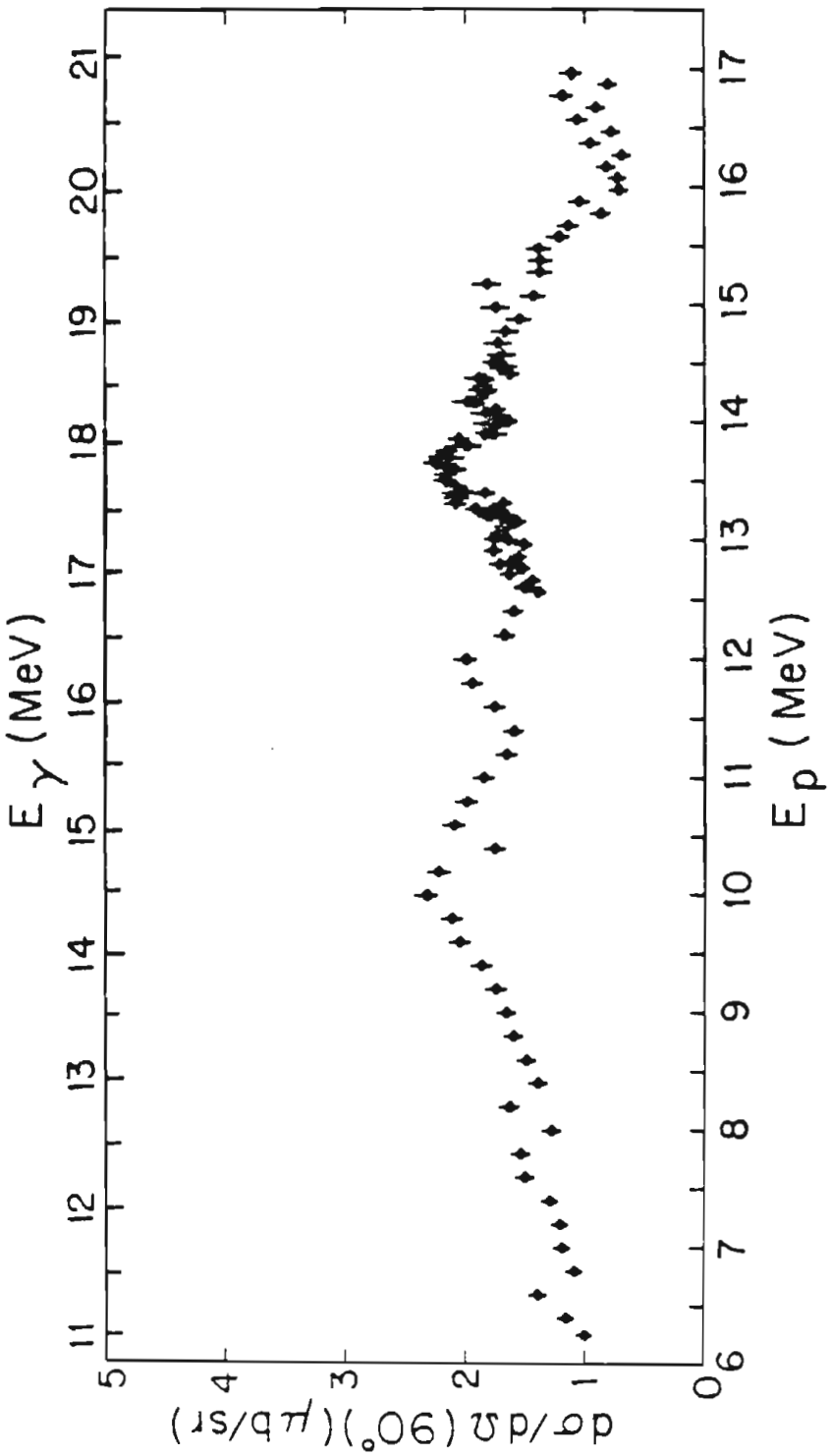
dσ/dΩ (90°) (μb/sr)
0
1
2
3
4
5
6
7
8
9
10
11
12
13
14
15
16
17
E γ (MeV)
11
12
13
14
15
16
17
18
19
20
21
E p (MeV)

Figure 10. Plots of the 90 degree yield curves obtained with the $^{13}C(p,\gamma_1)^{14}N$ reaction. The present results are compared to the combined results of Peiss, O'Connell and Paul and Paul, Kuan, and Warburton. The results of a calculation made for this nucleus by Vergados are shown in the top portion of the figure. Vertical bars representing Γ_γ / E_ρ for 1- T=0 states (solid bars) and 1- T=2 states (dashed bars) are plotted as a function of energy.

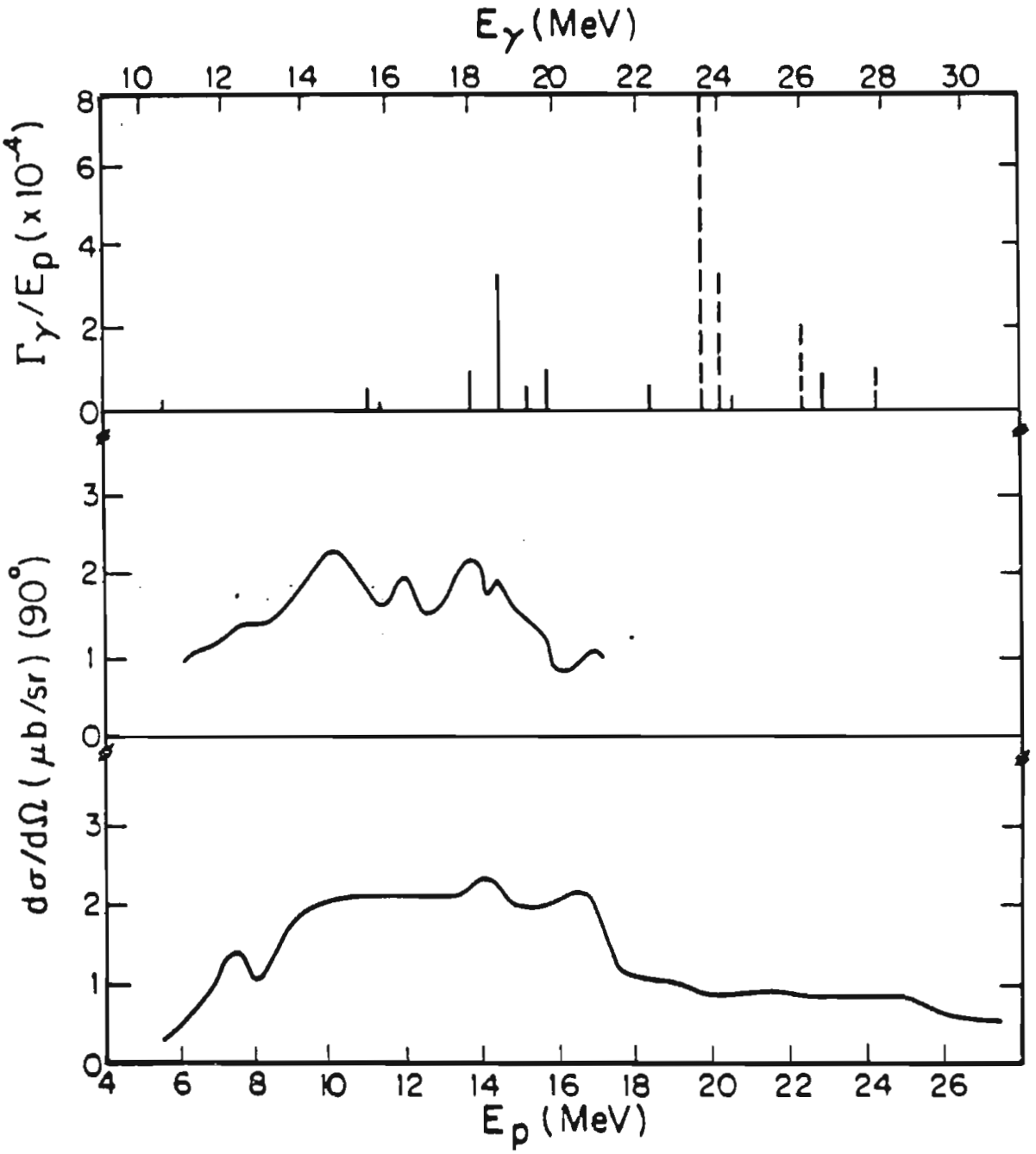
E_γ (MeV)
10 12 14 16 18 20 22 24 26 28 30
Γ_γ/E_p ($\times 10^{-4}$)
0 2 4 6 8
$d\sigma/d\Omega$ (μb/sr) (90°)
0 1 2 3
0 1 2 3
4 6 8 10 12 14 16 18 20 22 24 26
E_p (MeV)

Isospin selection rules allow transitions from T=0 and T=2 giant dipole states to this first excited state with T=1 (Warburton and Weneser, 1969). The spin and parity of 0+ of this state demands that all E1 transitions arise from states with spin and parity of 1-. Vergados (1975) has calculated the location and strength of the 1- T=0 and 1- T=2 states in ^{14}N. The results of this calculation are shown in figure 10 as vertical bars representing Γ_δ/E_p. Solid bars represent the T=0 states and dashed bars represent T=2 states. Although the formation of T=2 states in ^{14}N through the (p,γ) channel is isospin forbidden, such resonances have been observed in other nuclei for cases where the gamma decay is isospin allowed. The present data have their strength centered in approximately the same location as the calculation for T=0 states, but the strength is more uniformly distributed.

Chapter V

ANGULAR DISTRIBUTION ANALYSIS

5.1 FITS TO LEGENDRE POLYNOMIALS

Angular distributions of cross section and analyzing power were measured at twelve energies ranging from 8.05 to 15.5 MeV. These data and the fits described below are shown in figures 11,12,13 and 14. Cross section measurements were made at detector angles of 30,42,55,70,90,110,125,142 and 154 degrees. Data at the most extreme angles (30 and 154 degrees) were taken with unpolarized beam and the detector placed at the 145 cm position. Unpolarized beam was used for these latter measurements because greater beam intensity was required due to the combined effects of reduced solid angle and yield at these extreme angles, and because measurements of the analyzing power at these angles was not required to determine the coefficient b_4 with statistical significance (see below). The cross section data are plotted as $\sigma(\theta)/A_0$ where, for the measurements with polarized beam,

$$\sigma(\theta) = N_+ + N_-$$

and N_+ and N_- are the yields for spin up and spin down, respectively. The definition of A_0 will be given below.

Figure 11. Angular distributions of cross section and analyzing power obtained from the $^{13}C(p,\gamma_0)^{14}N$ reaction for incident proton energies of 8.05, 9.0, 10.0, 10.95, 12.0, and 12.5 MeV. The error flags reflect the statistical error associated with the data points. The solid curves indicate the fits to the data including all polynomials through fourth order, as described in the text.

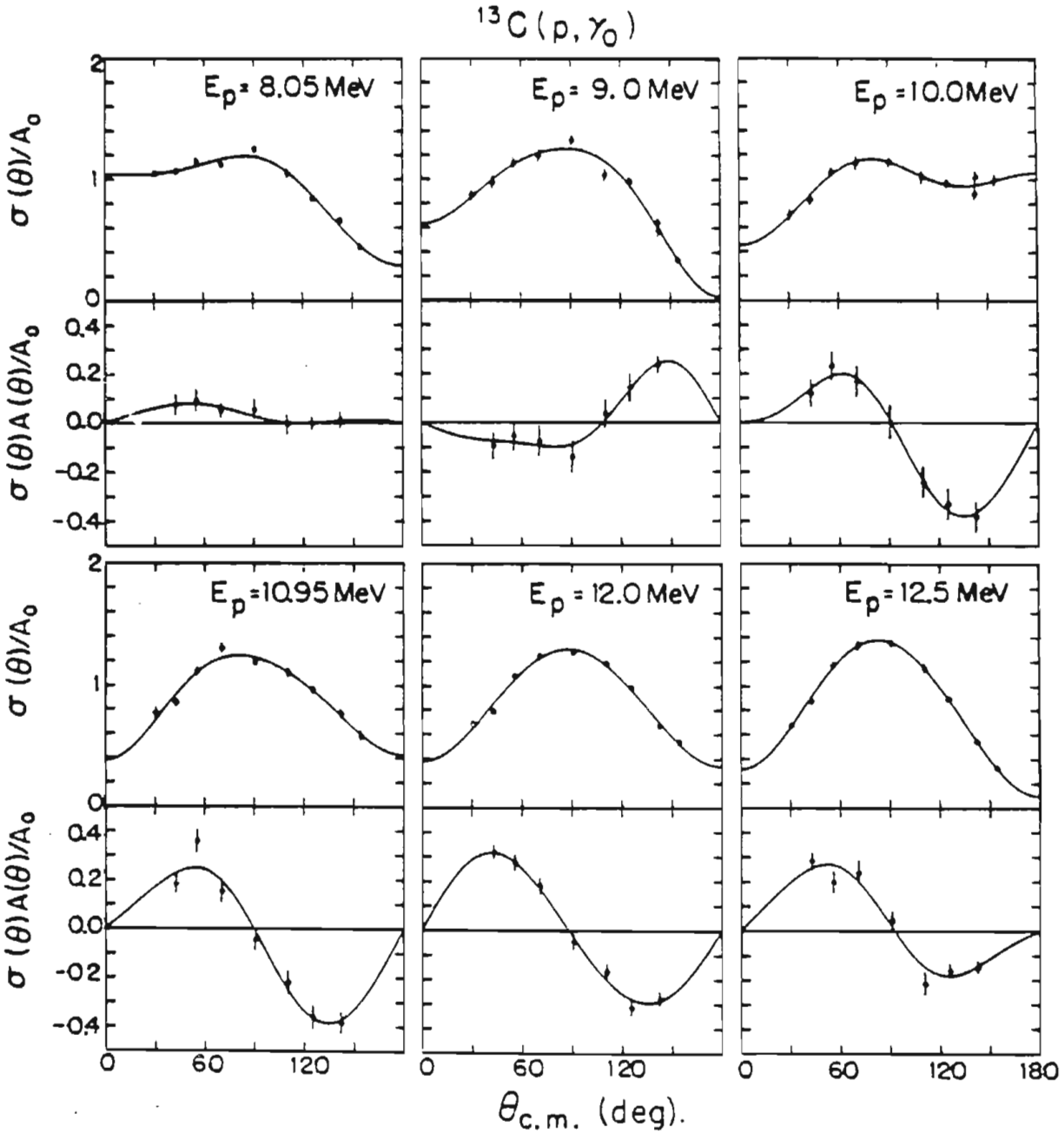
$^{13}C(p,\gamma_0)$
E_p= 8.05 MeV
E_p= 9.0 MeV
E_p =10.0MeV
E_p=10.95 MeV
E_p = 12.0 MeV
E_p= 12.5 MeV
$\sigma(\theta)/A_0$
$\sigma(\theta)A(\theta)/A_0$
$\theta_{c.m.}$ (deg).

Figure 12. Angular distributions of cross section and analyzing power obtained from the $^{13}C(p,\gamma_0)^{14}N$ reaction for incident proton energies of 13.0, 13.5, 14.0, 14.5, 15.0, and 15.5 MeV. The error flags reflect the statistical error associated with the data points. The solid curves indicate the fits to the data including all polynomials through fourth order, as described in the text.

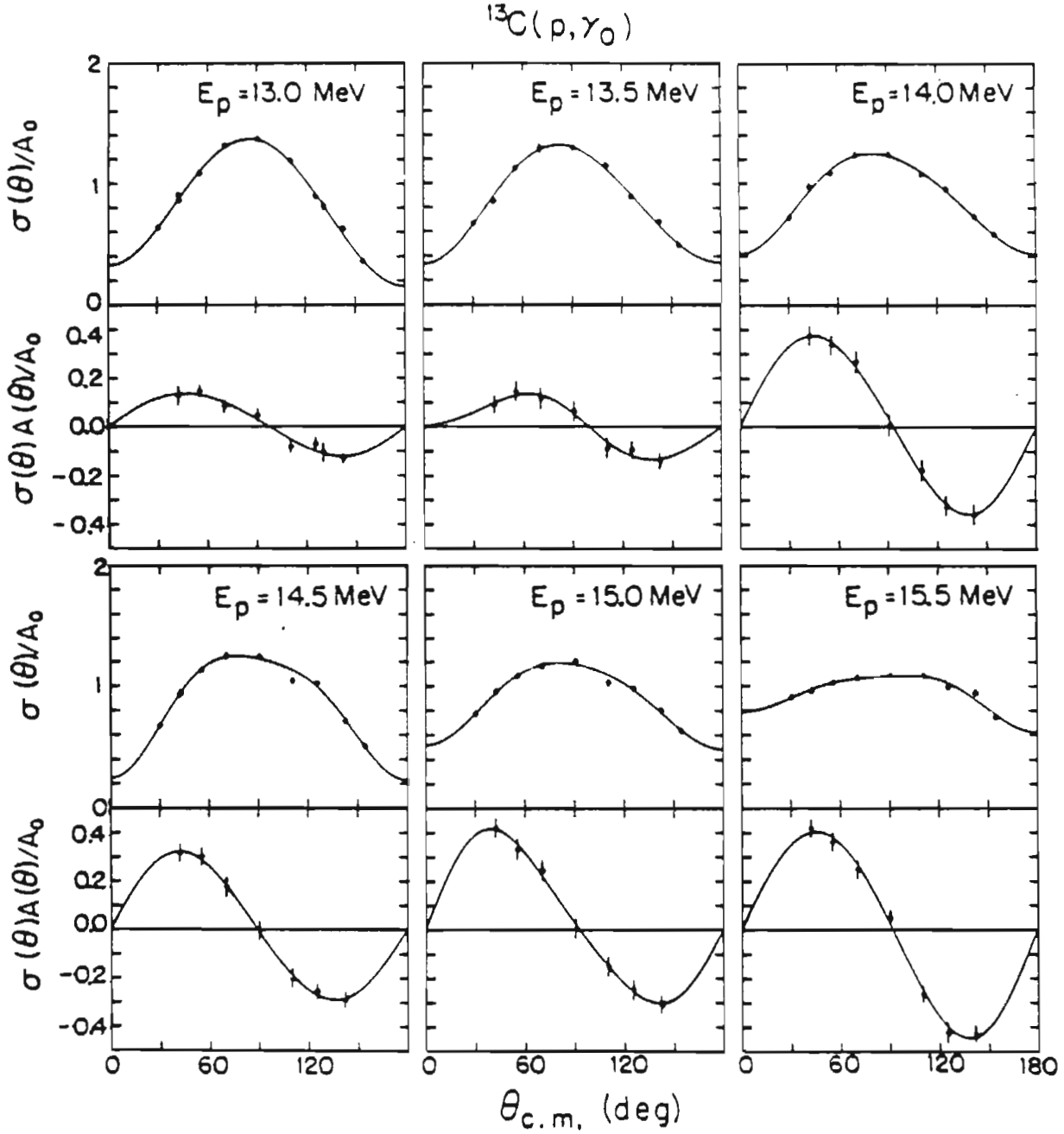
$^{13}C(p,\gamma_0)$
E_p = 13.0 MeV
E_p = 13.5 MeV
E_p = 14.0 MeV
E_p = 14.5 MeV
E_p = 15.0 MeV
E_p = 15.5 MeV
$\sigma(\theta)/A_0$
$\sigma(\theta)A(\theta)/A_0$
$\theta_{c.m.}$ (deg)

Figure 13. Angular distributions of cross section and analyzing power obtained from the $^{13}C(p,\gamma_1)^{14}N$ reaction for incident proton energies of 8.05, 9.0, 10.0, 10.95, 12.0, and 12.5 MeV. The error flags reflect the statistical error associated with the data points. The solid curves indicate the fits to the data including all polynomials through fourth order, as described in the text.

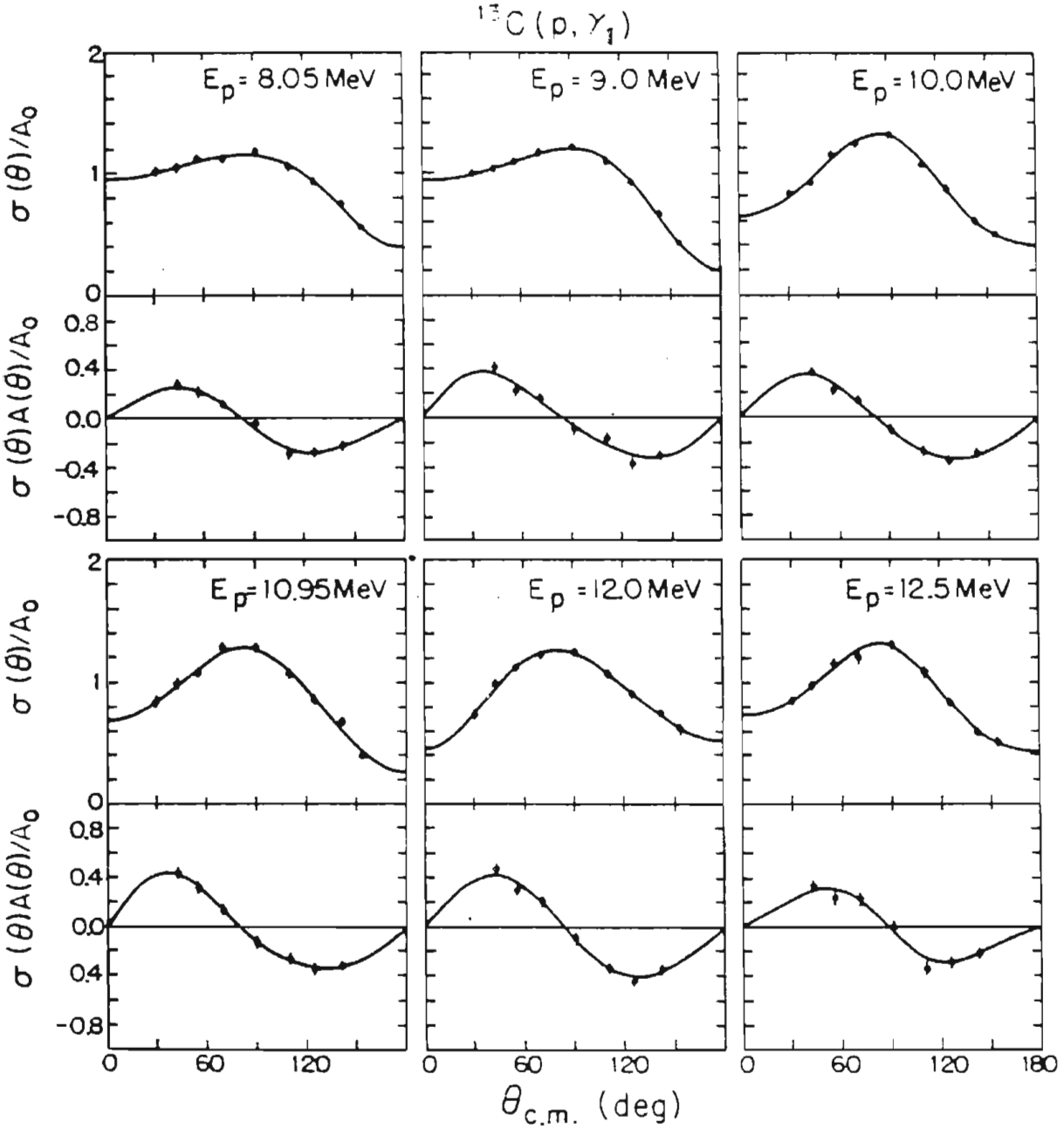
$^{13}C(p,\gamma_1)$
E_p = 8.05 MeV
E_p = 9.0 MeV
E_p = 10.0 MeV
E_p = 10.95 MeV
E_p = 12.0 MeV
E_p = 12.5 MeV
$\sigma(\theta)/A_0$
$\sigma(\theta)A(\theta)/A_0$
$\theta_{c.m.}$ (deg)

Figure 14. Angular distributions of cross section and analyzing power obtained from the $^{13}C(p,\gamma_1)^{14}N$ reaction for incident proton energies of 13.0, 13.5, 14.0, 14.5, 15.0 and 15.5 MeV. The error flags reflect the statistical error associated with the data points. The solid curves indicate the fits to the data including all polynomials through fourth order, as described in the text. A fit through third order was performed for the analyzing power data at 14.0 MeV because of the unphysical nature of the fourth order fit. This fit is represented by a dashed line.

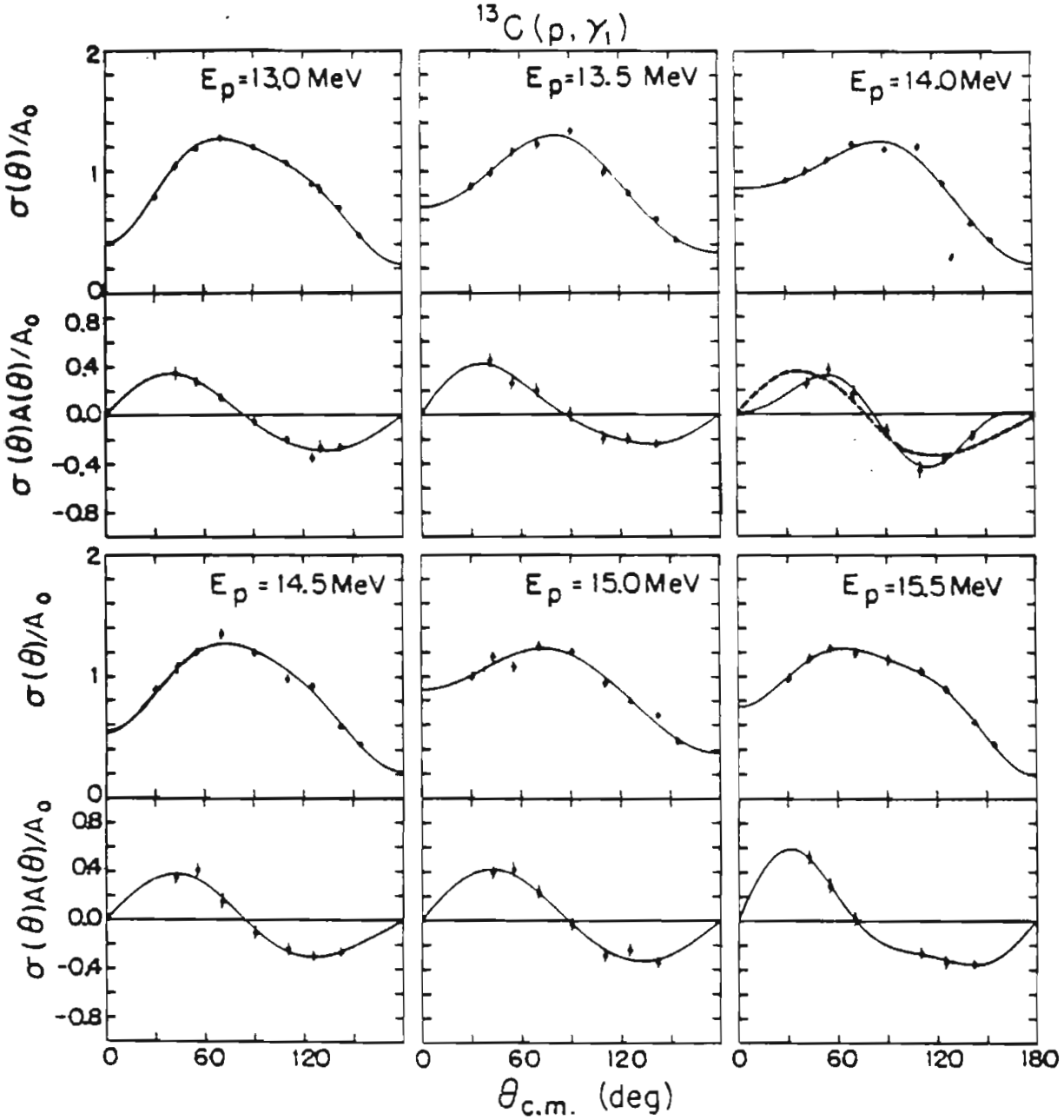
$^{13}C(p,\gamma_1)$
E_p=13.0 MeV
E_p=13.5 MeV
E_p=14.0MeV
E_p = 14.5MeV
E_p = 15.0MeV
E_p=15.5MeV
$\sigma(\theta)/A_0$
$\sigma(\theta)A(\theta)/A_0$
$\theta_{c.m.}$ (deg)

The angular distributions of center of mass cross section were fitted using a least squares procedure to an expansion of Legendre polynomials of the form

$$\sigma(\theta) = A_0 \left[1 + \sum_{k=1} a_k Q_k P_k(\cos(\theta)) \right] \quad ,$$

where the coefficients Q_k correct for the finite detector size and $a_0 = 1$. The fits through k = 4 are shown as solid lines in figures 11 through 14. Tables 1 and 2 list the normalized values of the coefficients for the ground state and first excited state transitions, respectively. The errors reflect the statistical error in the original data. The tables also include the normalized chi-squared. Coefficients of fits through third order fall within the errors of the coefficients from the fourth order fits. The normalized a_k coefficients derived from the fits through P_4 are plotted in figures 15 and 16.

The analyzing power measurements were made at detector angles of 42,55,70,90,110,125 and 142 degrees. All of these measurements were made with polarized beam and the detector placed at the 102 cm position. The angular distributions of analyzing power are plotted as $\sigma(\theta) A(\theta) / A_0$, where

$$A(\theta) = \left(\frac{N_+ - N_-}{N_+ + N_-} \right) \frac{1}{P} \quad ,$$

and P is the beam polarization. The errors on the data points reflect the statistical error in the original data and the possible error in the beam polarization.

Table 1-A. The a_k Coefficients Obtained from the $^{13}C(p,\gamma_0)^{14}N$ Reaction

E_p	$4\pi A_0$	a_1	a_2	a_3	a_4	χ^2
8.05	17.9±0.8 mb	0.28±0.01	-0.36±0.02	0.11±0.03	0.02±0.03	4.8
9.00	8.9±0.5 mb	0.21±0.02	-0.58±0.03	0.10±0.04	-0.10±0.05	2.2
10.00	7.5±0.6 mb	-0.09±0.02	-0.28±0.04	-0.22±0.05	0.03±0.06	1.0
10.95	17.3±0.7 mb	0.06±0.02	-0.52±0.03	-0.08±0.04	-0.08±0.05	3.1
12.00	36.3±1.0 mb	0.04±0.01	-0.63±0.02	-0.02±0.03	-0.02±0.03	4.4
12.50	40.1±1.1 mb	0.17±0.01	-0.76±0.02	-0.06±0.03	-0.04±0.03	0.7
13.00	39.1±0.9 mb	0.12±0.01	-0.75±0.01	-0.03±0.02	-0.02±0.02	3.2
13.50	47.7±1.1 mb	0.10±0.01	-0.64±0.02	-0.10±0.02	-0.03±0.03	1.6
14.00	46.9±1.1 mb	0.08±0.01	-0.52±0.01	-0.08±0.02	-0.07±0.03	1.6
14.50	38.6±1.1 mb	0.07±0.01	-0.59±0.02	-0.06±0.02	-0.18±0.03	3.1
15.00	37.8±1.5 mb	0.06±0.01	-0.43±0.02	-0.05±0.02	-0.08±0.03	2.1
15.50	54.9±2.0 mb	0.04±0.01	-0.23±0.02	0.05±0.02	-0.07±0.03	3.5

Table 1-B. The b_k Coefficients Obtained from the $^{13}C(p,\gamma_0)^{14}N$ Reaction

E_p	b_1	b_2	b_3	b_4	χ^2
8.05	0.04±0.02	0.03±0.01	0.01±0.01	0.00±0.01	0.2
9.00	-0.02±0.03	-0.09±0.02	0.05±0.02	-0.02±0.02	0.4
10.00	-0.06±0.03	0.19±0.02	-0.05±0.02	-0.02±0.02	0.3
10.95	-0.04±0.02	0.21±0.01	-0.03±0.01	-0.01±0.01	2.8
12.00	-0.01±0.01	0.20±0.01	0.01±0.01	0.01±0.01	1.0
12.50	0.04±0.02	0.15±0.01	0.01±0.01	-0.02±0.01	2.4
13.00	0.02±0.01	0.08±0.01	-0.01±0.01	0.00±0.01	0.9
13.50	0.02±0.02	0.08±0.01	-0.02±0.01	-0.01±0.01	0.5
14.00	0.03±0.02	0.24±0.01	-0.01±0.01	0.01±0.01	0.3
14.50	0.01±0.02	0.20±0.01	0.01±0.01	0.01±0.01	0.2
15.00	0.05±0.02	0.23±0.01	0.01±0.01	0.02±0.01	0.3
15.50	0.01±0.02	0.28±0.01	-0.02±0.01	0.01±0.01	0.8

Table 2-A. Table of a_K Coefficients Obtained from the $^{13}C(p,\gamma_1)^{14}N$ Reaction

E_p	$4\pi A_o$	a_1	a_2	a_3	a_4	X^2
8.05	13.7±0.8 mb	0.20±0.01	-0.31±0.02	0.09±0.03	-0.03±0.04	1.1
9.00	17.2±0.8 mb	0.23±0.01	-0.41±0.02	0.14±0.03	-0.03±0.04	0.5
10.00	22.3±1.0 mb	0.18±0.01	-0.55±0.02	-0.05±0.03	0.08±0.03	1.2
10.95	18.1±0.9 mb	0.20±0.02	-0.54±0.03	-0.01±0.04	0.01±0.04	2.8
12.00	20.1±0.9 mb	0.10±0.02	-0.49±0.03	-0.13±0.03	-0.03±0.04	0.6
12.50	15.5±0.8 mb	0.21±0.02	-0.52±0.03	-0.06±0.04	0.08±0.04	1.0
13.00	17.2±0.8 mb	0.18±0.01	-0.52±0.02	-0.10±0.03	-0.17±0.03	2.1
13.50	19.8±0.8 mb	0.24±0.02	-0.53±0.03	-0.05±0.04	0.04±0.04	2.3
14.00	19.3±1.2 mb	0.22±0.01	-0.48±0.02	0.10±0.03	0.03±0.04	4.0
14.50	17.9±1.2 mb	0.23±0.01	-0.52±0.03	-0.07±0.03	-0.11±0.04	4.1
15.00	18.4±1.1 mb	0.29±0.02	-0.37±0.03	-0.03±0.04	0.00±0.04	4.4
15.50	15.8±1.1 mb	0.29±0.02	-0.40±0.03	0.00±0.04	-0.14±0.05	0.4

Table 2-B. The b Coefficients Obtained with the $^{13}C(p,\gamma_1)^{14}N$ Reaction

E_p	b_1	b_2	b_3	b_4	X^2
8.05	-0.06±0.02	0.18±0.01	0.02±0.01	-0.01±0.01	0.7
9.00	-0.04±0.02	0.22±0.01	0.02±0.01	0.02±0.01	2.6
10.00	-0.07±0.02	0.22±0.01	0.03±0.01	0.01±0.01	0.8
10.95	-0.04±0.02	0.25±0.01	0.05±0.01	0.02±0.01	0.1
12.00	-0.05±0.02	0.28±0.01	0.03±0.01	0.00±0.01	1.6
12.5[illegible]	-0.[illegible]2±0.02	0.20±0.02	0.02±0.02	-0.03±0.02	1.5
13.00	-0.02±0.02	0.21±0.01	0.02±0.01	0.01±0.01	0.8
13.50	0.04±0.03	0.21±0.02	0.04±0.02	0.02±0.02	0.9
14.00	-0.08±0.03	0.22±0.02	0.04±0.02	-0.07±0.02	0.6
14.50	-0.01±0.02	0.23±0.01	0.04±0.02	-0.01±0.02	1.2
15.00	0.02±0.03	0.25±0.02	0.02±0.02	0.00±0.02	1.5
15.50	-0.08±0.03	0.26±0.02	0.08±0.02	0.06±0.02	0.1

Figure 15. Plots of the a_k and b_k coefficients obtained from the $^{13}C(p,\gamma_0)^{14}N$ reaction. These coefficients were obtained from the fits through fourth order shown in figures 11 and 12. The error flags reflect the statistical error in the original data. The coefficients are listed in table 1.

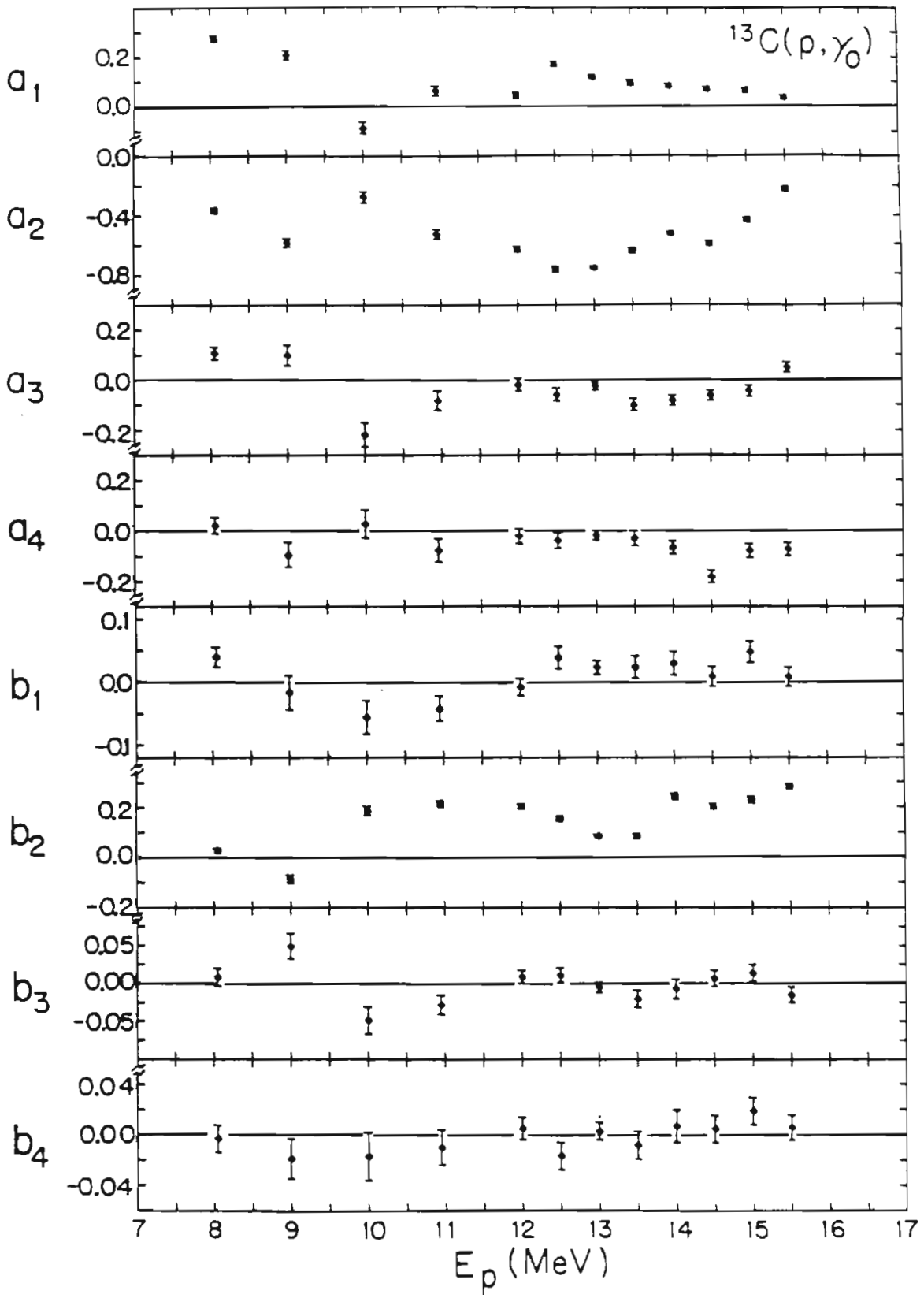
$^{13}C(p,\gamma_0)$
a_1
a_2
a_3
a_4
b_1
b_2
b_3
b_4
E_p (MeV)

Figure 16. Plots of the a_k and b_k coefficients obtained from the $^{13}C(p,\gamma_1)^{14}N$ reaction. These coefficients were obtained from the fits through fourth order shown in figures 13 and 14. The error flags reflect the statistical error in the original data. The coefficients are listed in table 2.

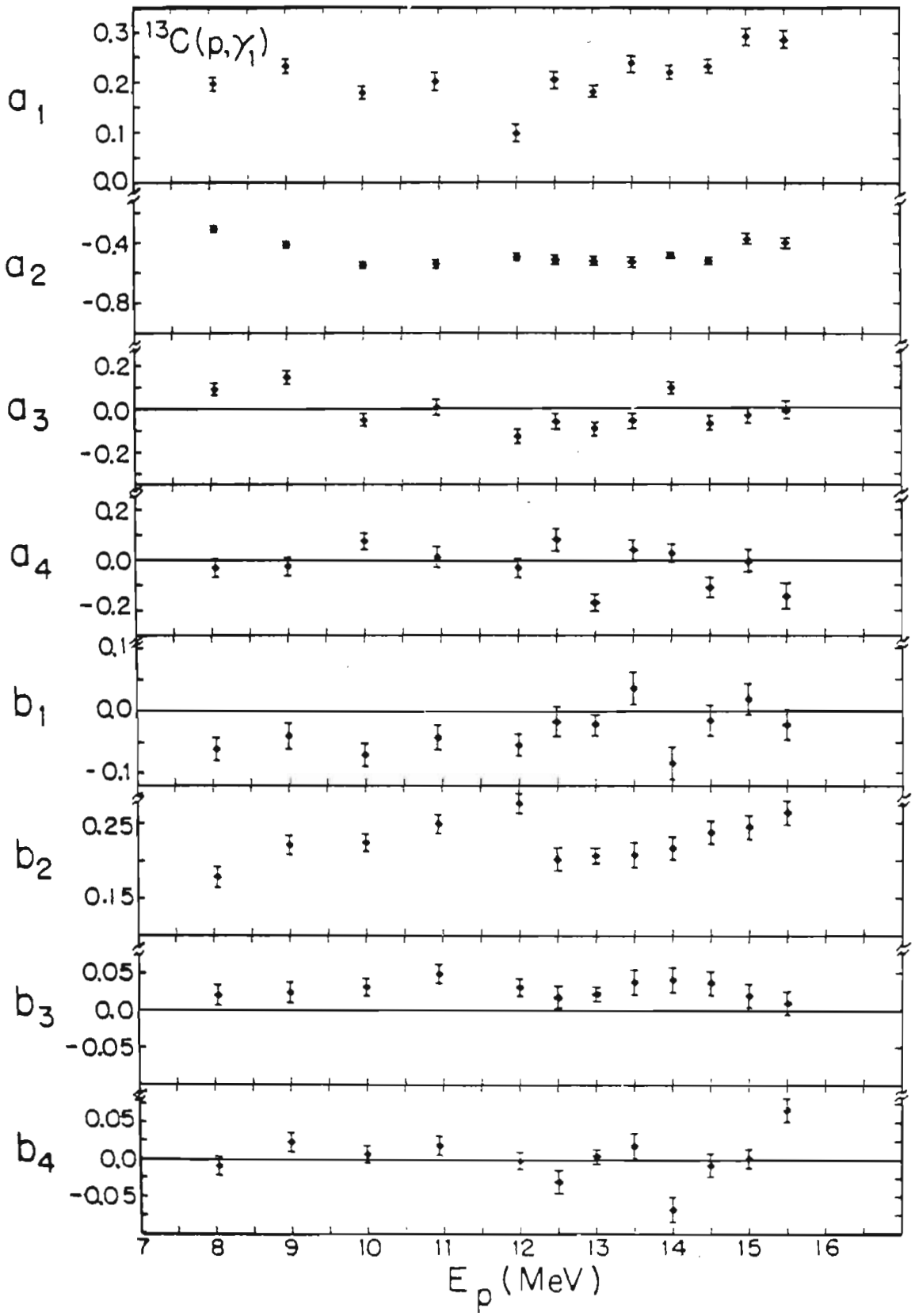
$^{13}C(p,\gamma_1)$
a_1
a_2
a_3
a_4
b_1
b_2
b_3
b_4
0.3
0.2
0.1
0.0
-0.4
-0.8
0.2
0.0
-0.2
0.2
0.0
-0.2
0.1
0.0
-0.1
0.25
0.15
0.05
0.0
-0.05
0.05
0.0
-0.05
7
8
9
10
11
12
13
14
15
16
E_p (MeV)

The angular distributions of analyzing power were fitted with a least squares procedure to an expansion in associated Legendre polynomials of the form

$$\sigma(\theta)A(\theta)/A_0 = \sum_{k=1} b_k Q_k P'_k(\cos\theta) ,$$

where the coefficients Q_k include corrections for the finite geometry. The fits through k=4 are shown as solid lines in figures 11 through 14. Due to the unphysical nature of the fourth order fit at E_p=14.0, a fit through third order is also shown in figure 14 as a dashed line. Tables 1 and 2 list the values of b_k obtained with fits through P'_4 to the ground state and first excited state transitions, respectively. The errors reflect the statistical error in the data and possible errors in the beam polarization. The table also lists the normalized chi-squares. The coefficients obtained from the fits through third order fall within the errors of the coefficients of the fourth order fits. The b_k coefficients derived from the fits through P'_4 for the ground state and first excited state transitions are plotted in figures 15 and 16, respectively.

In general the fits through fourth order were statistically justified for both the angular distribution and analyzing power data. This is consistent with the Landsdorf suggestion (1960) that angular distribution data should extend beyond the zero of P_{k+1} if the coefficient a_k is to be determined with statistical significance.

Statistically significant measurement of the coefficient b_4 can be obtained with data at less extreme angles because there is no b_0 and because the zeroes of the P'_k polynomials occur at angles less extreme than the P_k polynomials.

Baglin, Bentz, and Carr (1974) have made angular distribution measurements of the $^{14}N(\gamma,p_0)^{13}C$ reaction. These measurements were made with a bremsstrahlung beam and a gas target. The outgoing protons were detected at seven angles ranging from 20 to 160 degrees. Figure 17 shows a comparison of typical values of the a_k coefficients obtained from the values given in the (γ,p) experiment to the values obtained from this experiment. The agreement is, in general, excellent. Riess, O'Connell, and Paul (1971) have also measured the coefficients a_1 and a_2 at several energies using the $^{13}C(p,\gamma_0)$ reaction. Their results, plotted in figure 17 as crosses, are also in good agreement with the present data.

Figure 17. Comparison of the a_k coefficients obtained from the angular distributions of the $^{13}C(p,\gamma_0)^{14}N$ and $^{14}N(\gamma,p_0)^{13}C$ reactions. The coefficients obtained from this experiment are plotted as triangles. When no error flag is shown, the error is equal to the size of the triangle. The (p,γ_0) data taken by Reiss, O'Connell, and Paul (1974) are plotted as crosses while the (γ,p_0) data taken by Baglin, Bentz and Carr (1974) are plotted as points.

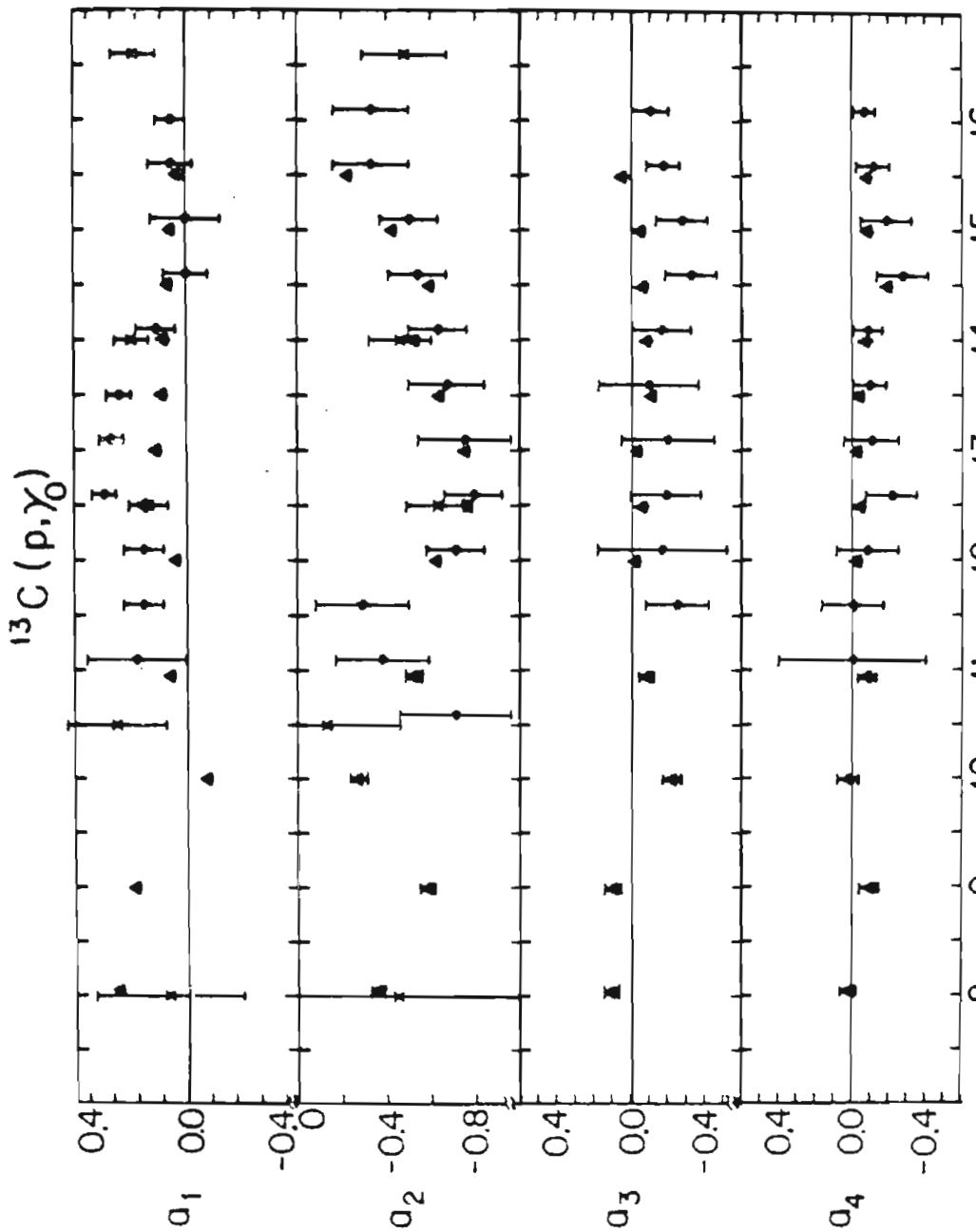
$^{13}C(p,\gamma_0)$
a_1
a_2
a_3
a_4
0.4
0.0
-0.4
0
-0.4
-0.8
0.4
0.0
-0.4
0.4
0.0
-0.4
8
9
10
11
12
13
14
15
16
E_p (MeV)

5.2 PROCEDURE FOR TRANSITION MATRIX ANALYSIS

The angular distributions of cross section and of analyzing power can be expressed as sums of products of transition matrix elements. Consider the following schematic representation of radiative capture in the jj coupling scheme.

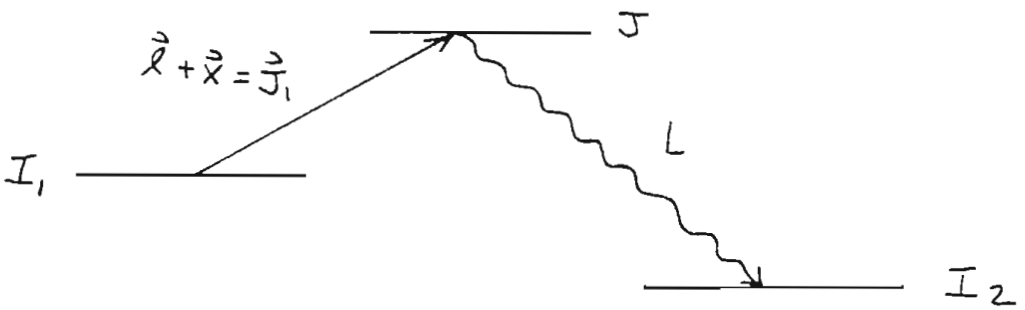

An incident particle of spin x and orbital momentum l is captured by a nucleus of spin I_1. The angular momenta of the incident channel, l and x, are coupled to form J_1. Then J_1 is coupled with I_1 to form an intermediate excited state of total angular momentum J. This excited state can decay by emitting a gamma ray of multipolarity L to a final state of spin I_2. This final state can be the ground state or an excited state. It is possible to excite many intermediate states of total angular momentum J and hence the formulation must allow for the possibility of interference. The primed variables in the expression below allow for this interference. The angular distribution of cross section, expanded in terms of Legendre polynomials in the jj coupling scheme is given by (Glavish, 1974)

$$\sigma(\Theta) = \sum_{\alpha} (-1)^{p} f \frac{1}{\hat{x}^2} \frac{1}{\hat{I}_1^2} \hat{J}\hat{J}'\hat{L}\hat{L}' \langle k0|\ell\ell'00\rangle \hat{\ell}\hat{\ell}'$$
$$\times \langle k0|LL'1-1\rangle W(LJL'J', I_2 k) W(J_1 J J_1' J', I_1 k)$$
$$\times W(\ell J_1 \ell' J_1', xk) P_k(\cos\Theta) \mathrm{Re}(RR'^{*})$$

where $p = J_1' - J_1 + \ell + \ell' + I_1 - I_2 - x - 1$ and f is given by

$f = 1/2\left[1 + (-1)^{L+L'+k}\right]$ pure electric or magnetic

$f = 1/2\left[1 - (-1)^{L+L'+k}\right]$ mixed electric and magnetic

The transition matrix element enters as the reduced matrix element $R = \langle LJ \| T \| \ell J_1 J \rangle$. The summation α includes summation over $1, 1', L, L', J, J', J_1, J_1'$ and k. The notation $\hat{a}$ is defined as

$$\hat{a} = \sqrt{2a+1}$$

The products of analyzing power and cross section can be expanded in terms of the associated Legendre polynomials (Glavish, 1974) as follows.

$$\frac{A(\Theta)\sigma(\Theta)}{A_0} = \sum_{\alpha} (-1)^{\beta} f \frac{1}{\hat{x}^2} \hat{J}^2 (J')^2 \hat{L}\hat{L}'\hat{J}_1\hat{J}_1'\hat{\ell}\hat{\ell}'$$
$$\times \left[\frac{3(2k+1)}{k(k+1)}\right]^{1/2} \langle k1|k101\rangle \langle k0|\ell\ell'00\rangle$$
$$\times \langle k0|LL'1-1\rangle W(LJL'J', I_2 k) W(J_1 J J_1' J', I_1 k)$$
$$\times \begin{Bmatrix} \ell & x & J_1 \\ \ell' & x' & J_1' \\ 1 & c & k \end{Bmatrix} P_k'(\cos\Theta)\, \mathrm{Im}(RR'^{*})$$

where $q = \ell' + J_1' + I_1 - I_2 - 2x + 1$.

The transition matrix elements are, in general complex, but can be written in terms of a real amplitude and phase as follows;

$$\text{matrix element} = A(l, J_1, L) \exp(i \phi(l, J_1, L))$$

where A is the amplitude and ϕ is the phase. Since the phase can be factored out, the above equations can be written in terms of amplitudes and relative phases.

The measurements of the a_k and b_k coefficients through k=4 provide up to 9 constraints (equations) on the transition matrix element amplitudes and their relative phases. In the interest of proper error analysis, a procedure has been developed (Cameron, 1977) to determine these amplitudes and relative phases directly from the experimental data by the minimization of chi-squared, calculated as follows;

$$\chi^2 = \sum_{data} \left(\frac{1}{\Delta\sigma_i}\right) \left[\sigma_i - \sum_k a_{k\,calc} Q_k P_k(\cos\theta)\right]^2$$

$$+ \sum_{data} \left(\frac{1}{\Delta\sigma_i A_i}\right) \left[\sigma_i A(\theta_i) - \sum_k b_{k\,calc} Q_k P_k'(\cos\theta)\right]^2$$

where $\sigma_i = \sigma_{exp}(\theta_i)/A_0$

and the summation over the data implies a sum over all data points (taken at an angle of θ_i). The quantities a_{calc} and b_{calc} are calculated from the equations given above. The minimum of chi-squared is obtained with a gradient search routine (Rosenbrock, 1960), and the errors are derived from the error matrix.

5.3 CALCULATION OF TRANSITION MATRIX ELEMENTS

The expressions relating angular distributions of cross section and analyzing power to the amplitudes and relative phases are inherently quadratic in nature and solving these equations generally results in double solutions. It is virtually impossible to choose the physical solution from the examination of experimental data and hence guidance from model calculations is useful. One model that has been particularly successful in describing the radiative capture process is the direct-semi-direct model. Work on this model began when compound nuclear model calculations failed to predict significant features in (p,γ) reactions in the giant dipole resonance region (Cohen, 1955). Cohen found that simple calculations assuming direct, single particle transitions to bound states could satisfactorily account for his measurements. A.M. Lane (1959) noted that the use of the "complex potential model" (Feshbach, Porter, and Weisskopf, 1954) implied that the incident particle moves some appreciable distance through a target nucleus before a

compound nucleus is formed. During this initial period of free motion, the incident particle could decay to a bound state by emitting a photon. The name "direct" was given to this one step process to distinguish it from the "two stage" compound nuclear process. Early calculations made by Lane (1959) with a square well potential showed fair agreement with experimental cross sections. More sophisticated calculations with a Woods-Saxon well produced cross sections significantly smaller than experimental values. G.E. Brown (1964) suggested that "semi-direct" capture in which the incident nucleon first inelastically excites the target nucleus into a collective state which subsequently radiatively decays could account for some of these differences.

The radial matrix element for direct-semidirect E1 capture is given by;

$$\left\langle \phi_{NLJ} \middle| r + \frac{V_1(r)}{E_\gamma - E_d + i\Gamma/2} \middle| \phi_{\ell' J'} \right\rangle$$

where V (r) is the radial part of the form factor. The kets $|\phi_{\ell' J'}\rangle$ are the protcn continuum wave functions calculated with the optical model and parameters derived from experimental data. The kets $|\phi_{NLJ}\rangle$ are bound state wave functions determined by integrating the Schroedinger equation with Woods-Saxon and spin-orbit potentials. In the

case of ^{14}N, the bound state is taken as a p1/2 particle for both the ground state and first excited state. The model can be simply extended to include a term to represent direct E2 capture.

If the form factor is taken to be that suggested by Brown (1964) the predicted relative amplitudes and phases will be identical to a pure direct calculation ($V_1(r)=0$), if the resonance parameters are taken to be the same for all matrix elements. Other form factors have been used in various calculations (Clement, Lane, and Rook, 1965; Snover et al., 1976; Likar, Potokar, and Cvelbar, 1977). In fact, Likar et al. (1977) have concluded that all approaches using real form factors give approximately the same energy dependence for the a_2 coefficient for $l \leq 3$ and medium weight nuclei. Consequently, for pure E1 radiation it is only necessary to perform a direct calculation, although the calculation can be considered either direct or direct-semidirect with a Brown form factor. Such a pure direct calculation should be sufficient to allow a clear choice of the physical E1 solution.

The analysis of the first excited state (see below) includes extraction of the E2 cross section. Comparison of this measured cross section to a direct E2 calculation will also be discussed below.

5.4 TRANSITION MATRIX ANALYSIS OF THE GDR BUILT ON THE GROUND STATE

The coupling of the 1/2- ground state of ^{13}C to the 1+ ground state of ^{14}N through radiative proton capture allows a total of 5 E1 amplitudes, 6 E2 amplitudes, and 5 M1 amplitudes. In an analysis limited to E1, E2, and M1 radiation, finite values of a_1 and b_1 can arise from the interference of E1 amplitudes with either E2 or M1 amplitudes, while finite values of a_3 and b_3 arise from E1-E2 interference. The coefficients a_2 and b_2 arise from either E1, M1 or E2 strength, while a_4 and b_4 depend only on E2 strength and E2 interference. Although the presence of finite values of coefficients other than a_2 and b_2 indicate the presence of radiation other than E1, the majority of the strength in the energy range of this study is expected to be E1 and hence a pure E1 analysis of the data should be useful. An examination of figure 15 supports this assumption in that the plots of a_2 and b_2 show the greatest magnitude. The equations for a_0, a_2, and b_2 represent 3 constraints on the 5 E1 amplitudes and 4 relative phases. The contributing E1 amplitudes are

$$ {}_0s1/2 \qquad {}_1s1/2 \qquad {}_1d3/2 \qquad {}_2d3/2 \qquad {}_2d5/2 $$

The notation is ${}_3L_{J_1}$, where J_1 is the value of the total angular momentum in the incident channel and J is the total angular momentum of the intermediate state. If definite solutions are to be found, a reduction in the number of

variables is required. In the absence of spin orbit forces, the matrix elements of a given orbital angular momentum value (l) and various allowed values of total incident angular momentum (J_I) and intermediate angular momentum (J) should be identical. Direct calculations with the spin orbit potential set to zero show no difference in the d3/2 and d5/2 matrix elements and verifies the sensitivity of the calculation to the spin-orbit potential. The direct coupling of d5/2 protons to a p1/2 bound state through E1 radiation, moreover, is not allowed. A pure E1 analysis was made using the following assumptions. The ${}_0$s1/2 and ${}_1$s1/2 amplitudes were assumed to be equal, the ${}_1$d3/2 and ${}_2$d3/2 amplitudes were assumed to be equal, and the ${}_2$d5/2 contribution was assumed to be zero. With these assumptions, the equations for pure E1 radiation become

$$a_0 = 1.0 = 1.000\,(s)^2 + 2.000\,(d)^2 \quad ,$$

$$a_2 = -1.9516\,(sd)\cos(\phi_s - \phi_d) - 0.900\,(d)^2 \quad ,$$

$$b = 1.179\,(sd)\sin(\phi_s - \phi_d) \quad ,$$

where ϕ_s and ϕ_d are the phases of the combined s and d amplitudes, respectively. Since these E1 equations represent three equations in three unknowns and direct quadratic algebraic solutions are possible, the experimental values of a_2 and b_2 were fitted with the amplitudes and relative phase. Complex solutions with degenerate real roots are indicated by non-zero values of chi-squared obtained with real variables. Table 3 lists the solutions

obtained from the values of a2 and b2 derived from the fits through fourth order. The amplitudes are given as a percent of the cross section (where $\sigma_s = 1.0 s^2$ and $\sigma_d = 2.0 d^2$). The errors indicated are derived from the error matrix and reflect the statistical error in the original data. Figure 18 shows a plot of these E1 solutions as a function of energy. The d amplitude is plotted as a percent of the cross section, with the remaining strength being s. A line drawing of the excitation curve is provided for reference at the top of the figure. A direct calculation (Cotanch, 1978) for the $^{13}C(p,\gamma_0)^{14}N$ reaction was performed using the parameters listed in table 4. The results of this calculation are shown in figure 18 as solid lines. The agreement with the amplitudes extracted from the data is very good throughout the region studied, however the calculated phase disagrees substantially in shape and value from the phase extracted from the data. This difference is not surprising considering the assumptions made to reduce the number of E1 amplitudes. The importance of the $_2d5/2$ amplitude was tested by repeating the analysis with the assumption that all three d matrix elements were equal. This analysis produced similar values for the amplitudes and relative phase for each of the two solutions. This supports our original simplifying assumption that $_2d5/2=0$. One notable difference for this latter calculation was that three energies produced solutions with non-zero values of

Table 3. The E1 solutions Obtained from the $^{13}C(p,\gamma_0)^{14}N$ Reaction

E_p (Mev)	solution 1 σ_d (%)	solution 1 σ_s (%)	solution 1 $(\phi_d-\phi_s)$ (deg)	solution 2 σ_d (%)	solution 2 σ_s (%)	solution 2 $(\phi_d-\phi_s)$ (deg)
8.05	99.5±0.9	0.5±0.2	-153±12	6.3±0.7	93.6±1.2	-7±3
9.00	97.8±1.8	2.2±0.7	45±9	17.5±2.0	82.5±2.7	16±3
10.00	93.4±2.0	6.5±1.3	-115±6	8.6±1.5	91.3±2.3	-53±3
10.95	92.1±1.9	7.9±1.1	-73±5	20.6±2.1	79.3±2.6	-39±3
12.00	90.6±1.5	9.4±1.0	-57±3	26.5±1.7	73.4±2.0	-34±2
12.50	88.2±2.1	11.8±1.6	-35±3	34.7±2.4	65.3±2.8	-23±2
13.00	92.6±1.0	7.4±0.7	-23±2	29.8±1.2	70.2±1.5	-13±1
13.50	96.7±1.2	3.3±0.6	-35±4	20.8±1.4	79.1±1.8	-14±2
14.00	89.6±1.5	10.3±1.3	-73±2	23.0±1.5	76.9±1.8	-44±2
14.50	91.7±1.3	8.3±0.9	-62±3	23.9±1.4	76.0±1.8	-35±2
15.00	91.8±1.3	8.2±1.0	-88±3	16.9±1.3	83.1±1.6	-47±2
15.50	85.0±1.5	15.0±1.2	-109±2	15.0±1.2	85.0±1.5	-71±2

Table 4. Parameters for the Direct Model Calculations (optical model parameters taken from Richter and Parish, 1968)

Continuum Single Particle State	Bound State
Real Well:	Ground State:
V =48.0 MeV	V =53.07 MeV
r =1.27 fm	E =-7.551 MeV
a =0.62 fm	
	First Excited State:
Imaginary Volume	V =48.59 MeV
V =0.0 MeV	E =-5.238 MeV
Imaginary Surface:	
V =8.5 Mev	
r =1.27 fm	
a =0.48 fm	
Spin Orbit:	
V =5.50 MeV	
r =1.175 fm	
a =0.62 fm	
Coulomb Radius:	
R =1.27 fm	

Figure 18. The solutions obtained from an E1 analysis of the $^{13}C(p,\gamma_0)^{14}N$ reaction using the procedure described in the text. The d amplitude is plotted as a percent of the cross section, with the remaining strength being s. The solid lines represent the results of a calculation using the direct model. The solutions are listed in table 3.

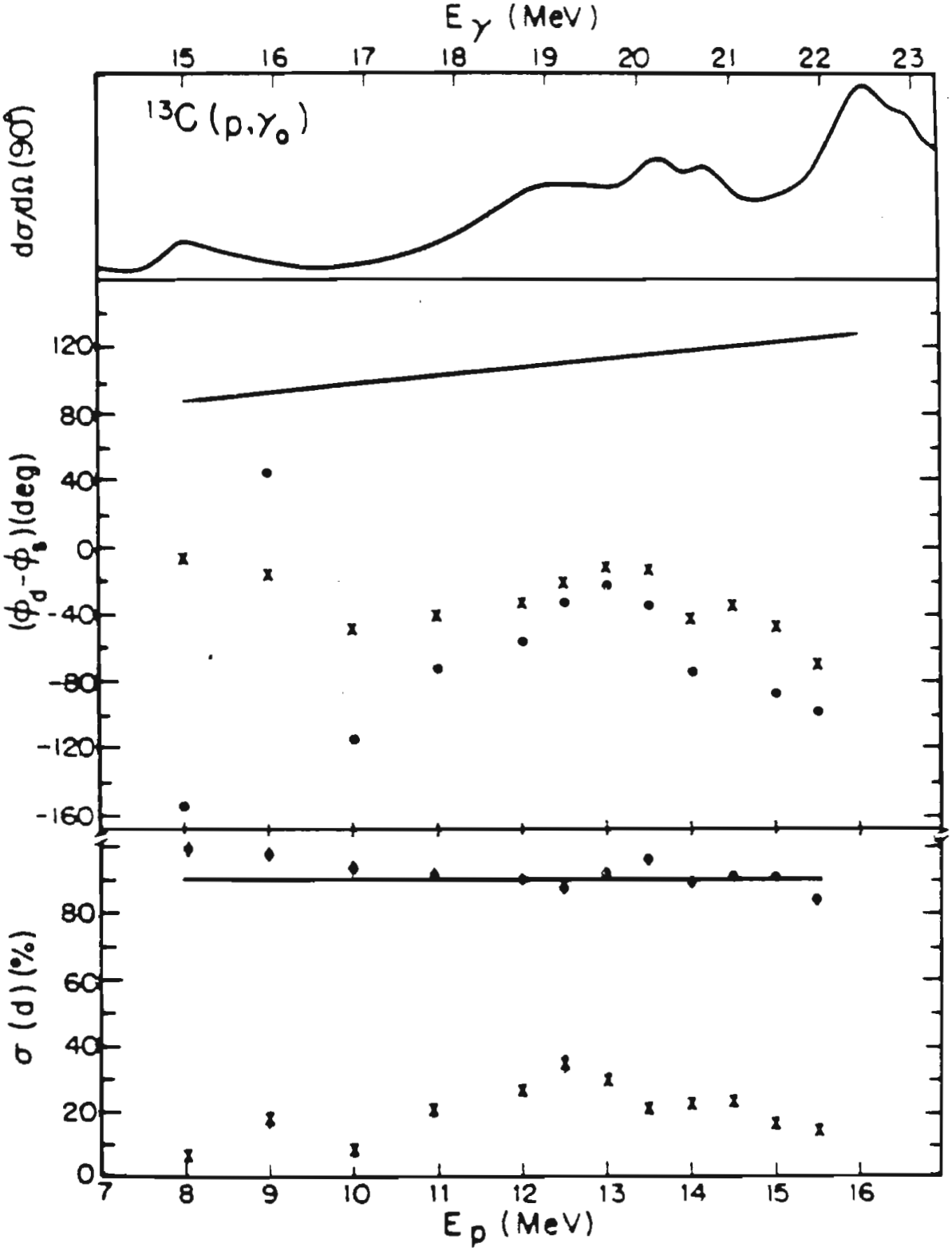
E γ (MeV)
15
16
17
18
19
20
21
22
23
13C (p,γ0)
dσ/dΩ (90°)
120
80
40
0
-40
-80
-120
-160
(φd-φp) (deg)
80
60
40
20
0
σ (d) (%)
7
8
9
10
11
12
13
14
15
16
Ep (MeV)

chi-squared (complex solutions with degenerate real components).

The phase extracted from the data can also be considered in the light of an optical model and phase shift analysis performed on elastic scattering data by Weller et al. (1978). If, as the analysis above indicates, the s amplitudes are small, and the d5/2 amplitude can be neglected because it does not contribute to direct capture, the typical a_2 value of -0.5 can only be explained by a giant resonance which has a maximum of 18 percent 1- contribution and a minimum of 82 percent 2-. Similar arguments led to the assignment of 2- for the giant resonance by Reiss, O'Connell, and Paul (1974). The 2- d3/2 amplitude, which must predominate under these assumptions, is composed of components having channel spin 0 and channel spin 1. The phase of the channel spin zero component of the d amplitude can be compared to the channel spin zero or channel spin one components of the s amplitude. The $(\delta^2_{a0} - \delta^1_{01})$ and $(\delta^2_{a0} - \delta^1_{00})$ phase differences (where the notation is δ^J_{LS}) determined by the phase shift analysis of the elastic scattering data by Weller et al. (1978) are approximately negative 50 and negative 70 degrees, respectively. These are in fair agreement with the phase extracted from the data in the above analysis. Thus the present data are consistent with an assignment of 2- to the giant dipole resonance and the predominance of d strength having channel spin zero.

The multiplicity of E2 and M1 amplitudes renders the extraction of definite solutions in an analysis including either of these multipoles impossible. For this reason, no further analysis of the (p,γ_0) data was attempted.

5.5 TRANSITION MATRIX ANALYSIS OF THE GDR BUILT ON THE FIRST EXCITED STATE

The coupling of the 1/2- ground state of ^{13}C to the 0+ first excited state of ^{14}N through radiative proton capture allows a total of 2 E1, 2 E2, and 2 M1 amplitudes. However, following the discussion in section 5.4, a pure E1 analysis is a logical beginning. If consideration is limited to E1 amplitudes, the equations of interest are

$$a_0 = 1.0 = 0.7500\,(s1/2)^2 + 0.7500\,(d3/2)^2$$

$$a_2 = 1.061\,(s1/2)\,(d3/2)\cos(\phi_s - \phi_d) - 0.3750\,(d3/2)^2$$

$$b_2 = -0.5303\,(s1/2)\,(d3/2)\sin(\phi_s - \phi_d)$$

where the notation is L_{J_i} with L and J_i being the orbital and total angular momentum of the incident proton, respectively. The phases ϕ_s and ϕ_d represent the phases associated with the s and d amplitudes. These three equations were solved for each energy using the values of a_2 and b_2 obtained from the fits through fourth order, which are listed in table 2. Table 5 lists the solutions and errors derived from the error matrix (where $\sigma s = .75s^2$ and $\sigma d = .75d^2$). Figure 19 shows a plot of the solutions as a function of energy. As before in figure 18, the d amplitude is plotted as a percent of the cross section with the remaining strength being s. A line drawing of the excitation curve is

Table 5. The E1 Solutions Obtained from the $^{13}C(p,\gamma_1)^{14}N$ Reaction

	solution 1			solution 2		
E_p(Mev)	$\sigma_{d3/2}$(%)	$\sigma_{s1/2}$(%)	$(\phi_d-\phi_s)$ (deg)	$\sigma_{d3/2}$(%)	$\sigma_{s1/2}$(%)	$(\phi_d-\phi_s)$ (deg)
8.05	91.9±1.6	8.1±1.6	67±4	10.7±1.3	89.3±1.7	126±3
9.00	88.9±1.9	11.0±1.5	86±4	18.2±1.8	81.8±2.3	126±3
10.00	87.9±2.0	12.1±1.6	104±3	25.5±2.1	74.5±2.5	133±2
10.95	84.5±2.7	15.5±2.1	104±4	28.5±2.9	71.4±3.4	129±3
12.00	80.5±3.0	19.4±2.6	99±3	30.2±3.1	69.8±3.5	122±3
12.50	90.7±2.1	9.3±1.5	99±4	21.0±2.2	79.0±2.7	135±3
13.00	90.1±1.6	9.9±1.2	100±3	21.9±1.6	78.0±2.0	135±2
13.50	90.3±2.4	9.7±1.9	100±4	21.9±2.4	78.1±2.9	135±3
14.00	89.4±2.1	10.6±1.7	95±3	20.9±2.0	79.0±2.4	131±3
14.50	88.0±2.2	12.0±1.8	100±4	24.0±2.3	76.0±2.7	132±3
15.00	85.0±2.6	15.0±2.2	84±4	20.4±2.5	79.5±2.9	118±3
15.50	84.1±3.0	15.9±2.4	88±4	22.5±2.8	77.5±3.3	119±3

Figure 19. The solutions obtained from a pure E1 analysis of the $^{13}C(p,\gamma_1)^{14}N$ reaction. The d amplitude is plotted as a percent of the cross section with the remaining strength being s. The solutions are listed in table 5. The solid lines indicate the results of the direct model calculation described in the text.

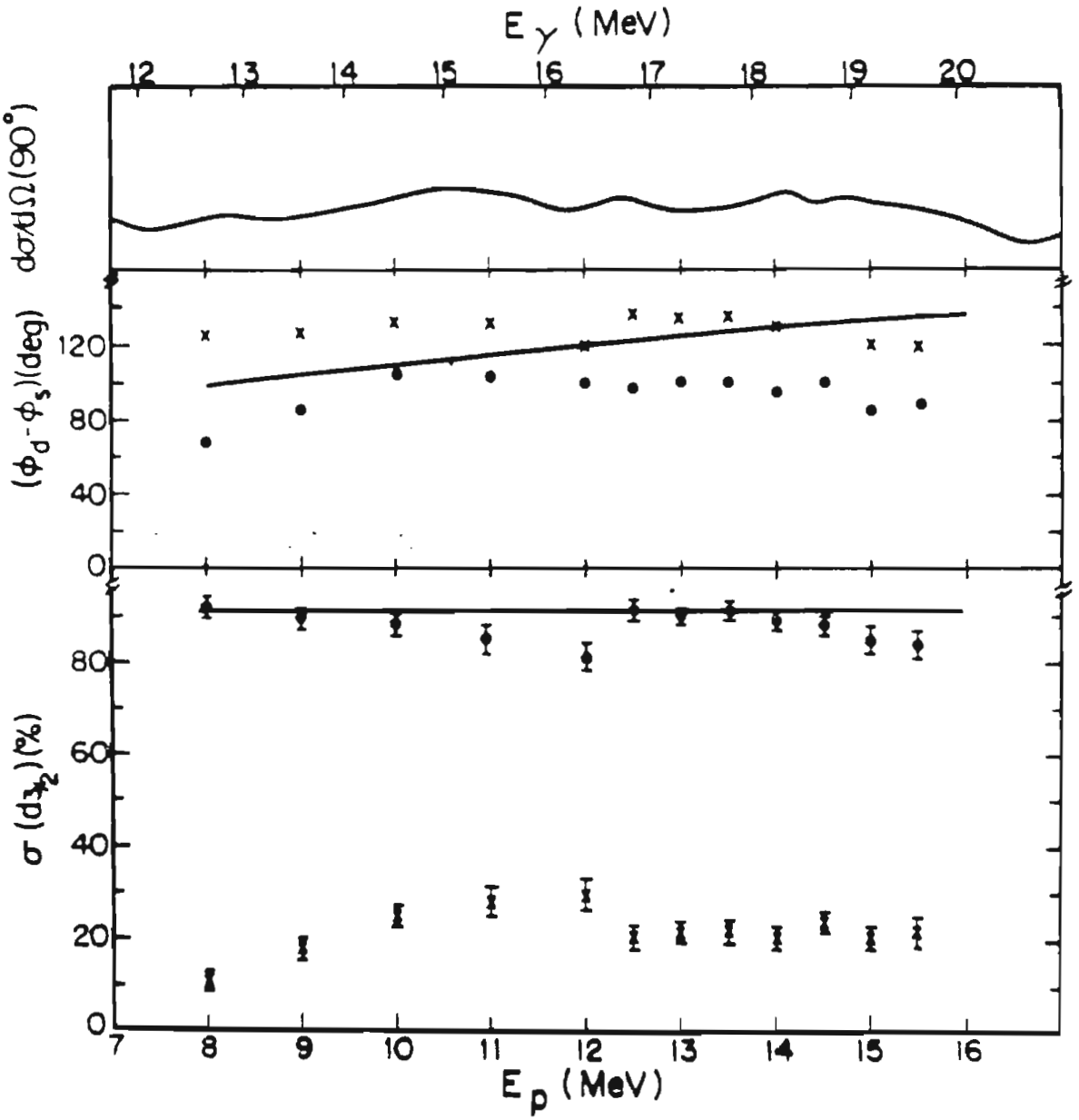
E γ (MeV)
12
13
14
15
16
17
18
19
20
dσ/dΩ(90°)
(φd - φs)(deg)
120
80
40
0
σ (d3/2)(%)
80
60
40
20
0
7
8
9
10
11
12
13
14
15
16
E p (MeV)

provided at the top of the figure for reference. A direct calculation (Cotanch, 1978) for the $^{13}C(p,\gamma_1)^{14}N$ reaction was performed using the parameters listed in table 4. The results of this calculation are shown in figure 19 as solid lines. The calculation clearly indicates that the predominantly d solution is the preferred solution. The agreement of the calculation with the amplitudes extracted from the data is very good. Although the phases disagree somewhat in shape, the values are similar and both increase in value with energy.

After this pure E1 analysis it is reasonable to consider the possibility of E2 or M1 radiation. Including both E2 and M1 amplitudes would prohibit distinct solutions and hence neglect of one of these multipoles is necessary. The finite values of a_3 and b_3 are consistent with the presence of E2 radiation and cannot arise from E1-M1 interference. The giant M1 resonance in this nucleus lies below the region spanned by this study and is expected to exhaust most of the M1 sum rule (Hanna, 1974). Fugii and Sugimoto (1959) have also shown from consideration of the radial matrix elements that the M1 strength is very small. For these reasons, the M1 amplitudes were neglected. If consideration is limited to E1 and E2 radiation, the contributing amplitudes are

s1/2(E1) d3/2(E1) p3/2(E2) f5/2(E2)

using the notation described above. The expressions for the a_k and b_k coefficients become

$$1 = a_0 = 0.750(s_{1/2})^2 + 0.750(d_{3/2})^2 + 1.250(p_{3/2})^2 + 1.250(f_{5/2})^2$$

$$a_1 = 2.372(s_{1/2})(p_{3/2})\cos(\phi_s - \phi_p) - 0.335(d_{3/2})(p_{3/2})\cos(\phi_d - \phi_p) + 2.465(d_{3/2})(f_{5/2})\cos(\phi_d - \phi_f)$$

$$a_2 = 1.061(s_{1/2})(d_{3/2})\cos(\phi_s - \phi_d) - 0.375(d_{3/2})^2 + 0.625(p_{3/2})^2 - 0.437(p_{3/2})(f_{5/2})\cos(\phi_p - \phi_f) + 0.714(f_{5/2})^2$$

$$a_3 = 1.936(s_{1/2})(f_{5/2})\cos(\phi_s - \phi_f) + 2.012(d_{3/2})(p_{3/2})\cos(\phi_d - \phi_p) - 1.095\cos(\phi_d - \phi_f)$$

$$a_4 = 3.499(p_{3/2})(f_{5/2})\cos(\phi_p - \phi_f) - 0.714(f_{5/2})^2$$

$$b_1 = 1.186(s_{1/2})(p_{3/2})\sin(\phi_s - \phi_p) - 0.671(d_{3/2})(p_{3/2})\sin(\phi_d - \phi_p) - 1.232(d_{3/2})(f_{5/2})\sin(\phi_d - \phi_f)$$

$$b_2 = -0.530(s_{1/2})(d_{3/2})\sin(\phi_s - \phi_d) + 0.365(p_{3/2})(f_{5/2})\sin(\phi_p - \phi_f)$$

$$b_3 = -0.646(s_{1/2})(f_{5/2})\sin(\phi_s - \phi_f) + 0.671(d_{3/2})(p_{3/2})\sin(\phi_d - \phi_p) + 0.0913(d_{3/2})(f_{5/2})\sin(\phi_d - \phi_f)$$

$$b_4 = 0.875(p_{3/2})(f_{5/2})$$

These four amplitudes and three relative phases were fitted directly to the experimental data through the minimization of chi-squared as described in section 2. As expected, solutions were found at each energy with E1 amplitudes

similar to the two pure E1 solutions described above (one predominantly d and the other predominantly s). For some energies two minima with different values of E2 strength were located for each of the two E1 solutions. As discussed above, the direct calculation indicated that the predominantly d solution is the physical solution. Hence consideration in the rest of this analysis will concentrate only on these solutions that are predominantly d3/2.

A search was conducted to determine if double solutions exist for the f5/2 and p3/2 amplitudes at all energies. The f5/2 (E2) amplitude was held fixed and the remaining six parameters were varied for a minimum of chi-squared. The cross section resulting from the f5/2 amplitude ($\sigma_f = 1.25\,(f5/2)^2$) was then varied from 0 to 20 percent of the total cross section in 1 percent steps. Figure 20 shows a plot of chi-squared per degree of freedom as a function of total E2 strength for three representative energies. The E2 strength ($\sigma_f + \sigma_p$) is plotted as a percent of the total cross section. The location and relative depth of the two minima varies, with some energies showing the deepest minimum in the zero to four percent range (see 12.5 MeV in figure 20, for example) while other energies show the deepest minimum in the seven to twenty percent range (see 13.0 MeV in figure 20, for example). For some energies the minimum in the seven to twenty percent range vanishes entirely (see 9.0 MeV in figure 20, for example), leaving only the solution in the zero to four percent range.

Figure 20. Plots of chi-squared per degree of freedom as a function of E2 strength obtained from an E1-E2 analysis of data taken with the $^{13}C(p,\gamma_1)^{14}N$ reaction. Results are plotted from data taken at proton energies of 9.0, 12.5, and 13.0 MeV. The E2 strength is plotted as a percent of the cross section, with the remaining strength being E1.

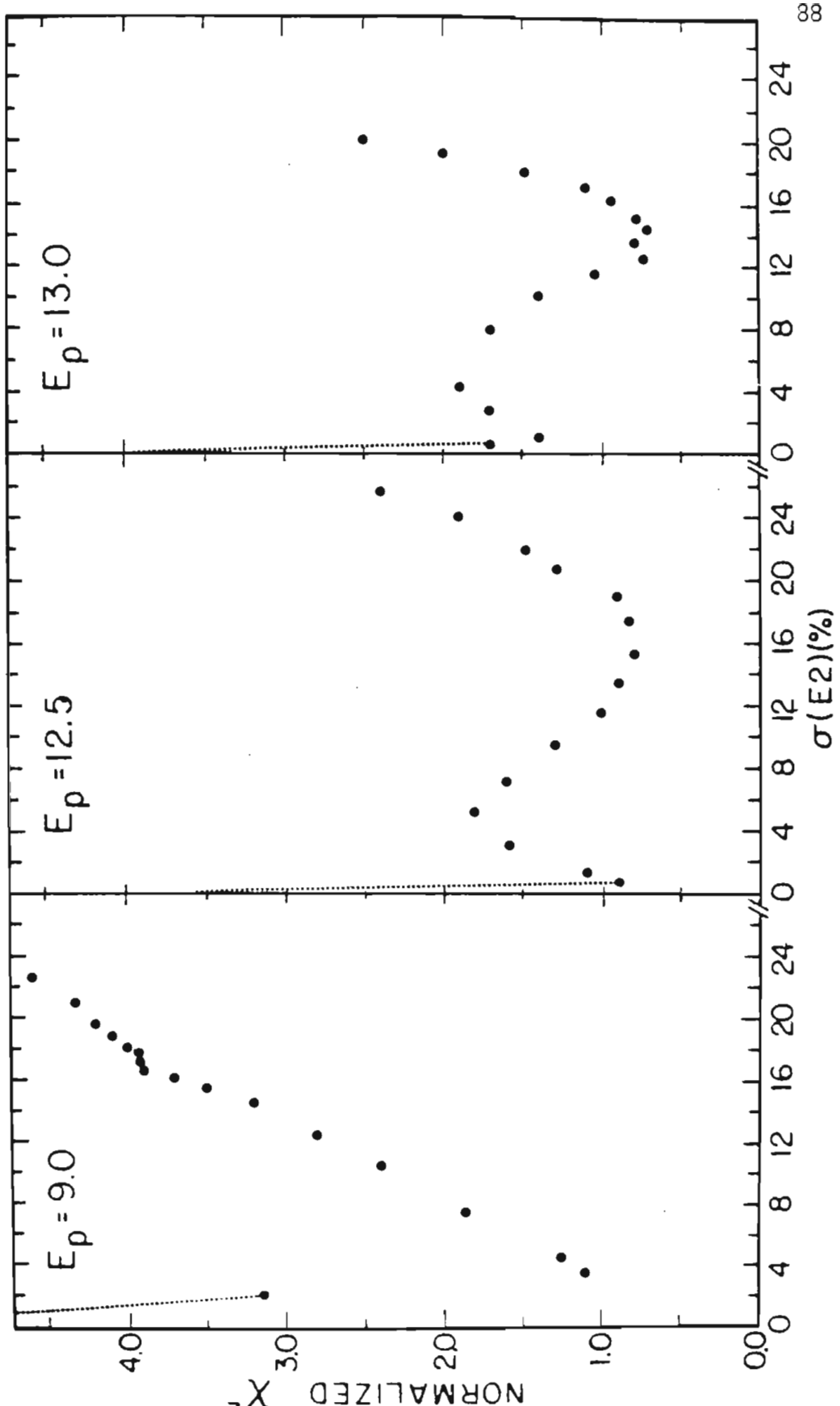
E_p=9.0
E_p=12.5
E_p=13.0
NORMALIZED χ^2
σ(E2)(%)
0.0
1.0
2.0
3.0
4.0
0
4
8
12
16
20
24

Table 6 lists the E2 solutions obtained with this method. The strengths in table 6 are listed as a percent of the cross section, where $\sigma_d = 0.75(d3/2)^2$, etc. It is interesting to note that the larger E2 solution has an E1 solution with substantially less d strength. Figure 21 shows a plot of the E1-E2 solutions listed in table 6. In order to compare the E1 results with the direct calculation (see figure 19) the d strength is shown as a percentage of the E1 cross section, rather than a percent of the total cross section. The solutions with less d strength and more E2 strength substantially disagree with this calculation. This disagreement, however, should not be taken too seriously because of the simplicity of the calculation. Nevertheless, it should be noted that if these points of greater E2 strength are considered as the physical solutions, this would imply several points of discontinuity in the E1 amplitudes.

The relative sizes and phase of the p and f E2 amplitudes have also been obtained with a pure direct calculation. Figure 22 shows a plot of the f amplitude and the f to p phase difference as a function of energy. The f amplitude is plotted as a percent of the E2 cross section, where $\sigma_f = 1.25(f5/2)^2$ and $\sigma_p = 1.25(p3/2)^2$. The smaller E2 solutions are plotted as points while the larger E2 solutions are plotted as crosses. The results of the calculation are shown as solid lines. The agreement between

Table 6. The E1-E2 Solutions Obtained from the $^{13}C(p,\gamma_1)^{14}N$ Reaction

E_p(MeV)	d3/2(%)	(ϕd-ϕs) (deg)	σs1/2(%)	σf5/2(%)	(ϕd-ϕf) (deg)	σp3/2(%)	(ϕp-ϕs)	X^2
8.05	90.4±1.6	69±4	8.3±1.2	0.7±0.2	55±13	0.7±0.2	59±16	0.5
9.00	85.6±2.2	89±3	10.6±1.6	1.6±0.3	85±11	2.1±0.6	98±9	1.1
10.00	86.3±2.1	107±3	13.0±1.8	0.7±0.3	69±12	0.0±0.1	-10±70	1.0
	54.4±2.3	128±3	30.2±2.3	8.8±1.3	118±6	6.5±1.1	128±3	1.1
10.95	83.1±2.9	105±4	15.6±2.4	0.8±0.4	108±20	0.5±0.4	78±27	1.3
	56.7±3.9	125±4	32.8±3.9	7.3±1.5	98±9	3.1±1.4	173±13	1.8
12.00	78.3±4.3	101±4	20.1±3.1	0.7±0.7	20±13	1.0±0.7	-67±19	0.7
12.50	89.2±2.2	101±5	10.1±1.7	0.7±0.2	104±19	0.1±0.1	48±66	0.9
	56.5±2.8	123±3	27.3±2.6	8.4±1.0	161±7	7.7±1.3	118±7	0.8

13.00	89.9±1.4	98±3	9.4±1.2	0.7±0.2	86±13	0.0±0.3	83±130	1.4
	53.9±3.1	131±3	31.7±2.9	9.9±1.1	72±7	4.5±0.5	240±10	0.7
13.50	88.2±2.6	103±4	10.0±2.0	1.4±0.4	131±15	0.3±0.3	85±32	1.1
14.00	85.1±3.2	99±3	12.2±2.4	0.9±0.3	111±23	1.8±0.7	70±13	14.3
	60.4±3.2	118±3	23.4±2.3	6.3±1.1	165±5	9.9±1.4	96±5	1.8
14.50	86.6±2.3	100±3	12.0±1.8	1.0±0.3	114±17	0.4±0.3	67±23	2.4
	51.4±4.1	127±3	37.9±4.8	7.3±1.3	59±10	3.4±0.9	268±16	1.8
15.00	81.8±3.3	87±4	15.3±2.5	2.3±0.6	100±13	0.6±0.5	105±21	1.9
15.50	83.3±2.8	88±4	14.4±2.3	1.9±0.5	71±12	0.4±0.3	87±29	2.2
	50.6±3.8	118±4	29.4±3.6	15.8±2.2	81±7	4.2±1.4	181±9	1.0

Figure 21. The predominantly $d_{3/2}$ solutions obtained from an E1-E2 analysis of the $^{13}C(p,\gamma_1)^{14}N$ reaction. In the lower half of the figure the d amplitude is plotted as a percent of the E1 cross section, with the remaining strength being s. The dashed line represents the results of a direct E1 calculation. The E2 strength is plotted as a percent of the total cross section in the upper portion of the figure. The solutions are listed in table 5-6.

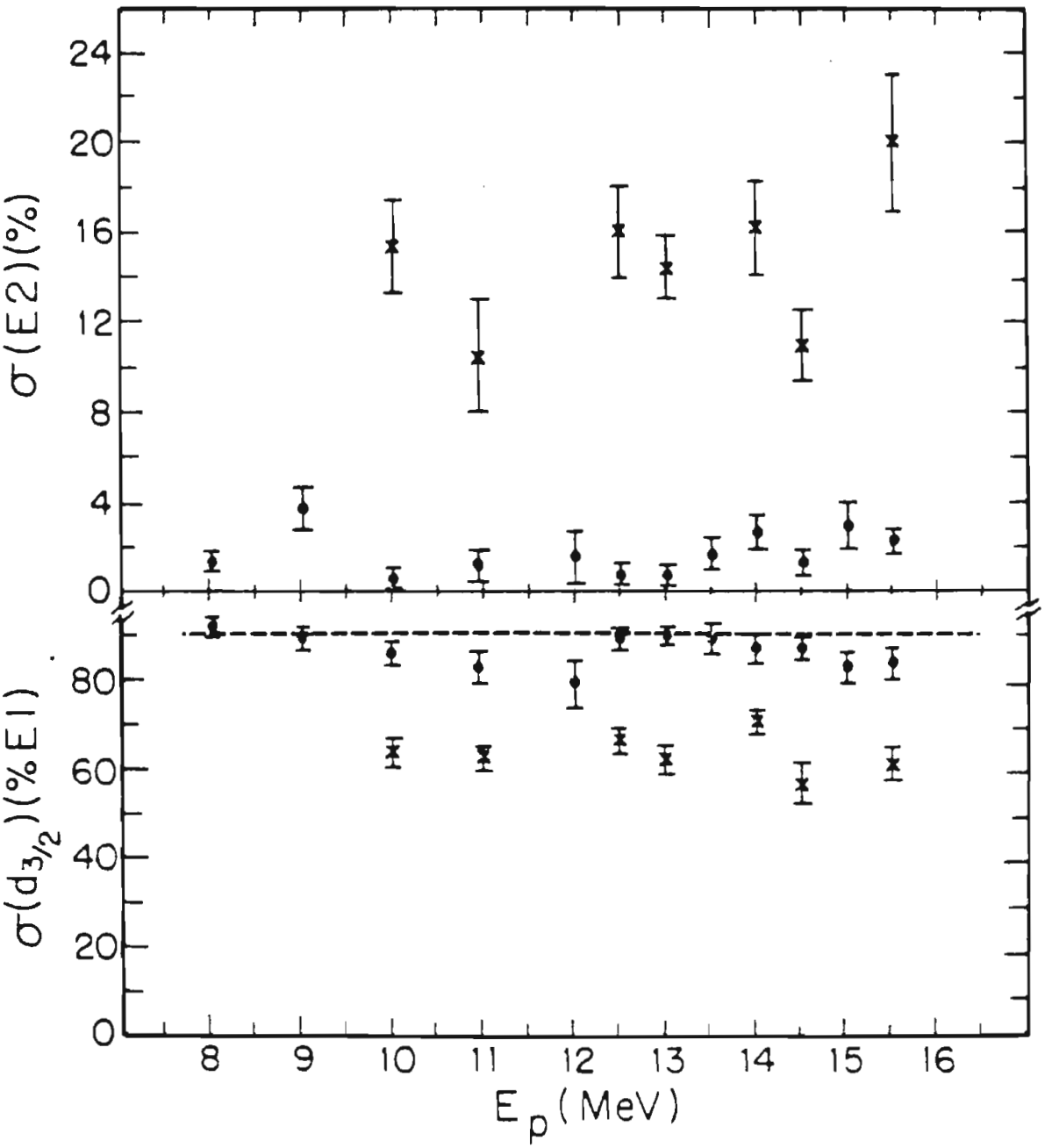
σ(E2)(%)
24
20
16
12
8
4
0
σ(d3/2)(%E1)
80
60
40
20
0
8
9
10
11
12
13
14
15
16
Ep (MeV)

Figure 22. Plots of the E2 amplitudes and relative phases extracted from data taken with the $^{13}C(p,\gamma_1)^{14}N$ reaction. The f amplitudes are plotted as a percent of the E2 cross section with the remaining E2 cross section being p strength. The solutions with smaller total E2 strength are plotted as points while the solutions with larger total E2 strength are plotted as crosses. The results of a direct E2 calculation are shown as solid lines.

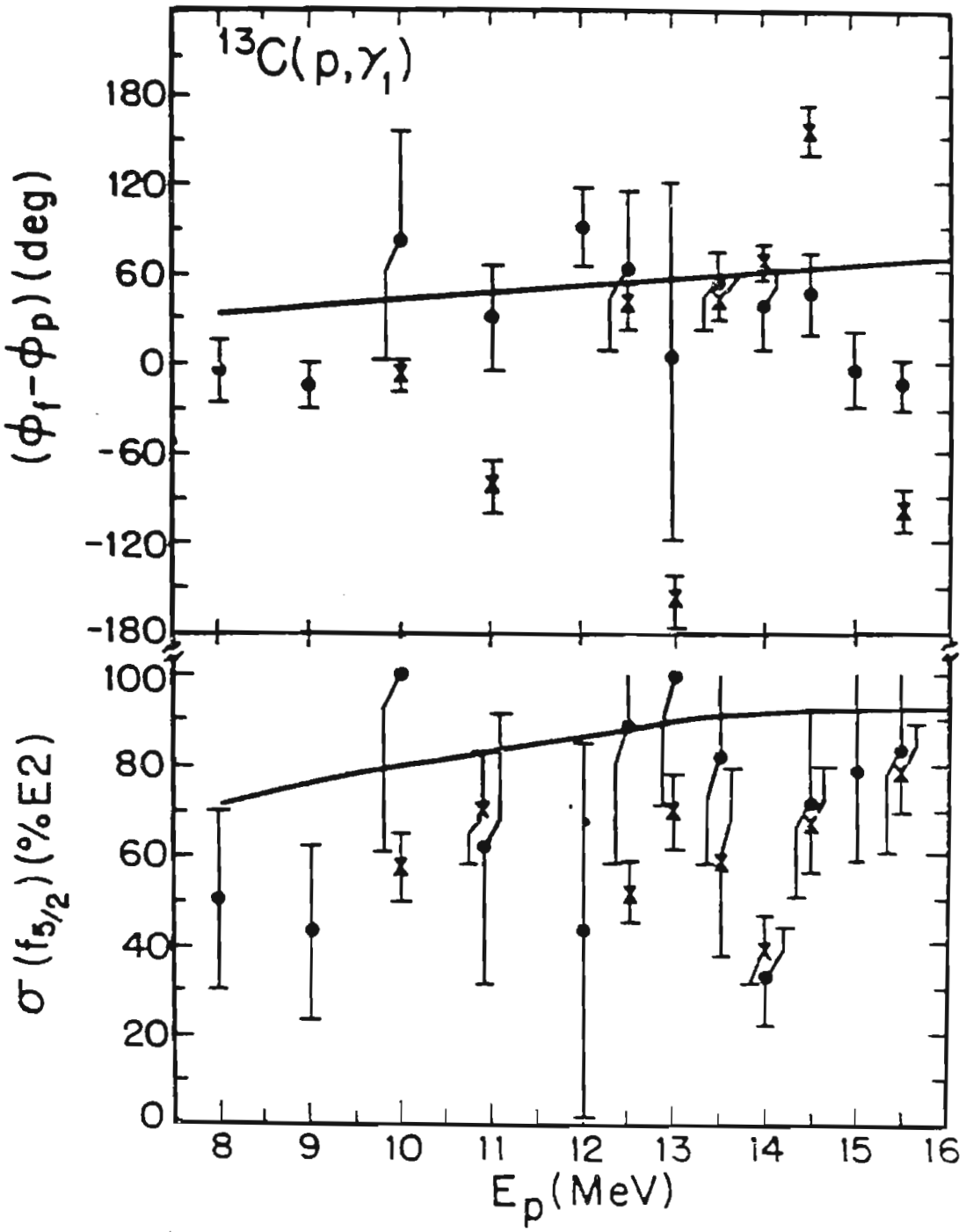
$^{13}C(p,\gamma_1)$
$(\phi_f-\phi_p)$ (deg)
180
120
60
0
-60
-120
-180
$\sigma(f_{5/2})$ (%E2)
100
80
60
40
20
0
8
9
10
11
12
13
14
15
16
E_p (MeV)

the calculation and the smaller E2 solution is fairly good. It is interesting to note that the larger E2 solution is in significantly less agreement than the smaller E2 solution. This result adds more strength to the argument that the smaller E2 solutions are the physical ones.

The direct model discussed above can also be used to calculate the direct E2 cross section. Figure 23 shows a plot of the E2 cross section and the results of a direct calculation made using the parameters listed in table 4. This calculation, shown as a solid line, includes a spectroscopic factor of 0.85 (Cohen and Kurath, 1967) and an effective charge of 0.89 for quadrupole radiation (Hayward, 1970). The set of solutions with the smaller E2 cross section is in fair agreement with the calculation. The set of solutions with the larger E2 could arise from an E2 resonance or resonances. Wagner et al. have observed the giant isoscalar quadrupole resonance (GQR) in ^{14}N via the $^{14}N(^{7}Li,^{7}Li')$ reaction. The solutions with larger E2 strength could certainly indicate the presence of this GQR. However, as will be discussed below in section 5.6, the rather large cross section for these larger E2 solutions makes it unlikely that they are the physical solutions.

A comparison of the calculated E1-E2 phase to the phase extracted from the data is shown in figure 24. This figure shows a plot of the phase difference between the d3/2 E1 amplitude and the f5/2 E2 amplitude. Again the dots

Figure 23. The E2 cross section extracted from data taken with the $^{13}C(p,\gamma_1)^{14}N$ reaction. The solid line represents the results of a direct calculation described in the text.

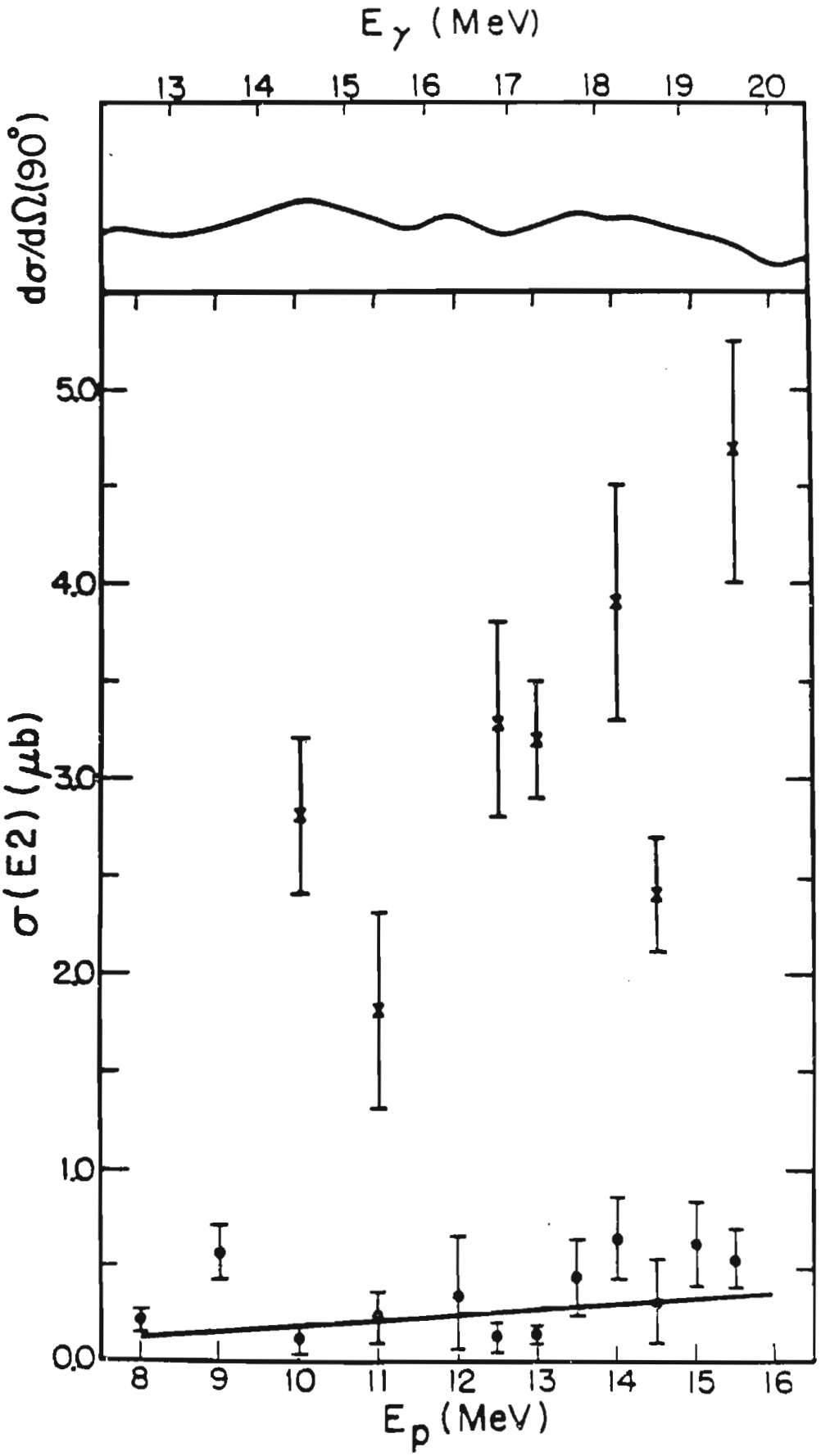
E_γ (MeV)
13 14 15 16 17 18 19 20
$d\sigma/d\Omega(90^\circ)$
5.0
4.0
3.0
2.0
1.0
0.0
$\sigma(E2)$ (μb)
8 9 10 11 12 13 14 15 16
E_p (MeV)

Figure 24. Plot of the E1-E2 phase difference extracted from data taken with the $^{13}C(p,\gamma_1)^{14}N$ reaction. The difference between the d3/2 E1 phase and the f5/2 E2 phase is plotted as a function of energy. The solid line represents the results of direct E1 and E2 calculations.

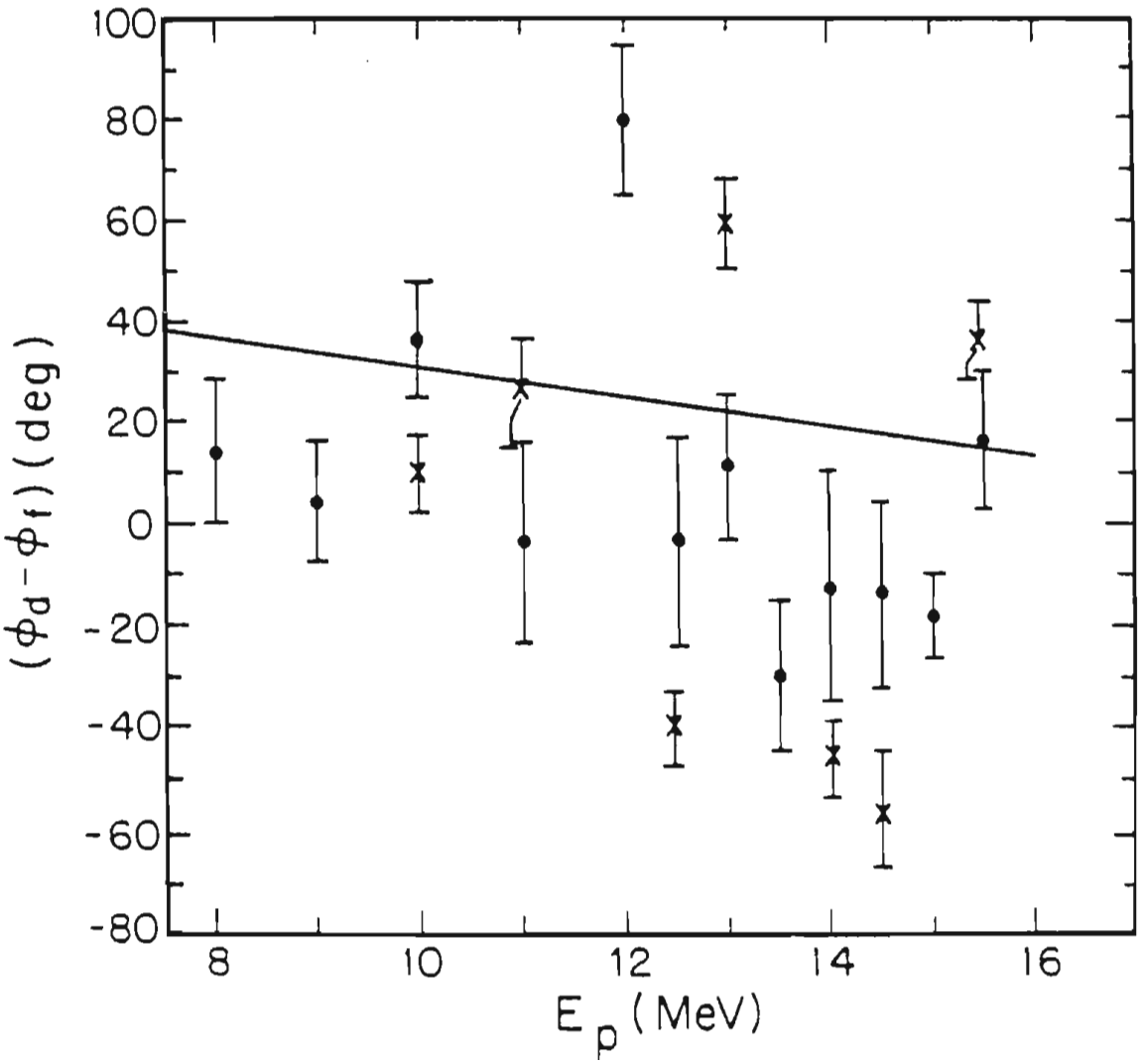
100
80
60
40
20
0
-20
-40
-60
-80
8
10
12
14
16
$(\phi_d - \phi_f)$ (deg)
E_p (MeV)

represent the smaller E2 solutions and the crosses represent the larger E2 solutions. The solid line indicates the relative phase calculated with the direct model. The calculation reflects the trend in the data and differs in value by approximately thirty degrees from typical values of the phase resulting from the smaller E2 solution. Again the values derived from the larger E2 solutions are in somewhat less agreement than the values from the smaller E2 solutions.

5.6 COMPARISON TO SUM RULES

A common measure of nuclear electric dipole absorption strength is the classical dipole sum rule. This sum rule, based on the kinetic energy term of the nuclear Hamiltonian, can be written as (Hayward, 1970)

$$\int \sigma_{E1}(\gamma, P)\, dE = 60NZ/A \quad \text{MeV-mb.}$$

The total cross section for the $^{13}C(p,\gamma_0)^{14}N$ and the $^{13}C(p,\gamma_1)^{14}N$ reactions may be converted to (γ,p) cross sections through the process of detailed balance. The integrated cross section for each of these reactions was obtained by calculating the ratio of A_o to the yield at 90 degrees for each energy where an angular distribution was measured. The yield curves were then divided into regions centered around the angular distribution measurements. The ratio of 90 degrees to A_o was used to calculate a value for

A_0 from each of the points in the appropriate region of the 90 degree yield curve.

The integrated cross section (assumed to be approximately all E1) obtained from data taken with the $^{13}C(p,\gamma_0)^{14}N$ reaction and the procedure described above is 12.4 MeV-mb for excitation energies ranging from 13.3 to 23.3 MeV. This represents 6 percent of the classical dipole sum rule. The integrated cross section for the $^{13}C(p,\gamma_1)^{14}N$ reaction was found to be 18.6 MeV-mb for excitation energies ranging from 11.0 to 21.0 MeV. This represents 9 percent of the classical dipole sum rule for this resonance built on the first excited state of ^{14}N.

The E2 cross section extracted from the data taken with the $^{13}C(p,\gamma_1)^{14}N$ reaction can be compared to the isoscalar sum rule for self-conjugate nuclei. This sum rule is given by (Gell-Mann and Telegdi, 1953)

$$\int \frac{\sigma_{E2}(\gamma,X)}{E_\gamma^2}\, dE_\gamma = \frac{\pi^2}{137}\,\frac{A}{12}\,\frac{\langle r_0^2\rangle}{938}\ \frac{fm^2}{MeV}$$

For self conjugate nuclei such as ^{14}N the Δ T=0 and ΔT=1 sum rules given by Warburton and Weneser (1969) are equal to each other and to the isoscalar sum rule of Gell-Mann and Telegdi. The value cf $\langle r_0^2 \rangle$ required to calculate the isoscalar sum rule can be chosen in several ways. An experimental value of 6.66 fm^2 is given by C.W. deJager et al. (1970) from electron scattering data. A second value

for $\langle r^2_0 \rangle$ is obtained from the assumption of a constant radial wave function up to the nuclear radius, R . This gives the following expression for $\langle r^2_0 \rangle$

$$\langle r^2_0 \rangle = 3/5 (1.2A^{1/3})^2 \quad fm^2$$

Table 7 lists the integrated E2 strength for the smaller and larger E2 solutions and the percentage of the isoscalar sum rule exhausted by each of these solutions. For the latter case, the smaller E2 strength was used where a larger solution did not exist. Comparisons are made to sum rules calculated using both of the values of $\langle r^2_0 \rangle$ given above. The percentage of the sum rule exhausted by the direct model calculation is also listed in the table. The fact that the larger E2 solution essentially exhausts the isoscalar sum rule gives further indication that these solutions can be ruled out and the smaller solutions are the physical ones.

Table 7. Comparison of the Integrated E2 Cross Section to the Isoscalar Sum Rule

item	Integrated Cross Section		$\%(\langle r_o^2\rangle_1)$	$\%(\langle r_o^2\rangle_2)$
small sol	1.2	bn/MeV	20	24
large sol	5.7	bn/MeV	97	114
direct cal	0.8	bn/MeV	13	16

where $\langle r_o^2\rangle_1 = 6.66$ fm^2

and $\langle r_o^2\rangle_2 = 5.57$ fm^2

Chapter VI

SUMMARY AND CONCLUSIONS

The region of the GDR built on the ground state of ^{14}N has been studied with the $^{13}C(p,\gamma_0)^{14}N$ reaction. The observed resonance exhausts 6 percent of the classical dipole sum rule between 13.3 and 23.3 MeV (excitation energy). The yield curve at 90 degrees was compared to earlier measurements of this reaction. Comparison was also made to measurements of the $^{14}N(\gamma,p_0)^{13}C$ and $^{14}N(\gamma,n_0)^{13}N$ cross sections through the process of detailed balance. In general, the agreement of both shape and normalization is good.

An E1 analysis of the GDR region was performed with several simplifying assumptions. Comparisons of the results to a direct model calculation suggested that the solution dominated by the capture of l=2 protons was the physical solution although the model failed to predict the observed values of the relative phase. Our data are consistent with the reaction proceeding primarily through the 2- giant dipole state by the capture of l=2, S=0 protons.

The GDR built on the first excited state has been studied with the $^{13}C(p,\gamma_1)^{14}N$ reaction. This resonance exhausts 9 percent of the classical dipole sum rule between

11.0 and 21.0 MeV. The 90 degree yield curve was compared to earlier data. The differences were attributed to problems known to be present in the earlier work. The location of the peak of the 90 degree yield curve agrees well with the excitation energy of T=0 strength calculated for this nucleus by Vergados.

The GDR region of the resonance built on the first excited state was studied in considerable detail. The angular distribution data was analyzed to determine the T-matrix elements. The favorable combination of target and final spins allows an analysis which includes both E1 and E2 amplitudes. The measurement of cross section data at angles ranging from 30 to 154 degrees substantially reduced the errors on the E2 cross section over similar analyses limited to angles ranging from 42 to 142 degrees. The E1 amplitudes extracted from the data exhibit characteristic double solution behavior. The direct model E1 calculation is in excellent agreement with the solution indicating that the E1 cross section results from approximately 90 percent d3/2 strength. The E2 solutions associated with the predominantly d3/2 E1 solution were also studied in considerable detail. A search to determine chi-squared per degree of freedom as a function of E2 strength revealed two minima at several energies which indicate the presence of two sets of solutions for the E1 and E2 amplitudes and relative phases. A detailed study of these solutions has established the following four points:

1. The chi-squares of the larger E2 solutions are significantly better at only two of the seven energies where double solutions exist.

2. The large E2 solutions imply points of discontinuity in the E1 solutions.

3. The smaller E2 (and corresponding E1) solutions are in better agreement with the calculations.

4. The larger E2 solutions exhaust approximately 100 percent of the isoscalar E2 sum rule.

All four of these points suggest that the smaller E2 solutions are the physical solutions. While the first three points give rise to relatively weak arguments, the fact that the larger solution exhausts the sum rule in this one channel over a relatively small energy region gives a very strong argument that the smaller E2 solutions can be selected as the physical solutions.

The smaller set of E2 solutions exhausts approximately 22 percent of the energy weighted isoscalar sum rule, in reasonable agreement with the 15 percent exhausted by the calculated direct E2 cross section. The present data therefore exhibit no evidence of a compact E2 resonance in the energy region spanned by this study. The small additional E2 strength observed in the data could arise from the tail of an isovector E2 resonance. It would be interesting to expand the energy range of this study to complete the search for possible isovector E2 resonances,

but the proton energies required to undertake such an investigation are not available in this laboratory.

Appendix I

DATA REDUCTION WITH A PEAK FITTING ROUTINE

Gamma ray spectra obtained with NaI detectors characteristically present peaks which are incompletely resolved from peaks corresponding to other states or from the background. Simple arithmetic sums of such peaks are often inadequate for two reasons. First, a sum can be extremely sensitive to the location and separation of the two points which define the summing region. Secondly, peaks from close-lying states are superimposed.

A fitting program has been developed in an effort to relieve these difficulties. This program, called SUPERSAM, fits a characteristic lineshape to peaks in a region of the gamma ray spectrum defined by the operator. The first version of this program was written by R.C. McBroom (1977) and the basic format and sense switch operation of the original version has received little modification. C.P. Cameron added a background subtraction feature and improved the overall efficiency of the program. Recently the original fitting routine (CHIFIT as described by Bevington, 1969) was replaced with the subroutine ROCORD (following the method of Rosenbrock, 1960) and a systematic method for modifying the lineshape parameters to reflect various rejection efficiencies was developed.

The characteristic lineshape of the NaI detector was originally determined from spectra obtained with the $T(p,\gamma)^4He$ reaction. This reaction is ideal for determining the lineshape because the very large Q value virtually eliminates background associated with beam (capture gamma rays from impurities in the target or from the collimator, beampipe, or beamdump) and because the absence of low-lying excited states in the ^4He system insures that the peak will be very well resolved. This latter feature allows a precise fitting of the low energy tail. The lineshape was assumed to have the form of the composite function:

$$F(X) = \left[1-g(X-C9)\right] \exp(C1+C2X+C3X^2+C4X^3) + g(X-C9) \exp(C5+C6X+C7X^2+C8^3)$$

where $g(X-C9) = 0 \quad X<C9$

$= 1 \quad X \geq C9$

and the functions are constrained to have equal value and slope at the point C9. The first term of the function fits the low energy tail and the low energy side of the peak, while the second term fits the maximum and high energy side of the peak. Calculation of the composite function requires constants with at least eight significant places and double precision arithmetic due to loss of significant figures during calculation.

Each individual data spectrum is fitted to the standard lineshape through three parameters. The gain (width), amplitude, and centroid are varied to obtain a minimum of chi-

squared. A transformed coordinate, xfit, is used to calculate chi-squared as follows:

xfit = (xdata-P)/R + C

where xdata = data spectrum channel number

P = data spectrum centroid

R = relative gain of data spectrum

C = centroid of standard spectrum (held fixed at 312.5)

$$X^2 = \sum \left(F(xfit) - F(data)\right)^2 / \left(\Delta F(data)\right)^2$$

where F(xfit) = value of standard lineshape at the transformed coordinate

F(data) = number of counts in data channel xdata of data spectrum multiplied by the ratio of the data spectrum amplitude to the standard spectrum amplitude

The operator selects the data region used to calculate chi-squared.

The lineshape observed in NaI gamma ray spectra is a function of the rejection threshold used during the data collection. The program PARA was written so that the lineshape parameters can be easily modified to describe a new standard lineshape. A total of eleven parameters are involved in the fit; four from each of the two pieces of the composite function, and the height, width, and centroid of the fit to the peak in the data spectrum. The centroid and point of joining of the two pieces of the function (C9) of

the original standard spectrum are not varied. These eleven parameters represent eight degrees of freedom. The coefficients C1 and C5 and relative amplitude of the data and standard peaks represent only two independent parameters and hence C5 was held fixed. Since the point of joining of the two pieces of the composite function (X=294) is not varied, and since the value of the two functions and their slopes are constrained to be equal at this point, two of the variables can be algebraically eliminated. Coefficients C1 and C2 are calculated directly by PARA from these constraints after every iteration made by the fitting routine ROCORD as follows:

$$C2=C6+2C7(294)+3C8(294)^2-2C3(294)-3C4(294)^2$$

$$C1=F-C2(294)-C3(294)^2-C4(294)^3$$

where $F=C5+C6(294)+C7(294)^2+C8(294)^3$

The program PARA contains input instructions and is stored with other capture software. Table A-1 lists the original parameters determined by McBroom (1977) and the parameters determined for use in this study.

Table A-1. Coefficients derived by McBroom (1977) from $T(p,\gamma)^4He$ spectra and coefficients obtained from $^{13}C(p,\gamma)^{14}N$ spectra.

coefficient	$T(p,\gamma)$		$^{13}C(p,\gamma)$	
C1	-3.6393078	00	-21.85820158	00
C2	8.9808694	-02	19.26189638	-02
C3	-4.8943085	-04	-6.21326038	-04
C4	9.1426823	-07	8.81372421	-07
C5	1.4269255	03	1.42692551	03
C6	-1.4676343	01	-1.46753967	01
C7	5.0242390	-02	5.02375991	-02
C8	-5.7103631	-05	-5.71077077	-05
C9	2.94	02	2.94	02

APPENDIX 2

Polarized Proton Capture on ^{59}Co

Polarized proton capture on ^{59}Co

J. D. Turner, C. P. Cameron, and N. R. Roberson
Duke University and Triangle Universities Nuclear Laboratory, Duke Station, Durham, North Carolina 27706

H. R. Weller
University of Florida, Gainesville, Florida 32611
and Triangle Universities Nuclear Laboratory, Duke Station, Durham, North Carolina 27706

D. R. Tilley
North Carolina State University, Raleigh, North Carolina 27607
and Triangle Universities Nuclear Laboratory, Duke Station, Durham, North Carolina 27706

(Received 21 November 1977)

The angular distributions of cross section and of analyzing power for the ^{59}Co$(\vec{p},\gamma_0)$ ^{60}Ni reaction have been measured throughout the giant dipole resonance region of ^{60}Ni. In addition, the 90° yield curve has been measured for E_p from 5.8 to 16.5 MeV. The data are analyzed to deduce the amplitudes and phases of the T matrix elements involved. Comparison of the results is made to both the dynamic collective model calculation of Ligensa and Greiner and to a direct-semidirect model calculation. The direct-semidirect calculation indicates that the reaction proceeds predominantly via the radiative capture of $d_{5/2}$ protons. Isospin splitting is also discussed.

[NUCLEAR REACTIONS ^{59}Co$(\vec{p},\gamma_0)$; measured $\sigma(\theta)$ and $A(\theta)$ E_p = 6.8–12.8 MeV. ^{59}Co(p,γ_0) measured $\sigma(90°)$, E_p = 5.8–16.5. Deduced T-matrix amplitudes and phases. Compared to model calculations.]

I. INTRODUCTION

The giant dipole resonance (GDR) region of ^{60}Ni has been previously studied via the proton-capture reaction.[1] The ^{59}Co (p,γ_0) excitation function obtained in the earlier work was interpreted in terms of the splitting of the $T_<$ = 2 and $T_>$ = 3 isospin components of the GDR of ^{60}Ni and was compared with the calculations of Akyuz and Fallieros.[2] The identification of the isospin components as two possibly overlapping envelopes of strength is in general very difficult and somewhat speculative because other dynamical effects can also introduce structure into the GDR.[3,4]

In the present experiment, angular distributions of cross section, $\sigma(\theta)$, and analyzing power, $A(\theta)$, have been measured for the capture reaction ^{59}Co (p,γ_0) ^{60}Ni with both polarized and unpolarized beams for energies that encompass the GDR. In addition, $\sigma(90°)$ was measured for proton energies of 5.8 to 16.5 MeV. Following previously developed techniques,[5,6] the angular distributions, $\sigma(\theta)$ and $A(\theta)$, were analyzed to determine the relative amplitudes and phases of the T-matrix elements contributing to the $E1$ decay of the GDR. The results of this analysis are compared to the dynamic collective model calculations of Ligensa and Greiner[7] in which the giant dipole phonons are coupled with surface quadrupole vibrations. The agreement is poor at high excitation energies. On the other hand, the results are in reasonably good agreement with a direct-semidirect model[8] calculation which predicts that the major contribution to the dipole transition is from the $d_{5/2}$ transition matrix element. The results are also examined for evidence of isospin splitting.

II. EXPERIMENTAL DETAILS

Since the experimental details of the present work are similar to those described in a previous paper,[9] only the salient features will be discussed. The γ rays were detected with a 25.4 cm × 25.4 cm NaI crystal assembly incorporating a plastic anticoincidence shield. The threshold of the shield discriminator was set low enough to reject the major portion of the escape peaks and over 99% of the cosmic ray background. Escape-peak rejection was necessary in order to resolve the peaks corresponding to γ-ray transitions to the ground and first excited state at 1.32 MeV. All measurements were made with the front face of the NaI detector 56 cm from the target which corresponded to a total angular acceptance of 18°. Figure 1 shows a typical γ-ray spectrum with an energy resolution of approximately 3.3%. The 4.2 ± 0.4 mg/cm^2 self-supporting ^{59}Co target used for these measurements was prepared at Oak Ridge National Laboratory[10] from

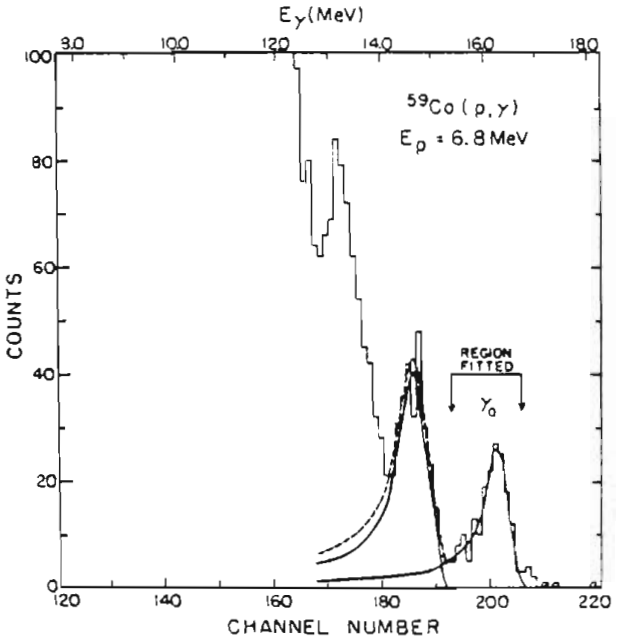

FIG. 1. Typical γ-ray spectrum obtained with the NaI spectrometer.

natural cobalt.

The analyzing power measurements were made with polarized protons from the Triangle Universities Nuclear Laboratory (TUNL) Lamb-shift ion source. Beam currents on target averaged approximately 40 nA. The beam polarization was determined by the quench ratio technique[11] at the beginning and end of each run. Two solid state detectors, mounted at $\pm 160°$ with respect to the beam direction, were used to monitor the asymmetry of the elastically scattered protons. These measurements were used to verify the fact that the beam polarization was constant during a run. Typical beam polarizations were 0.80 ± 0.02.

The efficiency (probability ϵ that a photon will be recorded if it reaches the crystal) of the detector system was determined by measuring the ^{12}C (p,γ_0) thick target (50 keV for 14.2 MeV protons) yield curve over the 15.07 MeV resonance in ^{13}N. This yield, along with the recent measurement[12] of the number of γ rays per proton $(6.83 \pm 0.22) \times 10^{-9}$, was used to determine the efficiency. The value obtained was $\epsilon = 0.168 \pm 0.011$, when the peak was summed in the full-energy region. It is assumed that the efficiency remains constant for all γ-ray energies of the present work.

III. ANALYSIS OF DATA

The yields for the angular distributions for γ-ray transitions to the ground state were determined by fitting a characteristic line shape to the spectrum using a least squares criterion (see Fig. 1). The γ_0 peak was then stripped from the spectrum and a fit was obtained for γ_1, the transition to the first excited state. This procedure was followed to ensure a proper separation of γ_0 and γ_1. A constant line width was used to fit all of the peaks obtained at different angles but at the same proton energy. The data for $\sigma(90°)$ were obtained by summing the region shown in Fig. 1.

The angular distributions for the center of mass cross sections were least squares fitted to an expansion of Legendre polynomials.

$$\sigma(\theta) = A_0 \left[1 + \sum_{k=1} a_k Q_k P_k(\cos\theta) \right],$$

where the coefficients Q_k correct for the finite geometry and $a_0 = 1$. The asymmetry measurements are presented in terms of the quantity $\sigma(\theta)A(\theta)/A_0$, where

$$A(\theta) = \left[\frac{N_+ - N_-}{N_+ + N_-} \frac{1}{P} \right].$$

In this expression P is the beam polarization and N_+ and N_- are the number of counts obtained for spin up and spin down, respectively. This product was fitted by an expansion in associated Legendre polynomials,

$$\frac{A(\theta)\sigma(\theta)}{A_0} = \sum_{k=1} b_k Q_k P_k^1(\cos\theta).$$

Fits were made through $k = 2$ for both the cross sections and asymmetries. Additional fits were also made through $k = 3$, but the inclusion of the $k = 3$ terms for $\sigma(\theta)$ was generally not statistically justified and did not seriously affect the value of a_2. This is in agreement with the Landsdorf suggestion[13] that the angular distributions must extend beyond the zero of $P_k(\cos\theta)$ if a_k is to be determined with statistical significance. Since there is no b_0 and since the zeros of $P_k^1(\cos\theta)$ occur at angles closer to 90° than for $P_k(\cos\theta)$, the $k = 3$ terms for $A(\theta)\sigma(\theta)/A_0$ were statistically significant and will be presented. The generally small values of b_1 and b_3 (relative to b_2), which arise only from the interference of $E1$ radiation with other multipoles, are consistent with the usual assumption that $E1$ radiation dominates this reaction in this energy region.

IV. RESULTS

The 90° yield curve, shown in Fig. 2, was measured from 5.8 to 8.0 MeV in 100 keV steps, from 8.0 to 11.0 MeV in 150 keV steps, and from 11.0 to 16.5 MeV in 200 keV steps. The errors shown are purely statistical, while the absolute cross section determined from the efficiency, target

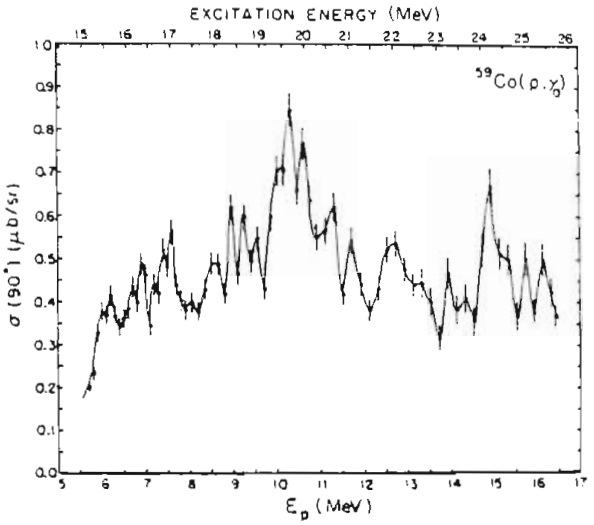

FIG. 2. The 90° yield curve for the ^{59}Co(p, γ_0) ^{60}Ni reaction. The error bars represent the statistical error associated with the data points and the solid curve is a smooth line drawn through the data points.

thickness, and beam current integration has an uncertainty of ±11%. The agreement of these data with those of Diener *et al.*[1] is fair; the general shapes of the two $\sigma(90°)$ yield curves are similar, and the absolute cross sections obtained in the two experiments agree within the errors quoted.

A sample of the angular distribution data is shown in Fig. 3 where $\sigma(\theta)/A_0$ and $A(\theta)\sigma(\theta)/A_0$ are presented for three different energies. Data were taken at five angles for each proton beam energy. The solid curves are the fits as previously described. The a_k and b_k coefficients obtained from all the fits are tabulated in Table I along with the a_k's from Ref. 1.

Since the ground state spin and parity of ^{59}Co is

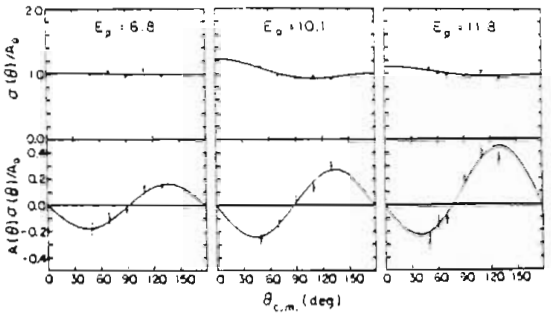

FIG. 3. Typical data at three energies for the quantities $\sigma(\theta)/A_0$ and $\sigma(\theta)A(\theta)/A_0$. The errors bars represent the statistical errors associated with the data points. The solid curves are the result of fitting the data as described in the text.

$\frac{7}{2}^-$, there are three amplitudes that can contribute to the formation of the 1^- dipole state. Each of these can be represented by a transition matrix element labeled by the total angular momentum brought in by the proton. Each of these T-matrix elements will have an amplitude and a phase which can be denoted by $d_{5/2}$, $g_{7/2}$, and $g_{9/2}$ and $\phi(d_{5/2})$, $\phi(g_{7/2})$, and $\phi(g_{9/2})$, respectively. With the assumption of pure $E1$ radiation and neglecting the possibility of statistical compound nuclear effects, the a_0, a_2, and b_2 coefficients can be expressed in terms of the three amplitudes and phases as

$$
\begin{aligned}
a_0 &= 1 = d_{5/2}^2 + g_{7/2}^2 + g_{9/2}^2 ,\\
a_2 &= -0.143 d_{5/2}^2 - 0.247 d_{5/2} g_{7/2} \cos(d_{5/2}, g_{7/2}) \\
&\quad + 1.464 d_{5/2} g_{9/2} \cos(d_{5/2}, g_{9/2}) + 0.476 g_{7/2}^2 \\
&\quad + 0.282 g_{7/2} g_{9/2} \cos(g_{7/2}, g_{9/2}) - 0.333 g_{9/2}^2 , \qquad (1)\\
b_2 &= 0.289 d_{5/2} g_{7/2} \sin(d_{5/2}, g_{7/2}) \\
&\quad + 0.488 d_{5/2} g_{9/2} \sin(d_{5/2}, g_{9/2}) \\
&\quad + 0.423 g_{7/2} g_{9/2} \sin(g_{7/2}, g_{9/2}) ,
\end{aligned}
$$

TABLE I. The a_k and b_k coefficients obtained from least squares fits to the data as described in the text. Also presented are the a_2 coefficients from Ref. 1.

E_p (MeV)	a_1	a_2	χ_2	b_1	b_2	b_3	χ_2
6.70[a]	0.02 ± 0.03	0.03 ± 0.05	1.5				
6.80	0.01 ± 0.05	0.01 ± 0.07	1.8	−0.01 ± 0.03	−0.12 ± 0.02	0.00 ± 0.02	0.5
7.20	0.06 ± 0.03	0.15 ± 0.06	0.4	0.05 ± 0.02	−0.15 ± 0.02	0.04 ± 0.02	1.3
7.55[a]	0.08 ± 0.05	0.16 ± 0.07	1.5				
7.60[a]	−0.01 ± 0.02	0.28 ± 0.03	0.6				
7.75	0.02 ± 0.04	0.10 ± 0.08	6.1	0.02 ± 0.03	−0.10 ± 0.02	0.01 ± 0.02	0.1
8.75	0.05 ± 0.03	0.26 ± 0.05	1.5	0.04 ± 0.02	−0.10 ± 0.02	0.00 ± 0.02	0.9
10.00[a]	0.22 ± 0.03	0.07 ± 0.04	1.5				
10.10	0.11 ± 0.03	0.12 ± 0.06	0.7	0.02 ± 0.02	−0.17 ± 0.02	0.01 ± 0.02	1.1
10.60	0.11 ± 0.04	0.12 ± 0.06	0.4	0.04 ± 0.02	−0.18 ± 0.02	−0.01 ± 0.02	8.1
11.80	0.06 ± 0.04	0.05 ± 0.06	1.2	0.14 ± 0.03	−0.23 ± 0.02	−0.05 ± 0.02	0.8
12.80	0.12 ± 0.03	−0.03 ± 0.06	2.8	0.05 ± 0.02	−0.14 ± 0.02	−0.02 ± 0.02	1.9

[a] From Ref. 1.

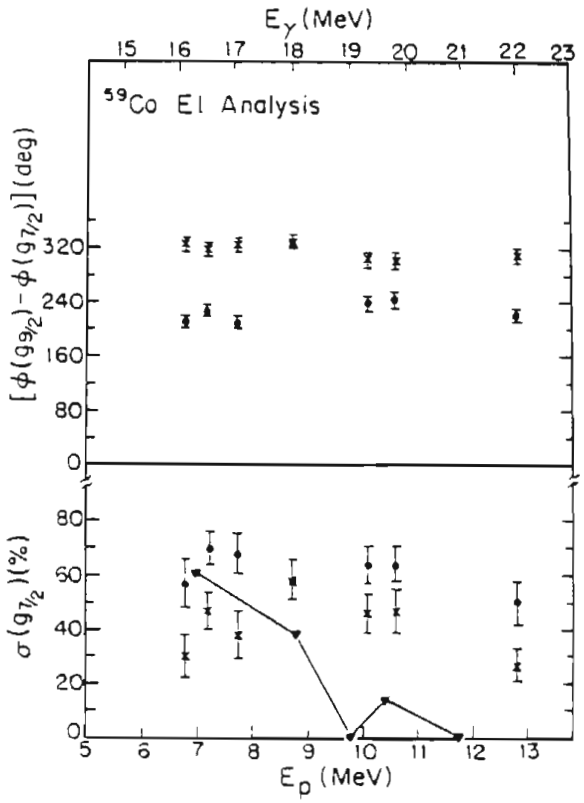

FIG. 4. Comparision of the transition matrix element amplitudes extracted from the present data with those calculated at five energies by Ligensa and Greiner. The dots and crosses represent the two mathematical solutions at each energy as mentioned in the text. The solid curve connects the five calculated values. The results are presented as a percentage of the cross section, $\sigma(g_{7/2}) + \sigma(g_{9/2})$, where $\sigma(g_{7/2}) = g_{7/2}{}^2$, etc. It should be noted that no mathematical solution was found for the data at $E_p = 11.3$ MeV. The error bars represent the statistical errors associated with the data.

where $(d_{5/2}, g_{7/2})$ stands for $\phi(d_{5/2}) - \phi(g_{7/2})$, etc.[14] Since these three equations involve five variables, there are many possible solutions for the amplitudes and relative phases. In an earlier study at this laboratory of the GDR in ^{55,57,59}Co, Cameron *et al.*[15] found that restrictions on one of the phase differences proved useful in limiting the range of the solutions. In this case, however, such restrictions are of little help, and hence the guidance of model calculations in the reduction of the number of amplitudes is necessary to proceed further with the analysis.

Ligensa and Greiner[7] (LG) have made detailed calculations for ^{60}Ni. They described the GDR as a coupling of the 1p-1h states to quadrupole surface vibrations. These states were then coupled to the continuum via a residual interaction. The calculated particle widths obtained with this model indicate that the $d_{5/2}$ amplitude is small and can be neglected. If only the $g_{7/2}$ and $g_{9/2}$ amplitudes and their relative phase are included in Eq. 1, the resulting quadratic equation can be solved exactly. Errors for the solutions were derived from the error matrix and reflect the proper statistical errors.[16] At each energy, two mathematical solutions are obtained and Fig. 4 shows a comparison between these solutions (dots and crosses) from the present analysis with the solutions calculated by LG. Note that $\sigma(g_{7/2}) = g_{7/2}{}^2$, etc. At the lower excitation energies there is some agreement, but at the higher energies there are large discrepancies.

A reaction model which has been used to predict angular distributions for radiative capture is the direct-semidirect (DSD) capture model.[8] The required radial matrix element for $E1$ capture is

$$\left\langle \phi_{nlj}(r) \left| r + \frac{V_1(r)}{E_\gamma - E_d + i\Gamma_d/2} \right| \phi_{l'j'}(r) \right\rangle ,$$

where $V_1(r)$ is the radial part of the form factor. The kets $|\phi_{l'j'}\rangle$ and $|\phi_{nlj}\rangle$ are the proton continuum and bound state wave functions, respectively. If the form factor is taken to be that suggested by Brown,[8] the predicted angular distributions (that is, the relative amplitudes and phases of the T-matrix elements) will be identical[17] to those obtained from a pure direct calculation, i.e., $V_1(r) = 0$, if the resonance parameters are taken to be the same for all matrix elements. Other versions of the form factor have been used[17-19] but, in fact, Likar *et al.*[17] have concluded (for $l \leq 3$ and medium weight nuclei) that all approaches using real form factors give approximately the same energy dependence for the a_2 coefficient. Consequently, for pure $E1$ radiation it is only necessary to perform a direct calculation[20] though the calculation can be considered to be either pure direct, or direct-semidirect (DSD) with the Brown form factor.[8]

The continuum single particle wave functions were calculated with the optical model parameters of Becchetti and Greenlees.[21] The bound state single particle wave function was obtained by integrating the Schrödinger equation with a Woods-Saxon potential including a spin-orbit term with $V_{so} = 6.2$ MeV. The experimental binding energy of 9.53 MeV for the proton was used to determine the well depth of 57.3 MeV. The matrix elements are simply related to the transition amplitudes through a Clebsch-Gordan coefficient. The resulting calculation indicates that all three matrix elements ($d_{5/2}$, $g_{7/2}$, and $g_{9/2}$) have approximately the same magnitude, but the Clebsch-Gordan coefficient reduces the relative $g_{7/2}$ amplitude by a factor of almost 40.

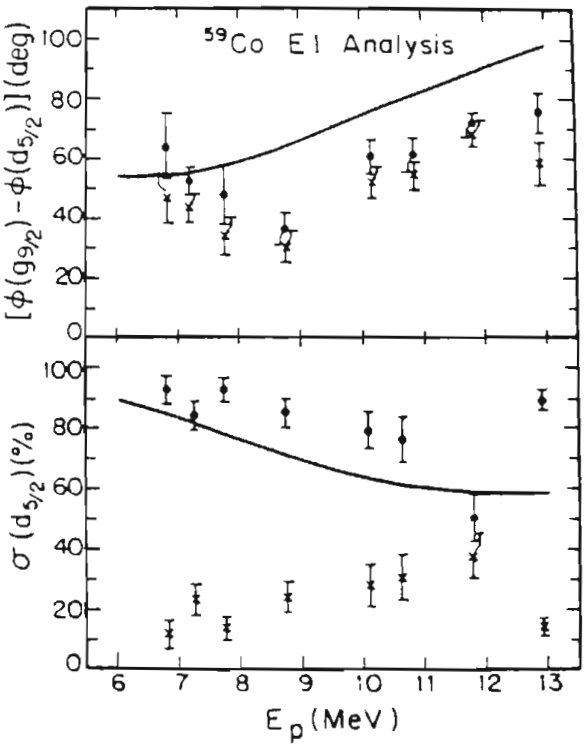

FIG. 5. Comparison of the transition matrix elements extracted from the present data with those from a direct-semidirect reaction model calculation as described in the text. The solid curve shows the results of the calculation. The results are presented as a percentage of the cross section, $\sigma(d_{5/2}) + \sigma(g_{9/2})$, where $\sigma(d_{5/2}) = d_{5/2}{}^2$, etc. The error bars represent the statistical errors associated with the data.

This result can be examined by considering the transformation between the amplitudes in the LS and jj coupling schemes which are given by[22]

$$d_{13} = d_{5/2},$$

$$g_{13} = -0.167 g_{7/2} + 0.986 g_{9/2},$$

$$g_{14} = 0.986 g_{7/2} + 0.167 g_{9/2}.$$

The notation here is L_{JS}, where L is the letter assigned to the orbital angular momentum, J is the total angular momentum, and S is the channel spin. These equations show that the $g_{7/2}$ amplitude is nearly identical to the g_{14} "spin flip" amplitude. Neglect of this amplitude seems reasonable.

If in Eq. (1) the $g_{7/2}$ amplitude is set equal to zero, and if only the $d_{5/2}$ and $g_{9/2}$ amplitudes are included, two mathematical solutions are obtained from the data at each energy. The results of this analysis (dots and crosses) are shown in Fig. 5. The errors shown are derived from the error matrix as mentioned above. The DSD predictions, also shown in Fig. 5, were normalized for plotting purposes such that $\sigma(g_{9/2}) + \sigma(d_{5/2}) = 100\%$, where $\sigma(d_{5/2}) = d_{5/2}{}^2$, etc. In fact, the calculations predict that $\sigma(g_{7/2})$ typically accounts for $<6\%$ of the cross section. This normalization procedure, of course, does not affect the relative $d_{5/2}$ to $g_{9/2}$ strength. The calculations are in good agreement with the predominantly $d_{5/2}$ solution and hence remove the ambiguity of the two solutions. This result indicates the importance of considering the particle decay channel in evaluating the transition matrix elements. So, despite the fact that the $E1$ transition rate is larger for the $g_{9/2}$ than for the $d_{5/2}$ single particle state, the coupling to the proton channel results in the predominance of the $d_{5/2}$ transition matrix element.

The relative amplitudes obtained from the experiment change slowly across the GDR except for the single point at $E_p = 12.8$ MeV, while the relative $g_{9/2}$ to $d_{5/2}$ phase changes smoothly except for a small inflection near $E_p = 8.8$ MeV, a point about midway between the proposed isospin components. The results of these data and calculations appear to imply that isospin effects do not significantly affect the relative amplitudes and phases. Therefore, no definitive evidence for isospin splitting has been observed in this experiment. If any effect of isospin splitting is present in these results, it would appear that it is in the relative phase of the T-matrix elements. This observation requires further investigation.

This work was supported by the U. S. Department of Energy and by the National Science Foundation. We thank Dr. Steve Wender, Dr. Richard Blue, and Steve Manglos for valuable assistance, and Dr. Steve Cotanch for providing us with the computer code used to calculate the direct radial matrix elements.

[1] E. M. Diener, J. F. Amann, P. Paul, and S. L. Blatt, Phys. Rev. C 3, 2303 (1971).
[2] R. O. Akyuz and S. Fallieros, Phys. Rev. Lett. 27, 1016 (1971).
[3] Evans Hayward, B. F. Gibson, and J. S. O'Connell, Phys. Rev. C 5, 346 (1972).
[4] P. Paul, in *Proceedings of the International Conference on Photonuclear Reactions and Applications, Asilomar, 1973*, edited by B. L. Berman (Lawrence Livermore Laboratory, University of California, 1973), p. 407.
[5] S. S. Hanna, H. F. Glavish, E. M. Diener, J. R. Calarco, C. C. Chang, R. Avida, and R. N. Boyd, Phys. Lett. 40B, 631 (1972).
[6] H. R. Weller, R. A. Blue, N. R. Roberson, D. G.

Rickel, C. P. Cameron, R. D. Leford, and D. R. Tilley, Phys. Rev. C 3, 922 (1976), and references therein.
[7]Rainer Ligensa and Walter Greiner, Ann. Phys. 51, 28 (1969).
[8]G. E. Brown, Nucl. Phys. 57, 339 (1964).
[9]H. R. Weller, N. R. Roberson, D. G. Rickel, C. P. Cameron, R. D. Ledford, and D. R. Tilley, Phys. Rev. C 13, 922 (1976).
[10]Oak Ridge National Laboratories, Isotope Sales, Oak Ridge, Tennessee.
[11]T. A. Trainer, T. B. Clegg, and P. W. Lisowski, Nucl. Phys. A220, 533 (1974).
[12]R. E. Marrs, E. G. Adelburger, K. A. Snover, and M. D. Cooper, Phys. Rev. Lett. 35, 202 (1975).
[13]A. Landsdorf, in *Fast Neutron Physics*, edited by J. B. Marion and J. L. Fowler (Interscience, New York, 1960), p. 744.
[14]It should be noted that there is a sign error in the a_2 coefficient in the $d_{5/2}$, $g_{9/2}$ term as given by Diener *et al.* (Ref. 1).
[15]C. P. Cameron, N. R. Roberson, D. G. Rickel, R. D. Ledford, H. R. Weller, R. A. Blue, and D. R. Tilley, Phys. Rev. C 14, 553 (1976).
[16]P. R. Bevington, *Data Reduction and Error Analysis for the Physical Sciences* (McGraw-Hill, New York, 1969), p. 154.
[17]A. Likar, M. Potokar, and F. Cvelbar, Nucl. Phys. A280, 49 (1977), and references therein.
[18]C. F. Clement, A. M. Lane, and S. R. Rook, Nucl. Phys. 66, 273 (1965).
[19]K. A. Snover, J. E. Bussoletti, K. Ebisawa, T. A. Trainer, and A. B. McDonald, Phys. Rev. Lett. 37, 273 (1976).
[20]S. Cotanch, private communication.
[21]F. D. Becchetti and G. W. Greenlees, Phys. Rev. 182, 1190 (1969).
[22]A. S. Ferguson, *Angular Correlation Methods in Gamma-Ray Spectroscopy* (North-Holland, Amsterdam, 1965), p. 13.

LIST OF REFERENCES

J. E. E. Baglin, E. J. Bentz, and R. W. Carr, Phys. Rev. C. 10 (1974) 24.

P. R. Bevington, in Data Reduction and Error Analysis for the Physical Sciences (McGraw Hill, Inc., 1969).

G. E. Brown, Nucl. Phys. 57 (1964) 339.

C. P. Cameron, unpublished Ph.D. thesis, Duke University, 1977.

T. B. Clegg, G. A. Bissenger, W. Haeberli, and P. A. Quin, in Polarization Phenomena in Nuclear Reactions ed. H. H. Barschall and W. Haeberli, (University of Wisconsin Press, Madison, Wis., 1970).

C. F. Clement, A. M. Lane, and S. R. Rook, Nucl. Phys. 66 (1965) 273.

S. Cohen and D. Kurath, Nucl. Phys. A101 (1967) 1.

B. L. Cohen, Phys. Rev. 100 (1955) 206.

S. R. Cotanch, private communication, 1978. See also M. G. Mustafa and F. B. Malik, Phys. Rev. C2 (1970) 2068.

W. Del Bianco, S. Kundu, J. Kim, Nucl. Phys. A270 (1976) 45.

H. Feshbach, Porter, and V. Weisskopf, Phys. Rev. 96 (1954) 448.

S. Fugii and O. Sugimoto, Nuovo Cimento, XII (1959) 513.

M. Gell-Mann and V. L. Telegdi, Phys. Rev. 91 (1953) 169.

R. W. Gellie, K. H. Lokan, N. K. Shermon, R. G. Johnson, and J. I. Lodge, Can. J. Phys. 50 (1972) 1689.

H. F. Glavish, S. S. Hanna, R. Avida, R. N. Boyd, C. C. Chang, and E. Diener, Phys. Rev. Lett. 28 (1972) 766.

H. F. Glavish, private communication, 1974.

S. S. Hanna, H. F. Glavish, E. M. Diener, J. R. Calarco, C. C. Chang, R. Avida, and R. N. Boyd, Phys. Lett. 40B (1972) 631.

S. S. Hanna, H. F. Glavish, R. Avida, J. R. Calarco, E. Kuhlmann, and R. LaCanna, Phys. Rev. Lett. 32 (1974) 114.

S. S. Hanna in Proceedings of the International Conference on Nuclear Structure and Spectroscopy, vol. 2, ed. H. P. Blok and A. E. L. Dieperink (Scholar's Press, Amsterdam, The Netherlands, 1974) 249.

S. S. Hanna in Lecture Notes in Physics, vol. 61, ed. J. Ehlers, K. Kepp, R. Kippenhahn, H. A. Weidenmueller and J. Zittartz (Springer - Verlag, New York, 1977) 275.

E. Hayward, Nat. Bur. Stand. (U.S.) Monograph 118, 1970.

M. Hasinoff, D. Johnson and D. F. Measday, Phys. Lett. 39B (1972) 506.

A. Landsdorf in Fast Neutron Physics, ed. J. B. Marion and J. L. Fowler (Interscience Publishers, New York, 1960) 744.

A. Likar, M. Potokar, and F. Cvelbar, Nucl. Phys. A280 (1977) 49. and references therein.

A. M. Lane, Nucl. Phys. 11 (1959) 625.

R. D. Ledford, unpublished Ph. D. thesis, Duke University, 1976.

R. E. Mans, E. G. Adelberger, K. A. Snover, and M. D. Cooper, Phys. Rev. Lett. 35 (1975) 202.

R. C. McBroom, unpublished Ph. D. thesis, Univ. of Florida, 1976.

P. Paul, H. S. Kuan, E. K. Warburton, Nucl. Phys. A254 (1975) 1.

A. Richter and S. J. Parish, Phys. Rev. Lett. 21 (1968) 1824.

F. Riess, W. J. O'Connell, and P. Paul, Nucl. Phys. A175 (1971) 462.

H. H. Rosenbrock, Comput. J. 3 (1960) 175.

D. M. Skopik, private communication, 1978.

K. A. Snover, J. E. Bussoletti, K. Ebisawa, T. A. Trainor, and A. B. McDonald, Phys. Rev. Lett. 37 (1976) 273.

M. Suffert, W. Feldman, J. Mahieuk, and S. S. Hanna, Nucl. Inst. and Methods 63 (1968) 1.

T. A. Trainor, T. B. Clegg, P. W. Lisowski, Nucl. Phys. A220 (1974) 533.

J. D. Vergados, Nucl. Phys. A239 (1975) 271.

G. J. Wagner, private communication, Max-Planck-Institut fuer Kernphysik, 6900 Heidelberg, Germany.

E. K. Warburton and J. Weneser in Isospin in Nuclear Physics, ed. D. H. Wilkinson (North Holland Publishing Company, Amsterdam, 1969) 173.

H. R. Weller, N. R. Roberson, and S. R. Cotanch, to be published in Phys. Rev. C, July 1978.

H. R. Weller. N. R. Roberson, D. Rickel, C. P. Cameron, R. D. Ledford, T. B. Clegg, Phys. Rev. Lett. 32 (1974) 177.

H. R. Weller, R. A. Blue, N. R. Roberson, D. G. Rickel, S. Maripuu, C. P. Cameron, R. D. Ledford, and D. R. Tilley, Phys. Rev. C 13 (1976) 922.

H. R. Weller, Private Communication, 1978.

BIOGRAPHY

PERSONAL: Born August 23, 1952, Bristol, Virginia
single

EDUCATION: B. S. (cum laude) Wake Forest University (1973)
Joint Majors in Physics and Philosophy

MEMBERSHIPS: Phi Beta Kappa, Sigma Pi Sigma, American Physical Society

PUBLICATIONS:

1. Assignment of 0- to the 2.99-MeV Level in ^{38}K via the ^{40}Ca(d,α)^{38}K reaction (with D. G. Rickel, N. R. Roberson, H. R. Weller, and D. R. Tilley) Phys. Rev. C13 (1976) 2077.

2. g Factor of the 738 KeV State in ^{43}K (with S. A. Wender, C. R. Gould, D. R. Tilley, D. G. Rickel, and N. R. Roberson) Phys. Rev. C14 (1976) 1179.

3. Polarized Proton Capture on ^{59}Co (with C. P. Cameron, N. R. Roberson, H. R. Weller, and D. R. Tilley) Phys. Rev. C17 (1978) 1853.

ABSTRACTS:

1. Study of Giant Dipole Resonances in the Co Isotopes Using Proton Capture and Polarized Proton Capture Measurements (with H. R. Weller, R. A. Blue, D. Griggs, N. R. Roberson, D. G. Rickel, C. P. Cameron, R. D. Ledford, and D. R. Tilley) Bull. Am. Phys. Soc. 19 (1974) 988.

2. The Giant Dipole Resonance Region of ^{31}P (with C. P. Cameron, D. G. Rickel, R. D. Ledford, N. R. Roberson, D. R. Tilley, R. C. McBroom,

R. A. Blue, and H. R. Weller) Bull. Am. Phys. Soc. 21 (1976) 556.

3. Investigation of the 3/2 Analogue State in ^{89}Y at E 14.62 MeV Using the $^{88}Sr(p,\gamma)^{89}Y$ Reaction (with C. P. Cameron, D. G. Rickel, R. D. Ledford, N. R. Roberson, D. R. Tilley, R. C. McBroom, and H. R. Weller) Bull. Am. Phys. Soc. 21 (1976) 581.

4. Study of the Giant Dipole Resonance of ^{89}Y (with R. D. Ledford, N. R. Roberson, C. P. Cameron, D. G. Rickel, D. R. Tilley, R. C. McBroom, and H. R. Weller) Bull. Am. Phys. Soc. 21 (1976) 516.

5. The $T(p,\gamma)^4He$ Reaction for $17<E_p<30$ MeV (with R. C. McBroom, H. R. Weller, N. R. Roberson, R. D. Ledford, C. P. Cameron, and D. R. Tilley) Bull. Am. Phys. Soc. 21 (1976) 534.

6. Evidence for $J^\pi=2^+$ States in ^4He (with R. C. McBroom, H. R. Weller, N. R. Roberson, R. D. Ledford, C. P. Cameron, and D. R. Tilley) Bull. Am. Phys. Soc. 21 (1976) 997.

7. Search for Collective E2 Resonances Above the Giant Dipole Resonance (with C. P. Cameron, R. D. Ledford, N. R. Roberson, H. R. Weller, R. A. Blue, R. C. McBroom, and D. R. Tilley) Bull. Am. Phys. Soc. 21 (1976) 996.

8. A Study of the Reaction $D(p,\gamma)^3He$ (with D. M. Skopik, H. R. Weller, R. A. Blue, N. R. Roberson, C. P. Cameron, and S. A. Wender) Bull. Am. Phys. Soc. 22 (1977) 1021.

9. Polarized Proton Capture on ^{59}Co (with N. R. Roberson, C. P. Cameron, H. R. Weller, D. R. Tilley, and S. F. Cotanch) Bull. Am. Phys. Soc. 23 (1977) 1022.

10. Polarized Proton Capture on ^{13}C (with N. R. Roberson, C. P. Cameron, H. R. Weller, S. A. Wender, and D. R. Tilley) Bull. Am. Phys. Soc. 23 (1978) 602.